

**OPTICAL ANALYSIS AND MODELING OF A WINDOW FOR SMALL
PARTICLE RECEIVER USING THE MONTE CARLO RAY TRACE
METHOD**

A Thesis
Presented to the
Faculty of
San Diego State University

In Partial Fulfillment
of the Requirements for the Degree
Master of Science
in
Mechanical Engineering

by
Ahmet Murat Mecit

Spring 2013

SAN DIEGO STATE UNIVERSITY

The Undersigned Faculty Committee Approves the

Thesis of Ahmet Murat Mecit:

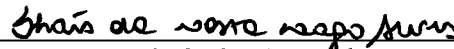
Optical Analysis and Modeling of a Window for Small Particle Receiver Using
the Monte Carlo Ray Trace Method



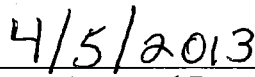
Fletcher J. Miller, Chair
Department of Mechanical Engineering



Randall M. German
Department of Mechanical Engineering



Thaís da C. L. Alves
Department of Civil, Construction, and Environmental Engineering



Approval Date

Copyright © 2013
by
Ahmet Murat Mecit
All Rights Reserved

DEDICATION

Dedicated to my family.

ABSTRACT OF THE THESIS

Optical Analysis and Modeling of a Window for Small Particle
Receiver Using the Monte Carlo Ray Trace Method

by

Ahmet Murat Mecit

Master of Science in Mechanical Engineering

San Diego State University, 2013

Concentrated solar power (CSP) systems use heliostats to concentrate solar radiation in order to produce heat, which drives a turbine to generate electricity. The Combustion & Solar Energy Laboratory (CSEL) at San Diego State University is developing a new type of receiver for power tower CSP plants based on volumetric absorption by a gas-particle suspension. The radiation enters the pressurized receiver through a window, which must sustain the thermal loads from the concentrated solar flux and infrared reradiation from inside the receiver. The window is curved in a dome shape to withstand the pressure within the receiver and help minimize the stresses caused by thermal loading. It is highly important to estimate how much radiation goes through the window into the receiver and the spatial and directional distribution of the radiation. These factors play an important role in the efficiency of the receiver and the thermal load on the receiver walls, as well as window survivability.

Concentrated solar flux was calculated with a computer code called MIRVAL from Sandia National Laboratory which uses the Monte Carlo Ray Trace (MCRT) method. The computer code is capable of taking the day of the year and time of day into account, which causes a variation in the flux. Knowing the concentrated solar flux distribution, it is possible to calculate the solar radiation through the window and the thermal loading on the window from the short wavelength solar radiation. The MIRVAL code as originally written did not account for spectral variations, but we have added that capability.

Optical properties of the window such as the transmissivity, absorptivity, and reflectivity need to be known in order to trace the rays at the window. A separate computer code was developed to calculate the optical properties depending on the incident angle and the wavelength of the incident radiation by using data for the absorptive index and refractive index for the window (quartz) from other studies and vendor information. Two sets of equations are used depending on the opacity of the window. This method accounts for regions where the window is partially transparent and internal absorption can occur.

A third code was developed using the MCRT method and coupled with both codes mentioned above to calculate the exterior thermal load on the window and the solar radiation that enters the receiver. Thermal loading was calculated from energy absorbed at various points throughout the window, including the effect of double reflections. In our study, window shapes from flat to concave hemispherical, as well as a novel concave ellipsoidal window are considered, including the effect of day of the year and time of the day. The results showed the hemispherical window has the highest transmission.

The tilt angle of the receiver for a chosen location at the power tower was studied to let the most amount of solar radiation in the receiver. According to results, the best tilt angle

varies from 25 to 26.5 depending on the geometry of the window for the heliostat field at the National Solar Thermal Test Facility. The thickness of the window was also varied from 10 mm to 40 mm to see the effect of the thickness, but 25 mm was picked as a lower limit considering the suggestions from the vendor. Several grades of fused quartz were considered, since the absorptive index can vary substantially depending on the purity. Last but not the least, absorption maps were created to study the heat flux across the window for different times of day.

The results of this research indicate that tilt angle and time of day did not have a significant effect on the transmission and absorption of the window. On the other hand, window thickness, geometry, and material type had a tremendous impact on the results. Certain grades of quartz from Hereaus were found to be much better than generic quartz, although a final conclusion on this is still open since we were unable to obtain a reliable data set of absorptive index across a wide wavelength range. Optically, the hemispherical window showed the best results for all window geometries. However, there are other factors, such as manufacturing constrains, mounting, cost, and heat losses from inside of the receiver, to consider when choosing the best window for the receiver. These factors are under research by other students in the SDSU Combustion and Solar Energy Laboratory and will be evaluated along with the optical predictions from this thesis to choose the optimal window shape.

TABLE OF CONTENTS

| | PAGE |
|--|------|
| ABSTRACT | v |
| LIST OF TABLES | ix |
| LIST OF FIGURES | x |
| NOMENCLATURE | xiii |
| ACKNOWLEDGEMENTS | xv |
| CHAPTER | |
| 1 INTRODUCTION | 1 |
| Concentrated Solar Power Systems | 1 |
| Small Particle Solar Receiver | 5 |
| Windowed Receivers | 6 |
| Monte Carlo Ray Trace (MCRT) Introduction | 10 |
| Overview of this Thesis | 11 |
| 2 MIRVAL | 13 |
| The Accuracy of MIRVAL | 16 |
| Spectral Variation | 22 |
| 3 OPTICAL PROPERTIES OF THE WINDOW | 28 |
| The Index of Refraction and the Absorptive Index | 30 |
| The Optical Thickness | 33 |
| The Absorptivity, Reflectivity, and Transmissivity | 34 |
| Low Opacity Method | 34 |
| High Opacity Method | 37 |
| Results for the Optical Properties | 39 |
| 4 WINDOW MATERIAL | 50 |
| 5 WINDOW GEOMETRY | 58 |
| 6 MONTE CARLO RAY TRACE | 61 |
| 7 RESULTS | 70 |
| Tilt Angle Study | 71 |

| | |
|--|----|
| Incident Angle Study | 73 |
| Thickness Study | 74 |
| The Effects of the Geometry | 78 |
| Absorption Maps on the Window | 80 |
| 8 CONCLUSIONS..... | 87 |
| 9 FUTURE WORK..... | 90 |
| REFERENCES | 92 |
| APPENDIX | |
| FIT EQUATIONS FOR ABSORPTIVE INDEX FOR GENERIC FUSED QUARTZ | 95 |

LIST OF TABLES

| | PAGE |
|---|------|
| Table 1. Direct Circumsolar Irradiance with Respect to Wavelength | 25 |

LIST OF FIGURES

| | PAGE |
|--|------|
| Figure 1. Types of concentrated solar power technologies..... | 3 |
| Figure 2. Schematic of a small particle solar receiver..... | 5 |
| Figure 3. Schematic of pressurized high-temperature DLR receiver. | 7 |
| Figure 4. Schematic of the receiver that is tested at Weizmann Institute in Israel. | 8 |
| Figure 5. A schematic of the small particle solar receiver with dimensions. | 9 |
| Figure 6. A schematic of the improved small particle solar receiver.. | 10 |
| Figure 7. Map of heliostat field at NSTTF. | 14 |
| Figure 8. Variables for Martin Marietta Receiver Model. | 15 |
| Figure 9. Power reaching aperture plane vs. number of rays on 3/21. | 17 |
| Figure 10. Grid map..... | 18 |
| Figure 11. Grid map (zoomed in to the center)..... | 19 |
| Figure 12. Flux map at 12 pm on 3/21 with 23.8° tilt angle. | 20 |
| Figure 13. Flux map at 2 pm on 3/21 with 23.8° tilt angle. | 21 |
| Figure 14. Flux map at 4 pm on 3/21 with 23.8° tilt angle. | 22 |
| Figure 15. The power reaching the aperture plane vs. radius. | 23 |
| Figure 16. Power vs time depending on the radius on March 21st..... | 24 |
| Figure 17. Spectral irradiance vs. wavelength for air mass 1.5 and 37 degree tilted surface | 25 |
| Figure 18. Cumulative distribution function for wavelength (NREL solar spectrum, airmass 1.5)..... | 26 |
| Figure 19. Example of a binary search. | 27 |
| Figure 20. The possible incidents at the window..... | 29 |
| Figure 21. Log of absorptive index vs. wavelength using data from Pilon’s research. | 31 |
| Figure 22. Index of refraction vs. wavelength using data from Pilon’s research. | 32 |
| Figure 23. Refraction index and log of absorptive index using the fit equations for the data from Dr Pilon’s research. | 33 |
| Figure 24. Angles of incoming radiation and refraction..... | 35 |
| Figure 25. Reflection from the second interface..... | 36 |

| | |
|---|----|
| Figure 26. The effect of the cutoff number on absorptivity for 1 cm thick window with 0 degree incident angle. | 41 |
| Figure 27. The effect of the cutoff number on absorptivity for 2.5 cm thick window with 0 degree incident angle. | 42 |
| Figure 28. Optical properties of the window (1 cm thick, 0 degree incident angle). | 43 |
| Figure 29. Optical properties of the window (1 cm thick, 30 degree incident angle). | 44 |
| Figure 30. Optical properties of the window (1 cm thick, 60 degree incident angle). | 45 |
| Figure 31. Optical properties of the window (1 cm thick, 0.5 μm). | 46 |
| Figure 32. Optical properties of the window (1 cm thick, 3 μm). | 46 |
| Figure 33. Frequency of the incident angle of the incoming rays to the aperture plane on March 21th at 12 pm (16 million rays). | 47 |
| Figure 34. Optical properties of the window (2.5 cm thick, 0 degree incident angle). | 47 |
| Figure 35. Optical properties of the window in the solar spectrum (2.5 cm thick, 0 degree incident angle). | 48 |
| Figure 36. Optical properties of the window (2.5 cm thick, 0.5 μm). | 48 |
| Figure 37. Optical properties of the window (2.5 cm thick, 3 μm). | 49 |
| Figure 38. Optical properties of the window in the solar spectrum (1 cm thick, 0 degree incident angle). | 51 |
| Figure 39. Comparison of spectral transmissivities for 0 degree incident angle. | 52 |
| Figure 40. Comparison of absorptivities for 0 degree incident angle. | 53 |
| Figure 41. The comparison of absorptive coefficients. | 54 |
| Figure 42. The effects of OH- concentration on the absorptive index. | 55 |
| Figure 43. The optical properties of HOQ 310 from both the data taken from the vendor (blue line) and the calculated data (red, green, and black lines) (1 cm thick, 0 degree incident angle). | 56 |
| Figure 44. The optical properties of HSQ 300 (1 cm thick, 0 degree incident angle). | 57 |
| Figure 45. 60 degree spherical window (dimensions are in meters). | 59 |
| Figure 46. Cap angle. | 59 |
| Figure 47. Ellipsoidal window (dimensions are in meters). | 60 |
| Figure 48. Power vs. radius at the aperture plane considering the range of interest for the diameter of the window. | 60 |
| Figure 49. Global and local coordinate systems and the departure at the aperture plane. | 65 |
| Figure 50. Incident angle. | 68 |
| Figure 51. Zenith and azimuth angles for the reflected ray. | 69 |

| | |
|---|----|
| Figure 52. Power reaching the window vs. tilt angle on 3/21 at 12 pm..... | 72 |
| Figure 53. Power entering the receiver vs. tilt angle on 3/21 at 12 pm. | 73 |
| Figure 54. Power entering the receiver vs. tilt angle on 3/21 at 2 pm. | 74 |
| Figure 55. Frequency for ellipsoidal window..... | 75 |
| Figure 56. Frequency for 60 degree spherical window..... | 76 |
| Figure 57. Frequency for 45 degree spherical window..... | 76 |
| Figure 58. Absorption for different geometries and thicknesses (HOQ 310)..... | 77 |
| Figure 59. Transmission for different geometries and thicknesses (HOQ 310). | 78 |
| Figure 60. Reflective losses for different geometries and the thicknesses. | 79 |
| Figure 61. Transmission for different geometries and types of quartz..... | 80 |
| Figure 62 Absorption and reflection losses for different geometries | 81 |
| Figure 63. Absorption map for 60 degree spherical cap on 3/21 at 12 pm..... | 82 |
| Figure 64. Absorption map for 60 degree spherical window on 3/21 at 12 pm top view (looking from inside the receiver)..... | 83 |
| Figure 65. Absorption map for 60 degree spherical window on 3/21 at 4 pm. | 83 |
| Figure 66. Absorption map for 60 degree spherical window on 3/21 at 4 pm top view (looking from inside the receiver)..... | 84 |
| Figure 67. Absorption map for 45 degree spherical window on 3/21 at 12 pm. | 84 |
| Figure 68. Absorption map for 45 degree spherical window on 3/21 at 12 pm top view (looking from inside the receiver)..... | 85 |
| Figure 69. Absorption map for ellipsoidal window on 3/21 at 12 pm..... | 85 |
| Figure 70. Absorption map for ellipsoidal window on 3/21 at 12 pm top view (looking from inside the receiver)..... | 86 |

NOMENCLATURE

| | | | |
|-------------------|---|---|-------------------|
| HTMM1 | = | the height of the centre of the aperture plane | [m] |
| OFFSET | = | offset from the z axis at the power tower | [m] |
| DELTAD | = | tilt angle | [rad] |
| $area_i$ | = | area under direct circumsolar | [m ²] |
| a_i | = | location on the x-axis | [ND] |
| <i>total area</i> | = | total area under direct circumsolar | [m ²] |
| CDF_i | = | Cumulative Distribution Function | [ND] |
| \bar{n} | = | complex refractive index | [ND] |
| n_λ | = | refractive index | [ND] |
| k_λ | = | absorptive index | [ND] |
| $\tau_\lambda(S)$ | = | optical thickness | [m] |
| β_λ | = | extinction coefficient | [1/m] |
| κ_λ | = | absorption coefficient | [1/m] |
| σ_λ | = | scattering coefficient | [1/m] |
| S | = | path length | [m] |
| Wave | = | wavelength | [μm] |
| θ_1 | = | incident angle | [rad] |
| θ_2 | = | refraction angle | [rad] |
| r_\perp | = | perpendicular component of unpolarized radiation | [ND] |
| r_\parallel | = | parallel component of unpolarized radiation | [ND] |
| r | = | average of parallel and perpendicular component of unpolarized radiation | [ND] |
| τ_\perp | = | perpendicular component of the transmittance | [ND] |
| ρ_\perp | = | perpendicular component of the reflectance | [ND] |
| α_\perp | = | perpendicular component of the absorptance | [ND] |
| τ_\parallel | = | parallel component of the transmittance | [ND] |
| ρ_\parallel | = | parallel component of the reflectance | [ND] |

| | | | |
|----------------------|---|--|--|
| α_{\parallel} | = | parallel component of the absorptance | [ND] |
| I | = | spectral intensity | [W/($\mu\text{m}\cdot\text{m}^2\cdot\text{sr}$)] |
| L | = | thickness of the window | [m] |
| α | = | absorptivity (Equation 23) | [ND] |
| ρ | = | reflectivity (Equation 24) | [ND] |
| τ | = | transmissivity (Equation 25) | [ND] |
| α | = | defined variable (Equation 29) | [ND] |
| β | = | defined variable (Equation 30) | [ND] |
| γ | = | defined variable (Equation 31) | [ND] |
| a | = | defined variable (Equation 34) | [ND] |
| b | = | defined variable (Equation 35) | [ND] |
| Φ | = | cap angle | [rad] |
| r | = | radius of a sphere | [m] |
| cr | = | radius of the circle or window | [m] |
| P_0 | = | location of the emission | [m] |
| \vec{r}^g | = | direction of the incoming rays in global coordinate system | [ND] |
| PWT | = | power of a ray | [Watt] |
| $\vec{\gamma}(t)$ | = | parametric equation | [m] |
| t | = | scalar | [ND] |
| P_i | = | intersection point | [m] |
| \vec{F} | = | gradient of a function | [ND] |
| \vec{x}^l | = | local x axis | [ND] |
| \vec{y}^l | = | local y axis | [ND] |
| \vec{z}^l | = | local z axis | [ND] |
| [R] | = | translation matrix | [ND] |
| Ran | = | random number | [ran] |
| \vec{r}_{ref}^l | = | direction of a reflected ray | [ND] |
| θ | = | zenith angle (used before) | [rad] |
| φ | = | azimuth angle | [rad] |

ACKNOWLEDGEMENTS

First and foremost, I would like to thank my advisor Prof. Fletcher Miller for his support, encouragement, and guidance throughout the time I spent on this thesis. Dr. Arlon Hunt, who first introduced the concept of the small particle solar receiver, provided valuable comments on this research. It was a great pleasure working alongside both Prof. Miller and Dr. Hunt. The support and aid of my colleagues in the SDSU Combustion and Solar Energy Laboratory was invaluable. I would like to acknowledge Cliff Ho from Sandia National Laboratory for providing MIRVAL. I also would like to acknowledge Andrew Clarkson from L-3 Brashear for his comments about the window. I would like to thank my thesis committee, Dr. Randall German and Dr. Thais Alves, for their comments on the thesis. I also would like to thank Google.org for supporting my thesis research under grant agreement #32-2008. Last but not the least, I would like to thank the US department of energy for supporting my thesis research with its SunShot program under the grant agreement # DE-EE0005800.

CHAPTER 1

INTRODUCTION

Non-renewable resources are being used at alarming rates in order to fulfill our need for energy. In 2008, 87% of the energy that we consumed came from non-renewable resources, while only 10% of the energy came from combustible renewable resources such as wood, biogas etc. In the same year, 2.2% of our energy was generated by hydropower, and only 0.7% came from renewable resources such as geothermal, solar, wind, heat, etc [1]. Burning non-renewable resources and combustible renewable resources are contributing to global warming [2]. It has become clear that non-renewable resources will eventually be depleted. Considering these facts, the effort to discover clean energy is becoming more important every day. Developed countries have already started to pass laws to require the usage of renewable resources. Governor Brown, of California, has signed a law requiring that 33% of our electricity arise from renewable resources by the year 2020 [3]. Germany, who already leads the world on clean energy, set a goal to provide all of its electricity from renewable resources by the year 2050 [4]. These kinds of developments draw our attention to solar energy. There are several ways to make use of solar energy for practical ends, and solar power can potentially reduce energy costs. One approach is called concentrated solar power (CSP) systems.

CONCENTRATED SOLAR POWER SYSTEMS

Concentrated solar power systems use mirrors to focus solar radiation. Concentrated solar radiation is used to heat a working fluid which drives a turbine to generate electricity. CSP is now feasible after several decades of research. Compared to a natural gas plant, the total operation and maintenance cost of a CSP plant is 30% lower without the cost of natural gas. This does not include greater job creation [5]. The global stock of CSP plants reached 1GW capacity as of 2010. Many countries have projects in development. The total expected capacity of those in planning stages is 15 GW [6]. 11.3% of global electricity could be provided by CSP, with 9.6% from solar power directly and 1.7% with the help of back up fuels. CSP can significantly contribute to the world's energy supply. The Department of Energy has also started a program

called SunShot initiative [7]. The goal of this program is to lower the cost of solar electricity and make it competitive with the conventional forms of energy by 2020 [8].

There are four types of CSP technologies: parabolic troughs, dish/engine systems, Linear Fresnel reflectors and power towers. These systems can be categorized depending on the focus type, as line focus collectors and point focus collectors. Linear Fresnel Reflectors (LFRs) and the parabolic troughs have line focus collectors which mean that the collectors are lined in a single axis in order to make tracking the sun simpler. On the other hand, the dish/engine systems and the power towers have point focus collectors which mean that the collectors track the solar radiation along two axes to focus the solar radiation to a single point in order to achieve higher temperatures [5]. A schematic of each type of CSP technologies is shown below in Figure 1 [9]. One of the challenges with central receivers, however, is the receiver design. Current commercial receivers cannot sustain the highest fluxes that a heliostat field is capable of producing, especially if using a gas as the working fluid, which is the desired working fluid for a gas turbine offering higher efficiency than the Rankine systems in use today. Therefore, we, Combustion and Solar Energy Laboratory at San Diego State University (CSEL), have initiated research on an older concept for a gas-cooled receiver as described in the next section.

Parabolic trough systems consist of parabolic-shape mirrors that are curved in one direction. These mirrors are connected in a line and the system has several parallel rows of these lines. These lines can be 100 meters (m) or more long with the curved surface of 5 m to 6 m. The mirrors concentrate the solar radiation to its focal line to heat the fluid inside a tube which goes along the focal line of the mirrors. Synthetic oils are used in most of the existing applications as fluid but molten salt is under experimental tests in the new plants. The tube is generally is made of stainless steel and it is coated with a selective coating. This allows the device to effectively absorb solar radiation while hardly emitting it. The tube is also covered with vacuum jacket. It allows the solar radiation in freely while preventing thermal heat losses. The main objective is to minimize heat loss from the pipe [10].

Linear Fresnel reflectors (LFRs) are very similar to parabolic troughs. These systems use long, flat or slightly curved mirrors. The absorber tube is fixed and located on the focal point of the system as it is shown in Figure 1 [9]. An absorber tube has a secondary reflector on top of it that refocuses the rays missing the tube. When compared to parabolic troughs, LFRs have more advantages. LFRs use flat glass mirrors which are cheaper to produce and require less steel and

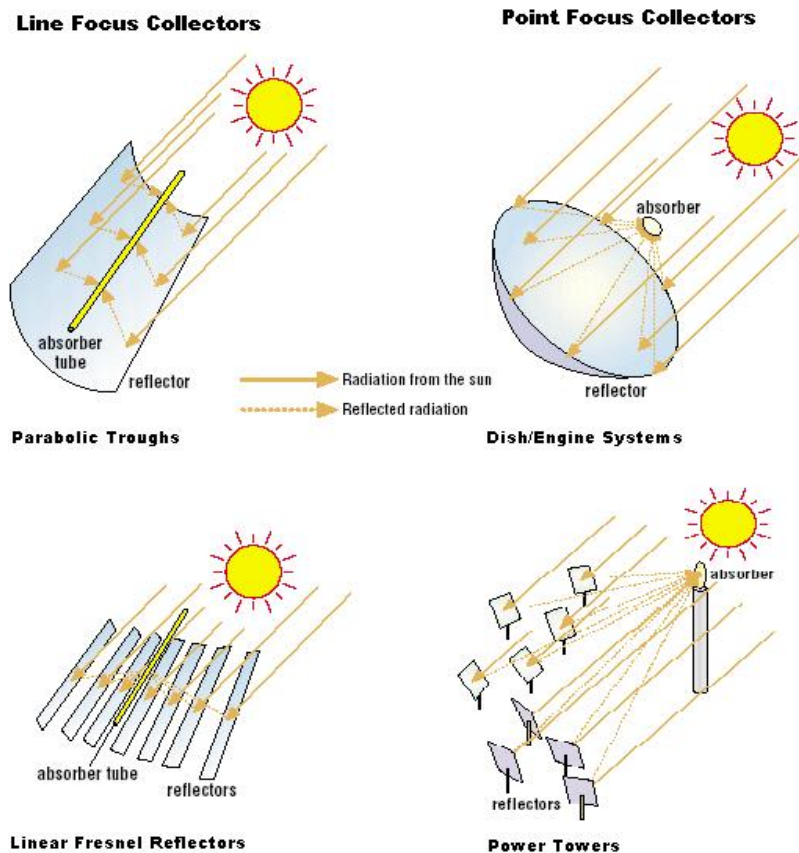


Figure 1. Types of concentrated solar power technologies.
Source: Volker Quaschnig. "Technology Fundamentals: Solar Thermal Power Plants." Last modified June 2003.
<http://www.volker-quaschnig.de/articles/fundamentals2/index.php>.

concrete which also lowers the cost. The wind loads on LFRs are less; therefore LFRs have better structural stability. Since the absorber tube is fixed, one disadvantage about LFRs is that optical efficiency is lower. Therefore, there are greater losses from the mirror due to the focus of radiation in the mornings and afternoons [10].

Dish/engine systems are also called parabolic dishes. Parabolic dishes concentrate the solar radiation to its focal point where there is a Stirling engine or a micro-turbine that generates electricity. These systems have the highest efficiency compared to the other CSP systems. Each parabolic dish system produces electricity independently and the capacity is in between 5 to 50 kW. This makes the system suitable for distributed generation [10].

Power towers use a field of heliostats to concentrate the solar radiation to the focal point of the heliostats. The heliostat is a computer-controlled device that consists of mirrors and moves

throughout the day in order to concentrate the solar radiation to a designated target, called the aim point. A receiver is located at the focal point on a tower called a power tower. The fluid flowing inside the receiver is heated by the concentrated radiation, with the details depending on the receiver design. The heat drives a thermodynamic cycle, generally a Rankine cycle, to generate electricity. Compared to the LFRs and parabolic troughs, power towers can reach higher temperatures. The reason is that more solar radiation is concentrated on a smaller surface which will reduce the heat losses. The thermodynamic cycles are more efficient when operating at higher temperatures. Therefore, higher efficiency can be achieved with power tower systems. Also, thermal energy storage systems are more efficient when operating at the higher temperatures. These potential advantages make the power tower systems more appealing. These systems could soon become the preferred CSP technology [10].

The current commercial CSP plants use a Rankine cycle to produce electricity. The reason is that they can reach high enough temperatures that lead to phase change, eventually requiring water cooling. CSP technology fits in dry desert climates where water is scarce. High temperatures can be reached with a small particle solar receiver to use a Brayton cycle. This method is more efficient compared to the Rankine cycle at higher temperatures because water cooling is not needed.

There are several commercial CSP plants using power tower technology. The first commercial plant, PS10, was built in Spain. The 11 MW plant has a storage unit and produces 23 GWh electricity annually. Solartres, which is also built in Spain, is 15MW commercial power plant. It also uses power tower technology and aims to produce 96 GWh electricity annually [11]. Another example to commercial CSP plants is Sierra SunTower which is 5 MW CSP plant and built in California [12]. There are also several power tower plants that are currently being built.

Depending on the receiver, a specific kind of working fluid is used by power tower systems. Air, steam or molten salt is used by the current systems. Working temperature of the fluid can be as low as 250 °C and as high as 1000 °C [10].

We, CSEL, are developing a new type of receiver for power tower CSP plants based on volumetric absorption by a gas-particle suspension in order to reach higher temperatures. The design of the receiver consists of a window which allows the solar radiation inside the receiver. There are several receivers with a window that have been developed.

SMALL PARTICLE SOLAR RECEIVER

The small particle solar receiver was first introduced by Hunt in the late 1970s [13]. The small particle solar receiver is a large vessel with a window that allows the radiation into the receiver. Inside the receiver, a gas-particle suspension flows. This suspension contains air and smoke-like (sub-micron) carbon particles. The solar radiation is absorbed volumetrically by the carbon particles. As the carbon particles absorb the solar radiation, the temperature of the particles increases. Therefore, they heat the gas by conduction, which is very effective due to their small size. Eventually, the temperature increase of the suspension causes the carbon particles to oxidize. This process yields a hot, pressurized gas for use in Brayton cycle [13]. A schematic of small particle receiver is shown in Figure 2.

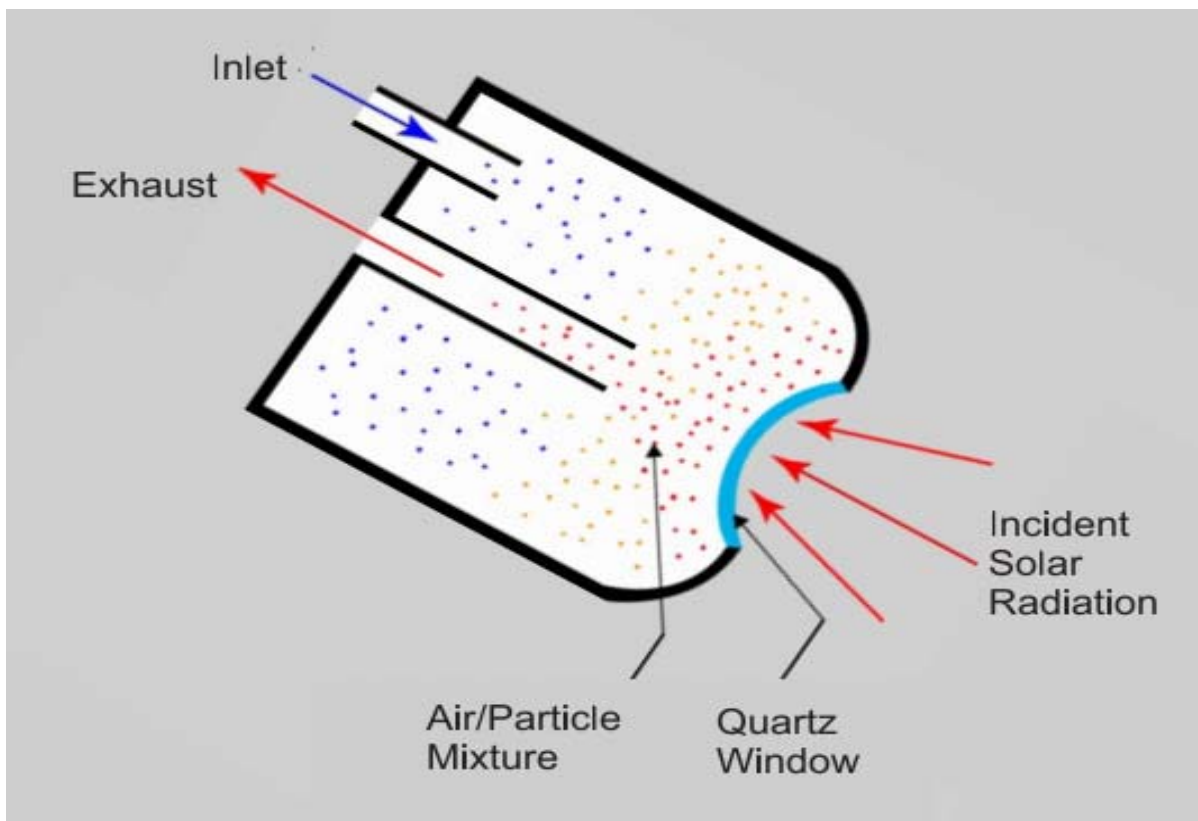


Figure 2. Schematic of a small particle solar receiver.

The small carbon particles have selective absorption characteristics, recognized by Hunt. The small carbon particles are good absorbers in the solar spectrum [13]. This is a great advantage since the most incoming radiation to the system is in solar spectrum. Hunt also pointed out that using small particles will provide a great surface area to enhance the heat transfer to the gas. The

optical efficiency of the small carbon particles was defined as the fraction of solar radiation absorbed by the particles as opposed to the fraction that is scattered out through the window. The optical efficiency was greater than 96% as it is analytically calculated by Hunt [13].

The first experimental test was performed at 30 kW scale in 1982 by Hunt and Brown. Results showed that the temperature of the air and carbon particle mixture was 1000 K. It was recognized that the window was successfully used, although the system was not pressurized and the window was flat in this receiver [14]. Later on in 2004, a 10 kW receiver was tested with different type of gases. The temperature of the gas – carbon particle mixture reached to 2000 K when air was used. The window was cooled when operating the system and the transmissivity of the window was measured 87% [15]. There were not any problems reported about the window. Later on in 2008, this very solar receiver was tested in Isreal, which will be mentioned in the following chapter.

WINDOWED RECEIVERS

There are several examples of windowed receivers that are built and tested. A volumetric air cooled receiver has been built and tested under a research program by the German Aerospace Center (DLR) [16, 17]. The receiver is designed for solar-hybrid gas turbine and combined cycle systems and operates at 15 bar. It has a secondary concentrator at the inlet where the solar radiation enters the system right before the quartz window. An absorber is put behind the window. The cold air enters the absorber and gets heated up volumetrically through the absorber then exits the system. The exit temperature of the hot air is between 800 °C and 1000 °C [17]. As it has been shown at the simulation results, the receiver is capable of reaching 80% efficiency with the help of a secondary reflector. A schematic of the receiver is shown below in Figure 3 [16].

Another example of a windowed receiver has been developed and tested at the Weizmann Institute in Israel [18]. The receiver has a quartz flat window and the transmission of the window was measured 87%. Concentrated solar radiation enters the receiver through the window. The radiation is absorbed volumetrically in the receiver by the working fluid that is mixed with carbon particles. Due to thermal stability and high absorption in the entire solar spectrum, carbon particles were chosen to mix with the working fluid. Two working fluids were used: nitrogen and air. The energy flux of the concentrated solar radiation was up to 3 MW/m² and the size of

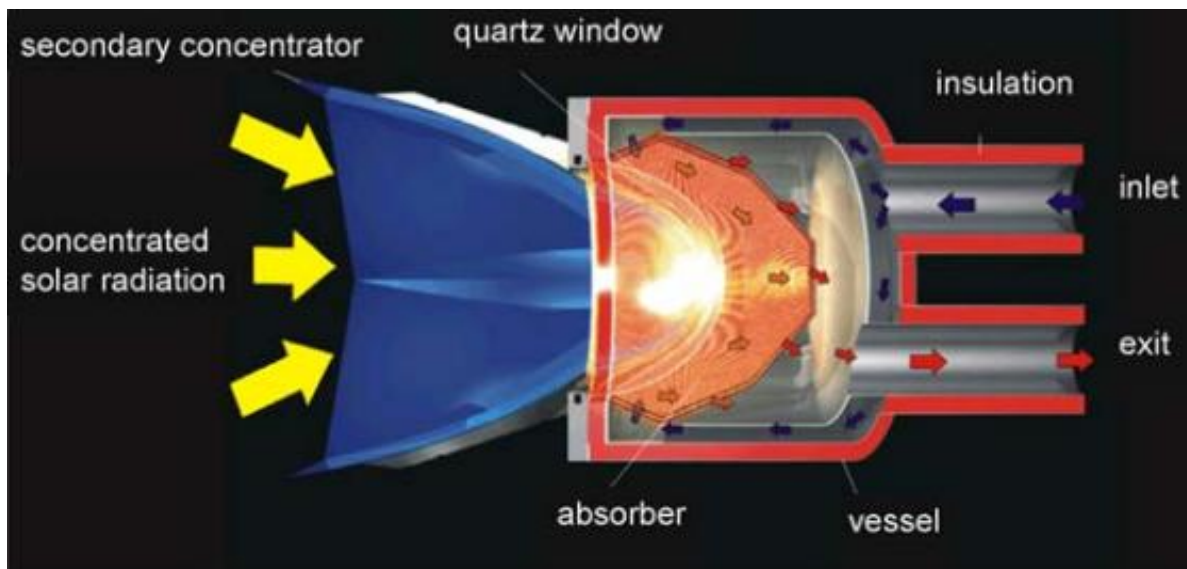


Figure 3. Schematic of pressurized high-temperature DLR receiver. Source: Buck, Reiner, Eckhard Lüpfer, and Félix Tellez. "Receiver for Solar-Hybrid Gas Turbine and CC Systems (REFOS)." Paper presented at the 10th SolarPACES International Symposium on Solar Thermal Concentrating Technologies, Sydney, Australia, 2000.

carbon particles was around $3\ \mu\text{m}$ in the experiments. The temperature of the working fluid was in between 1343 K and 2118 K depending on the partial pressure ratio of the working fluid, the working fluid type, and the particle loading. The schematic of this receiver is shown in Figure 4 [18]. Reaching high temperatures in the system will bring a major problem which is overheating the quartz window. This major problem will be discussed later. The design of this particular receiver is very similar to the receiver that we are designing which will be explained in the following section.

The Combustion and Solar Energy Laboratory at San Diego State University is currently working on modeling and designing a 5 MWth pressurized small particle solar receiver [19]. The prototype will be built under the SunShot grant awarded by Department of Energy. The small particle solar receiver then will be tested at National Solar Thermal Test Facility (NSTTF).

There have been several numerical simulations of small particle solar receivers. The first study, using a five-flux radiation model, was done by Miller in 1988, who modeled a lower temperature pipe flow system and compared it to lab-scale experiments [20]. In 2010 a detailed radiation study was performed by Steven Ruther, using the Monte Carlo Ray Trace Method and an assumed slug flow fluid dynamics model [21]. The dimensions for the small particle solar receiver were chosen based on an estimate of the heliostat field at the National Solar Thermal

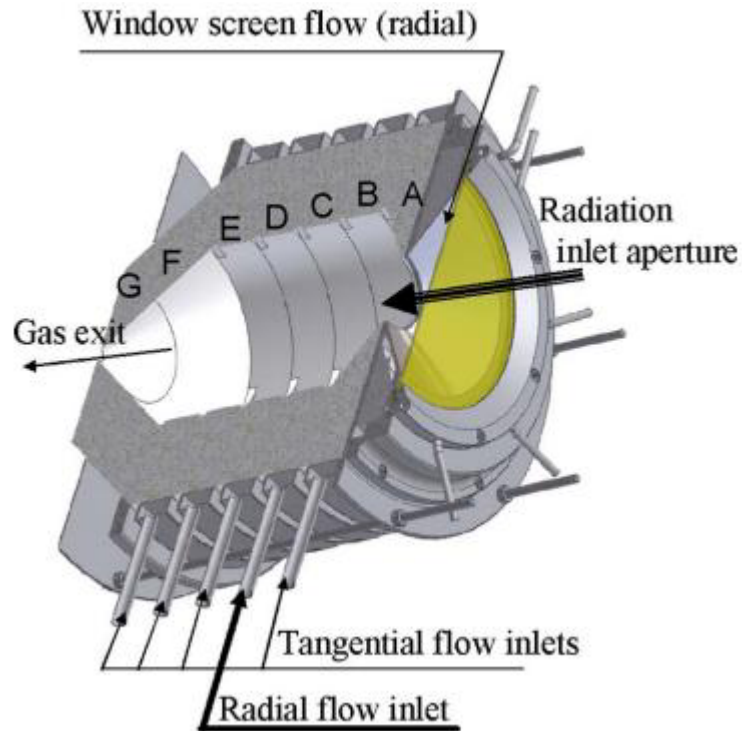


Figure 4. Schematic of the receiver that is tested at Weizmann Institute in Israel. Source: Klein, Hanna Helena, Rachamim Rubin, and Jacob Karni. “Experimental Evaluation of Particle Consumption in a Particle Seeded Solar Receiver.” *Journal of Solar Energy Engineering* 130, no. 1(2007): 011012-8.

Test Facility (NSTTF). The heliostat field can focus 5MW solar radiation on a 3 meter diameter circle on the power tower. The window diameter was picked 3 meter based on this fact. A schematic of the small particle solar receiver with dimensions as modeled is shown below in Figure 5 [21].

Two different studies were performed depending on the flow direction. Cocurrent flow (black arrows in Figure 5) which means the direction of the solar radiation and the air-carbon particle suspension is the same. Counter current flow (blue arrows in Figure 5) which means the direction of the solar radiation and the air-carbon particle suspension are opposite to each other. The interior wall properties for the receiver were based on the aluminum oxide model or they were modeled as black walls. The window for the receiver was flat with a transmissivity of 1 for ease of modeling. This means whenever a ray will hit the window it will be transmitted through the window. The incident radiation coming from the heliostat field was 5MW. The direction incident radiation was either collimated or set to be diffuse a 45° cone angle. This angle better

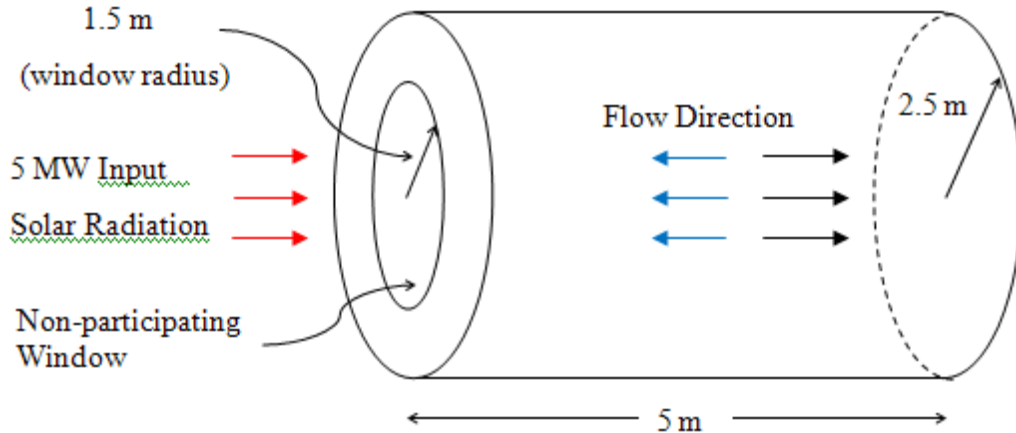


Figure 5. A schematic of the small particle solar receiver with dimensions. Source: Ruther, Steven James. “Radiation Heat Transfer Simulation of a Small Particle Solar Receiver Using the Monte Carlo Method.” Master’s Thesis, San Diego State University, 2010.

represents the incident radiation from the heliostat field, since an actual heliostat field model was not available at the time.

Along with the parameters that have been discussed above, particle diameter and mass loading were also varied to find most efficient cases. Three different particle diameters were chosen: 0.2, 0.5, 1.0 μm . Mass loading was varied from 0.15 to 0.60 g/m^3 . Depending on all these parameters, the temperature of the working fluid for different cases was varying from 1300K to 1600K [21].

Later on, this research was improved by Crocker, by adding in more realistic flow calculations [22]. The geometry of the small particle solar receiver was changed as it is shown below in Figure 6 [22]. An outlet tube was added to the receiver with a diameter of 0.6 m. Only counter current flow was studied in Crocker’s model since it showed better results compare to the concurrent flow study in Ruther’s model. The MCRT method was used to solve for the solar radiation and create a source term. A model in FLUENT was built and coupled with MCRT. This model will be well-suited to couple with the model, described in this thesis, for the window since they both use MCRT method. The uniform solar irradiation assumed previously was changed to a Gaussian flux distribution to more accurately represent the concentrated solar flux at NSTTF. The diameter and the transmissivity of the window were not changed but the window temperature was set to 1000K. Other parameters mentioned for Ruther’s model were not changed and different cases depending on these parameters were studied. The temperature of the working fluid for different cases was varying from 1300K to 1500K [22].

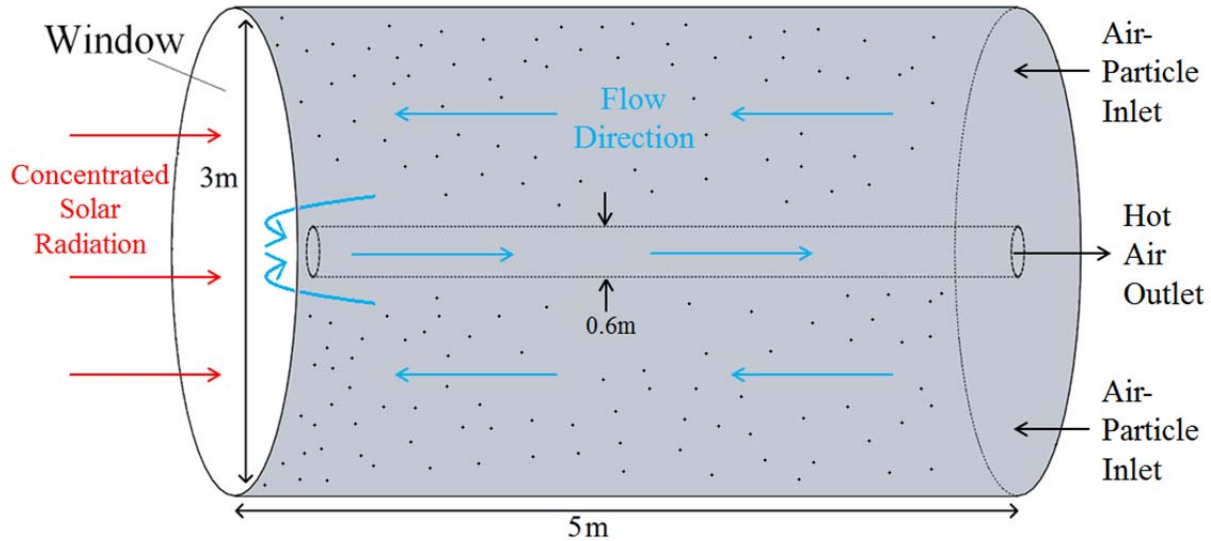


Figure 6. A schematic of the improved small particle solar receiver. Source: Crocker, Adam. “Coupled Fluid Flow and Radiation Modeling of a Small Particle Solar Receiver.” Master's Thesis, San Diego State University, 2012.

Most recently, the 2-D model of Crocker has been extended to 3-D by del Campo [23]. This will allow coupling of the window and heliostat field model described in this thesis (which are 3-D) to the receiver model.

MONTE CARLO RAY TRACE (MCRT) INTRODUCTION

Modeling the radiation transfer inside a particle receiver is a formidable task, and improved receiver design requires accuracy beyond the initial flux model developed by Miller [20]. This led to the development of Monte Carlo models of the receiver as described above (Ruther, Crocker, Fernández), and which is used in this thesis for modeling the heliostat field and the window. The Monte Carlo method is a statistical approach to investigate problems by creating applicable random numbers and considering probability distributions. The Monte Carlo method was first used in radiation heat transfer (the Monte Carlo Ray Trace) in 1964 by Howell and Perlmutter [24]. One-dimensional gray participating media between infinite parallel plates was considered in the paper. The method was applied to this case and the results were validated against the conventional approach. It was mentioned in the paper that the MCRT method can be used easily in more complex cases which can be difficult to solve by standard analytical techniques [24]. Later on, complex cases were investigated by Howell [25]. The results have shown that the MCRT method is flexible enough to be applied to the complex case but the computation time gets longer as the case gets more complex. MCRT method has also been

proven that it can be adapted to parallel computation which will reduce the computation time. Also, computing time is becoming a less of an issue as the computer technology is developing [25].

Several computer codes have been built to calculate the solar flux concentration in concentrated solar power systems, and three of these use the MCRT method [26]. Tonatiuh was created to do optical simulations [27]. SolTRACE aims to model complex optical systems. MIRVAL was developed for optical performance analysis for Solar One project by Sandia National Laboratories [26]. The flux calculation from heliostat field to the power tower is essentially a radiation exchange from surface to surface. A similar method is used here to calculate the radiation that is transferred from the aperture plane to the window.

OVERVIEW OF THIS THESIS

One of the purposes of this research is to determine the solar heating loads that a real window would have and thereby develop a more realistic receiver/window model that can be used for design. In the model described above, Figure 6, the window is flat with the transmissivity of 1. As shown by Mande [28], a flat window is not possible in this pressurized situation unless it is very thick. The thickness should be kept as small as possible since higher thickness will lead higher absorption on the window. High absorption will heat up the window. The window should be kept under 1000 K to operate properly. Mande discusses concave window shapes that can withstand the pressure by remaining in compression, and these shapes are modeled here optically. Additional modeling of the window as a structural element is currently being reported by Saung [29].

The flat window with a transmissivity of 1 was used in the previous models because those models were developed to study the radiation and fluid dynamics inside the receiver, not the window. In reality, there will be some absorption and reflection at the window surface and this affects what happens inside the receiver. A Fortran code was developed to calculate the optical properties of the window as part of this research. This code accounts for rays reaching the window from arbitrary directions with arbitrary wavelengths.

The other purpose of the research is to have a more realistic solar radiation input to the receiver. In the models by Crocker and Ruther, the solar input was modeled as either collimated or evenly distributed over a 45 degree cone half angle. In the Ruther model, there was no spatial

variation across the aperture plane, while in the Crocker model a Gaussian distribution was considered. In reality, however, the direction of the radiation will be different depending on the day of the year, time, location of the receiver, and the heliostat field, etc. MIRVAL is modified and used to consider all these affects in order to get a realistic solar radiation input for the conditions of National Solar Thermal Test Facility (NSTTF) in Albuquerque, NM. As mentioned earlier, the Combustion and Solar Energy Laboratory at San Diego State University will test the prototype of a small particle solar receiver at NSTTF once it is built under the SunShot grant award by Department of Energy.

Once the two models described above were developed, they were coupled and used to determine the transmission, absorption, and reflective losses for different window geometries as well as different grades of quartz. Different tilt angles for the receiver were also studied to obtain highest transmission at the window. Absorbed flux was mapped for different window geometries. Finally, power reaching the windows throughout the day and the year were studied.

CHAPTER 2

MIRVAL

As mentioned earlier, MIRVAL is a computer code developed by Sandia National Laboratories in 1979. It is updated by Akiba Segal in 1995. MIRVAL is capable of computing the solar thermal input to a solar receiver from heliostats as well as simulating and evaluating the performance of different heliostats by using the Monte Carlo Ray Trace method. It was first used in order to evaluate competing designs for heliostats, heliostat field layout, and receivers in Solar One project. Under the Solar One project, 10 MW pilot plant was built near Barstow, California [30].

MIRVAL is obtained by personal communication from Cliff Ho [31]. This is the main reason why MIRVAL was picked for this research. One other reason is the availability to study annual performances. Also MIRVAL is written in Fortran which makes it easier to couple with the in-house codes since they are also written in Fortran. Last but not the least, the directional variation in MIRVAL is another reason MIRVAL was picked.

MIRVAL offers many subroutines that are already built in, for different types of heliostats and the heliostat fields such as north facing or surrounding. Since MIRVAL is handling the calculations for heliostats and power towers in the subroutines, it is easy to modify the necessary subroutine in order to apply MIRVAL for different designs that need to be investigated.

There are four different subroutines for four different types of heliostats in MIRVAL. The heliostats were designed by Boeing, Honeywell, Martin Marietta, and Mc Donnell Douglas. The heliostats are controlled by a guidance motor. The guidance motor rotates the heliostats in two axes depending on the position of the sun.

The reflectivity of the mirrors on the heliostat field is defined with the variable ABSMIR. The value of this variable is easy to change and is set to 0.91. The reflectivity of all the mirrors in the system is assumed to be the same. It is independent of the incident angle or the wavelength of the incoming radiation. It should be noted that the mirrors are not flat.

There is another program called BOX which is a part of MIRVAL. BOX is used to map the heliostats field. MIRVAL can only be used after BOX creates the map of heliostat field [30]. BOX was modified by Dom Rumbolo, who is a member of Solar and Combustion Energy Laboratory at San Diego State University, according the map of heliostat field at NSTTF. The heliostat field contains 218 individual heliostats. Each heliostat has 25 mirrors on it. The map of the field is shown in Figure 7. Figure 7 is obtained via personal communication from Cliff Ho [31]

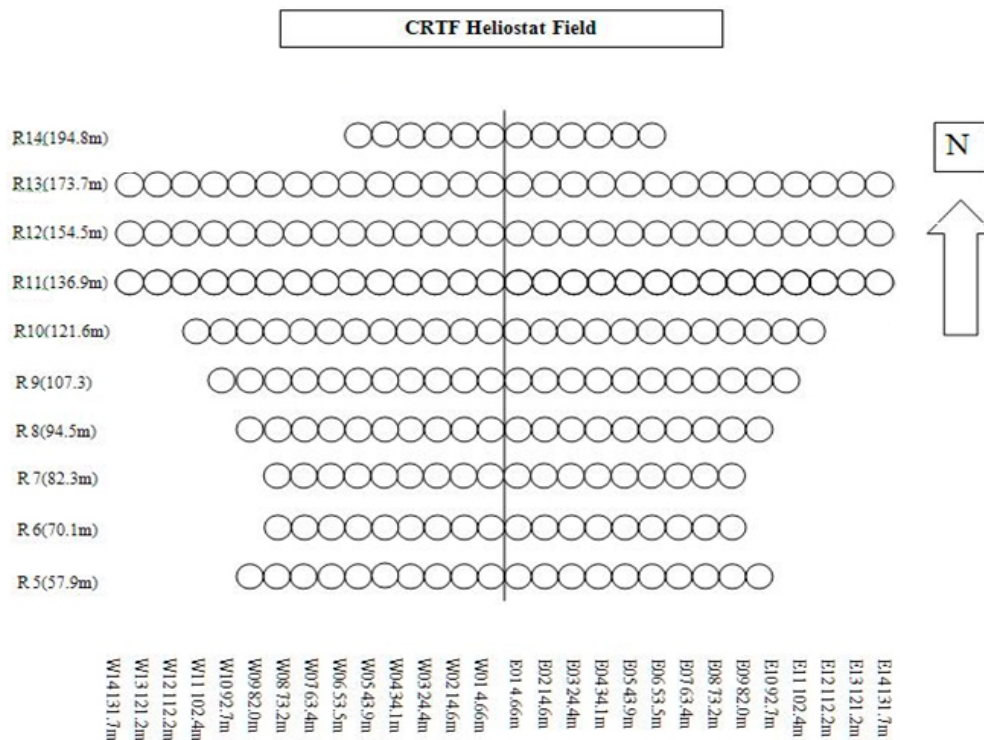


Figure 7. Map of heliostat field at NSTTF. Source: Ho, Cliff. E-mail Message to Author, October 2012.

There are three different subroutines for three different types of receivers. The design of the receiver is chosen according to the design of the heliostats. These designs are created by Honeywell, Mc Donnell Douglas, and Martin Marietta [30]. The Martin Marietta is a cavity-type receiver. It has a north-facing aperture. The solar radiation is concentrated to this aperture. The Martin Marietta design is very similar to the NSTTF design since they are both north-facing fields. Therefore, this model was used in this thesis. There are several input variables which represent the location of the aperture as it is shown in Figure 8 [30]. These variables were chosen according to the NSTTF sizes. HTMM1 the height of the center of the aperture plane is 60

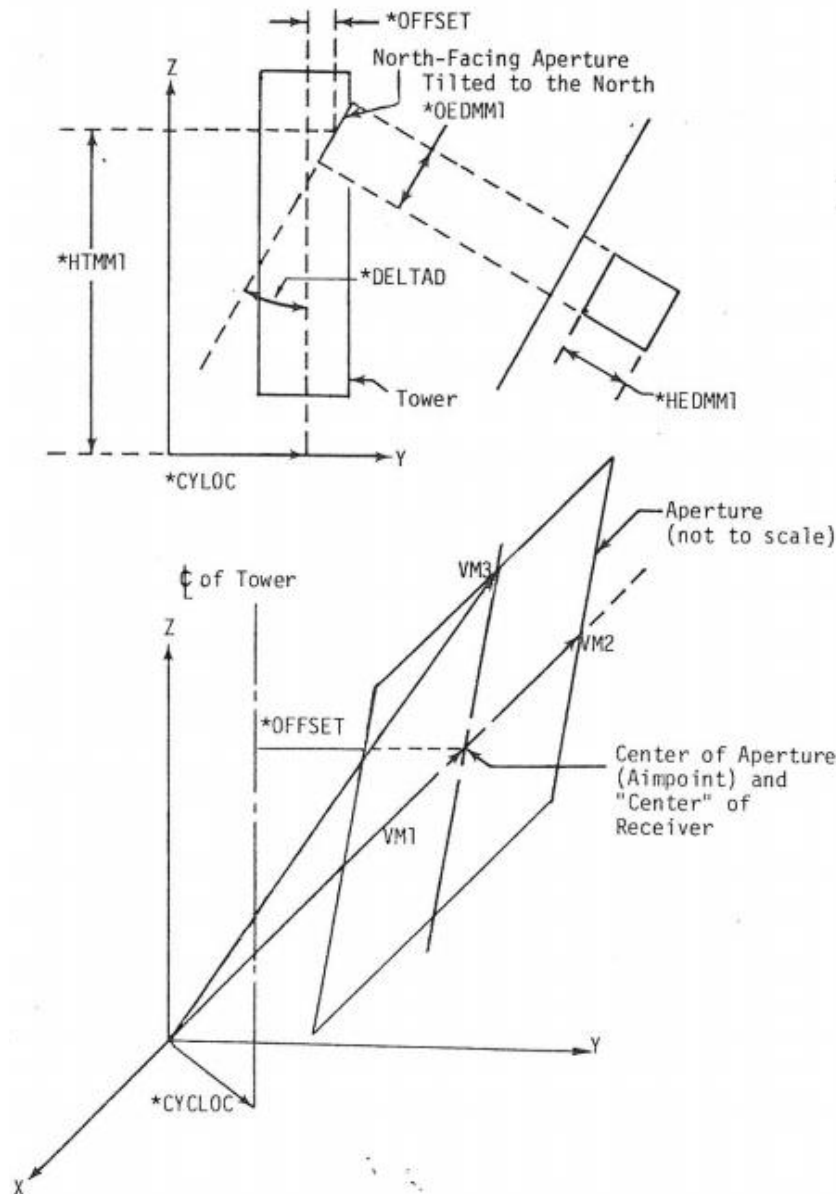


Figure 8. Variables for Martin Marietta Receiver Model.
Source: Leary, P. L., and J. D. Hankins. *User's Guide for MIRVAL: A Computer Code for Comparing Designs of Heliostat-Receiver Optics for Central Receiver Solar Power Plants* (SAND-77-8280). Livermore, CA: Sandia National Laboratory, 1979.

meters. OFFSET, which is the offset from the z axis, is 7.5 meters. DELTAD, the tilt angle, is 23.8° from the vertical. This angle was chosen to aim the aperture to right in the middle of heliostat field. It is only used to determine the flux map at the aperture plane. Later on, different tilt angles will be studied to obtain the highest transmission for different window geometries.

HTMM1 and OFFSET were kept the same throughout this research. Aperture plane is the plane at the power tower where the solar radiation is concentrated.

In power tower systems, the heliostats are fixed to the ground. This might cause shadowing which means a heliostat can block the neighboring heliostat depending on the position of the sun. The power towers are also fixed and the distance from the heliostats to the tower is quite far. Therefore, incoming radiation might be absorbed along the way when there is a participating medium in between such as dust particle in the air. In this work, the affect of the participating medium is not considered. Also optical aberration, beam spread due to finite sun size, cosine effect, fine scale errors in the mirror surface and spillage due to errors in mirror tracking, which means the incoming radiation is successfully reflected but missed the receiver, can be seen. MIRVAL is sophisticated enough so all of these events are considered. The MIRVAL default settings are used for these events.

MIRVAL has the flexibility for different types of runs depending on user's need. A collective run is used when there is no need to calculate the performance of subgroups of mirrors but the whole field. The main purpose is to cut down the competition time. On the other hand, the discrete run would be the best choice when the performance of an individual mirror is needed. There is also subdivided run which is used when the performance of a group of mirrors needed. Another option is to do the analysis over time; for that the energy run is used. The user chooses the starting time and stopping time as well as a sun elevation limit then MIRVAL produces the result averaged over the chosen time. Last but not the least, if the user is interested in the performance of the field at a specific time of day and year then the power run is performed [30].

THE ACCURACY OF MIRVAL

By the nature of MCRT method, the accuracy of the results depends on the number of rays. The results will be more accurate as the number of rays increase. An increase in the number of rays will lengthen the computation time. As mentioned earlier, computing time is becoming a less of an issue as the computer technology is developing. Despite this fact, the computation time is still a big issue for this work since the runs are performed on a personal computer. Therefore, the adequate number of rays should be determined before performing different cases. This study is the very first and the key study that is done by using MIRVAL in this research.

One way of determining the adequate number of rays is to have one big grid cell at the aperture plane and calculate the power reaching this cell. This method should be repeated for different hours of the day and for different number of rays. The value of the power should asymptote as the number of rays increase. Thus, the adequate number of rays can be determined when the power asymptotes. It can be clearly seen from Figure 9 that the power reaching aperture plane asymptotes around 10000 rays. Therefore, an adequate number of rays for one grid is 10000 on March 21st for different times.

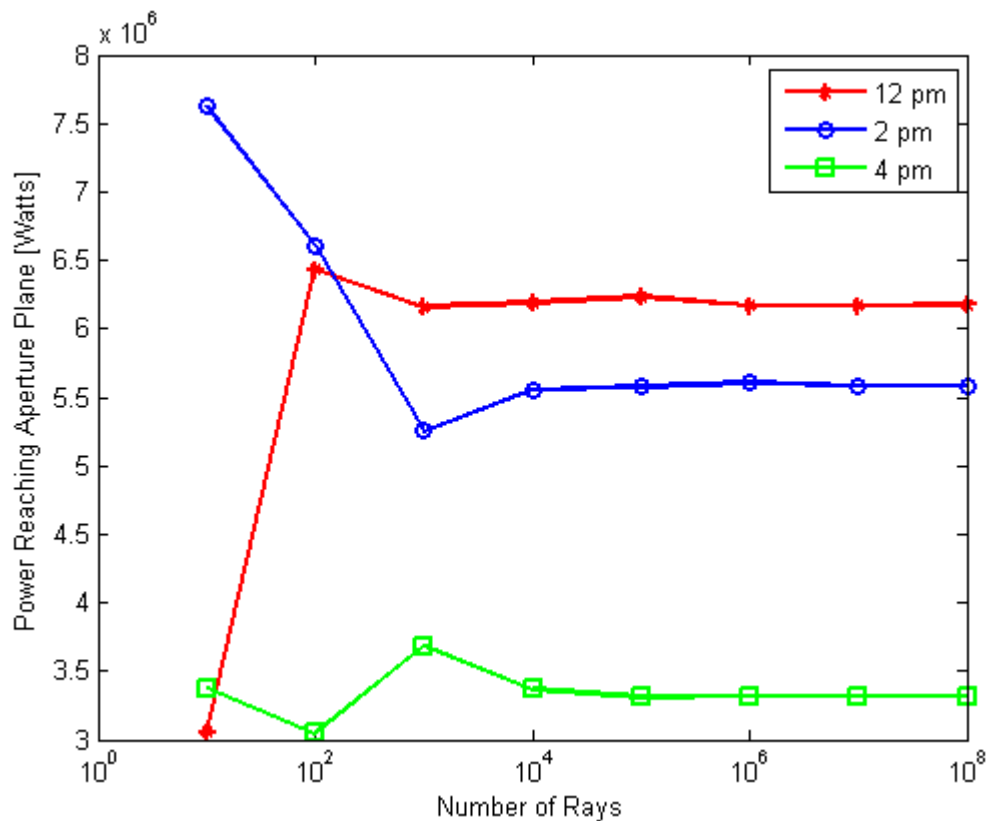


Figure 9. Power reaching aperture plane vs. number of rays on 3/21.

Now that an adequate number of rays per grid is known, the flux map can be created. First, the number of grid cells should be defined. The flux map will look smoother with more grid cells. For a better display and a better spatial resolution, 1600 grid cells were created. The grid map is shown in Figure 10. In order to get accurate results, at least 16 million rays ($1600 * 100000$) are needed. When MIRVAL is run with certain number of rays per grid cell, MIRVAL assigns power for each ray depending on the number of rays and carries on with the calculations per ray. After the calculations, MIRVAL gives the location of each ray that is hitting the aperture

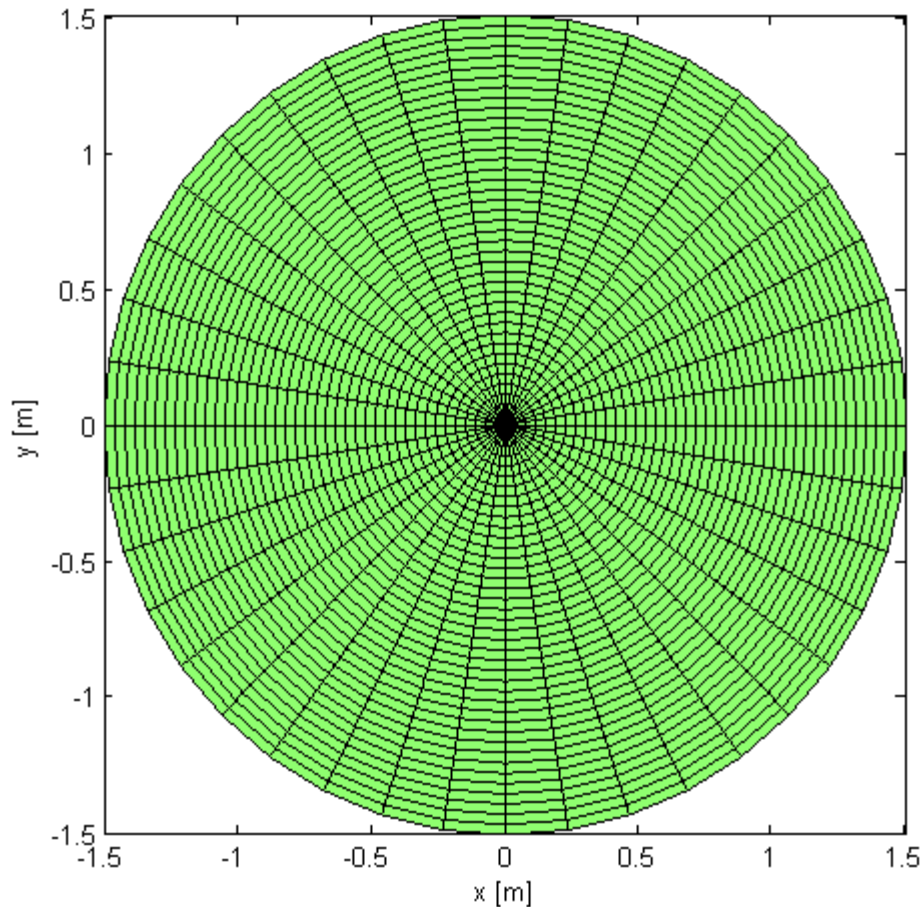


Figure 10. Grid map.

plane in Cartesian coordinate system along with the power. These data are stored in a file. A Fortran code is developed to read the file and assign each ray to the appropriate grid cell in polar coordinate system and calculate the power per grid cell. The polar coordinate system is chosen to simplify the calculations.

The grid map is shown in Figure 10. The radius for the aperture plane (not the window) was picked to be 1.5 m for the illustrative purposes. The center of the grid map can be seen in Figure 11.

There are several reasons why the flux map at the aperture plane is needed. One of the reasons is to have a better understanding of how well the concentrated flux is focused. Another reason is to figure out the location of the highest concentration and how it changes throughout the day. Third reason is that the value of the highest flux can be determined, which can be a limiting factor for many receivers. Last but not the least, the size of the window should be determined and the flux map is a good start to determine the range that the size of the window

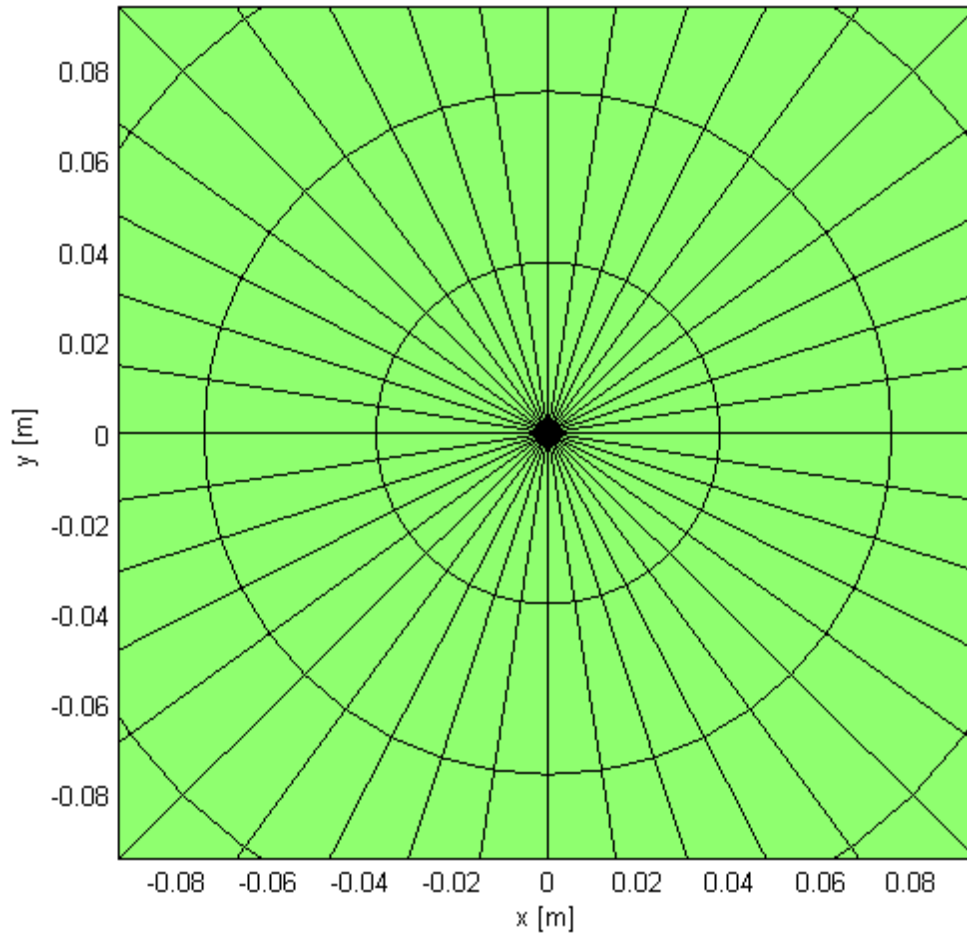


Figure 11. Grid map (zoomed in to the center).

should fall in. The rays are traced beyond the aperture plane until they meet the window which is behind the aperture plane unless the window is flat.

The following 3 figures (Figures 12-14) are the flux maps for different times on March 21st. March 21st is the first equinox day of the year. The tilt angle for each flux map is 23.8°. This angle was picked because the normal from the origin of the aperture plane points right in the middle of the heliostat field. The purpose is to get a better concentration at the origin of the aperture plane. Once again, the radius for the aperture plane (not the window) was picked to be 1.5 m for illustrative purposes. There are rays that fall out of this range. They were not considered because the number of these rays is approximately 4% of the total rays. The area that they fall in is much larger than the rest of the rays. Therefore, the heat flux in that area is very low compare to the rest. For this reason, it will not make a difference to show the heat flux after 1.5 m radius. For the flux map studies, 200 million rays were used which means 125000 rays per

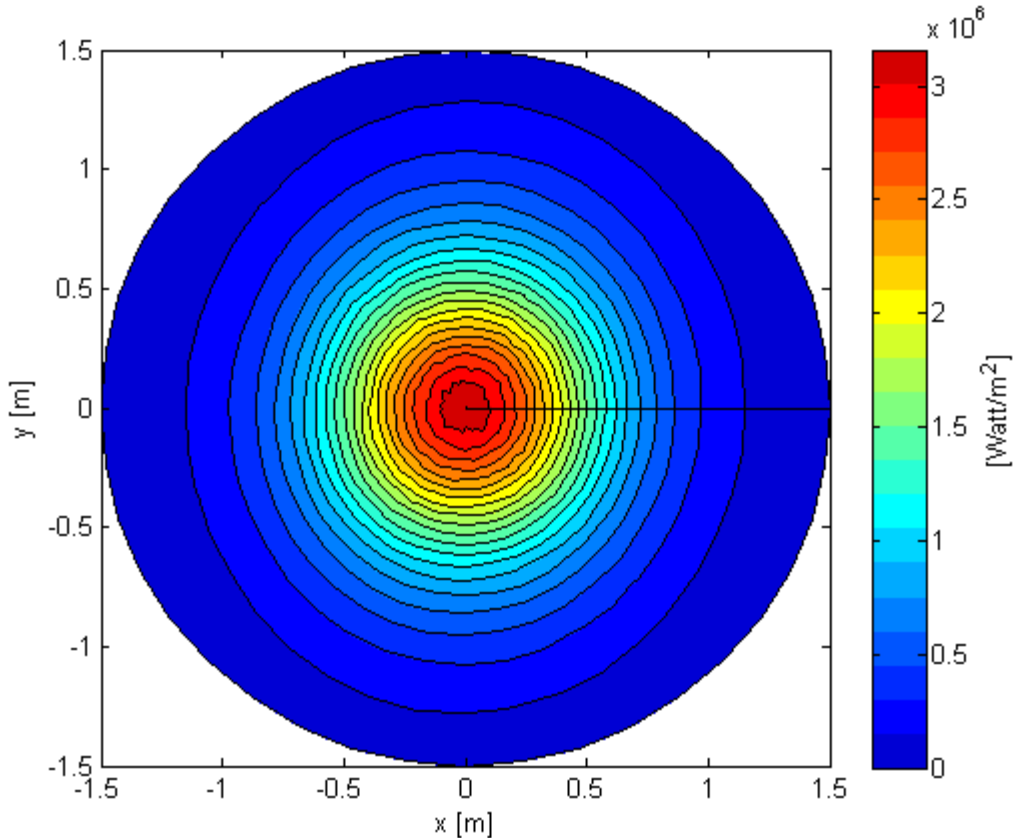


Figure 12. Flux map at 12 pm on 3/21 with 23.8° tilt angle.

grid cell since there are 1600 grid cells. As mentioned earlier, at least 100000 rays are needed per grid cell for accurate results.

Among the studied times, the highest heat flux is reached at 12 pm and the value of it is 3.2 MW/m^2 . The lowest peak flux is reached at 4 pm and the value of it is 0.9 MW/m^2 . The change in time does not have a significant effect on the location of the heat flux concentration but the change in power is drastic. Therefore, this change should be investigated more carefully.

Figure 15 has been created to show how much power is captured on the aperture plane with respect to the radius. This graph is for March 21st and the tilt angle is 23.8° . There were three different times studied. It can be easily seen among the chosen times the power is higher at 12 pm and lower at 4 pm. The bigger radius at the aperture plane will have a bigger surface area and that will allow more light capture, although it will also increase the receiver losses.

The window for the solar receiver will be located where the aperture plane is in order to let the solar radiation inside the solar receiver. It is obvious by looking at Figure 15, that if the

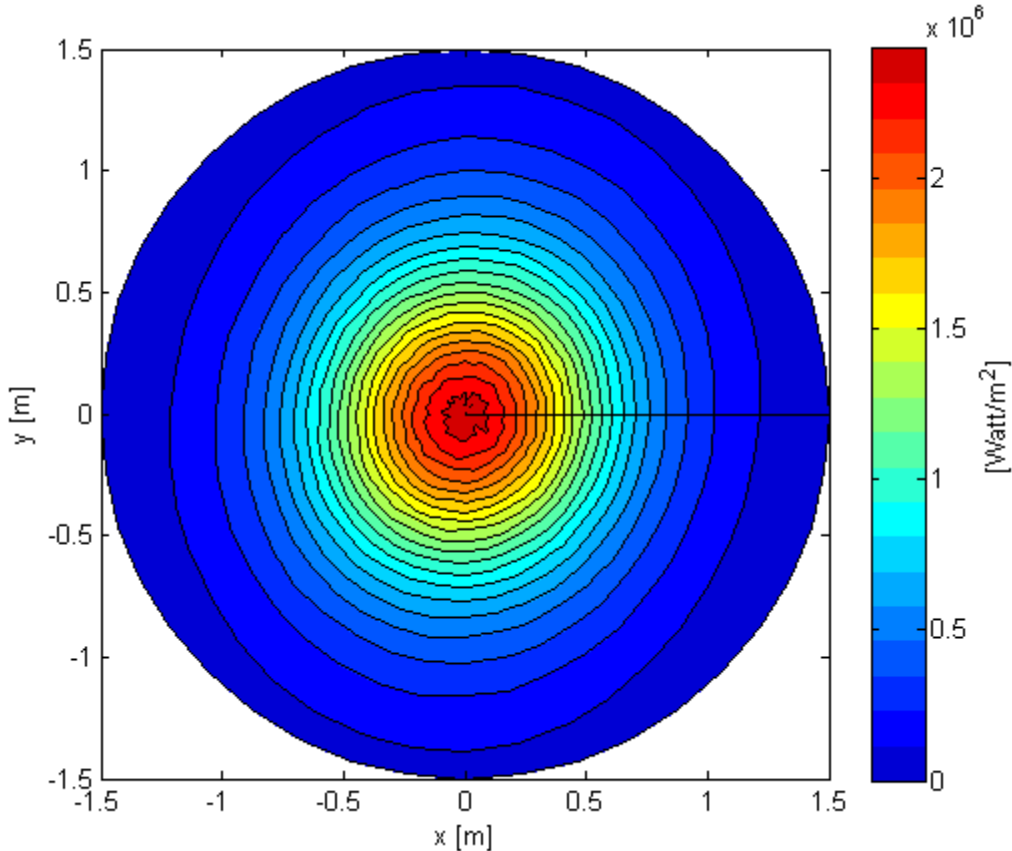


Figure 13. Flux map at 2 pm on 3/21 with 23.8° tilt angle.

radius of the window is bigger than more radiation will enter the receiver. More radiation means more energy captured inside the receiver. The bigger radius will create some issues. One of the issues is that there will be radiation coming from inside of the receiver and leaving the receiver from the window, representing radiation losses. Without a detailed receiver model coupled to the window model, it is not possible to determine the optimal window diameter, though clearly the advantages of a larger window begin to decrease at about 1 m. This is something under current research by our group. The other issue is high cost of quartz, and of fabricating large quartz windows, currently being studied by Saung [29]. Quartz is a very expensive type of glass. More material needs to be used for a bigger radius window. All of these factors should be studied very carefully in order to find the optimum radius for the window. Here we consider the solar flux on the window, but not the window cost or the losses from inside the receiver.

The power reaching the aperture plane changes throughout the day as well as the power reaching the window. It is expected that, the power will be less early in the mornings and in the late afternoons. The power reaching the window will depend on the radius of the window at the

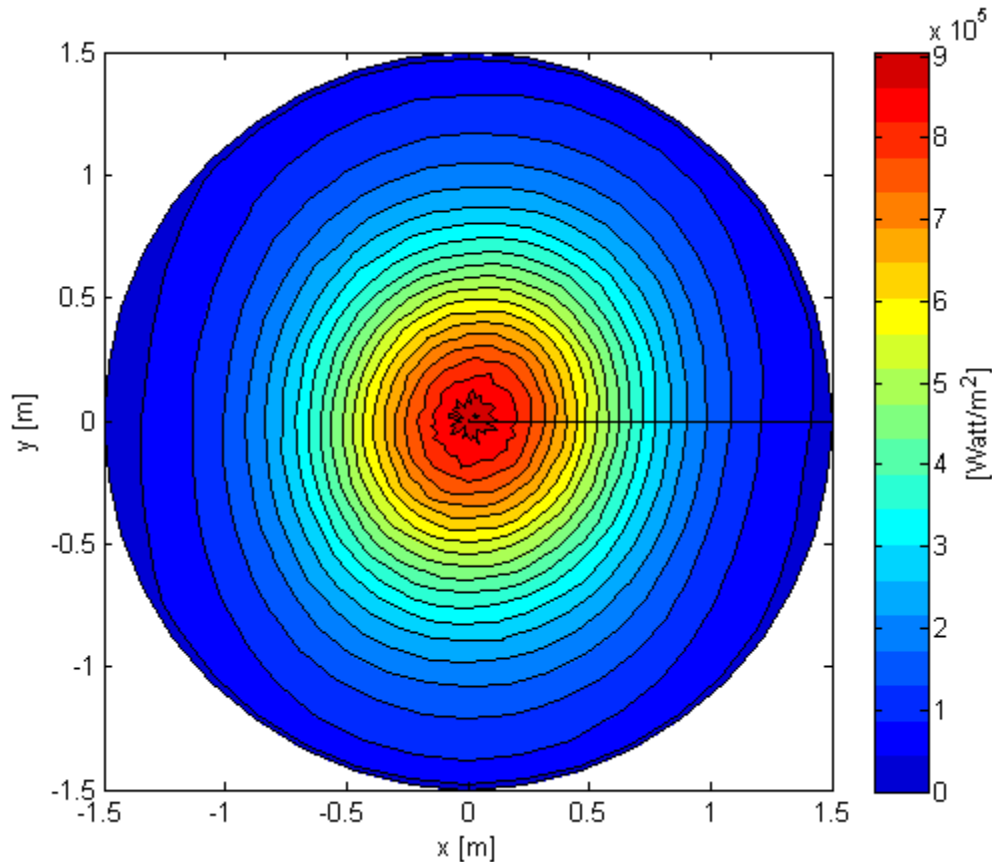


Figure 14. Flux map at 4 pm on 3/21 with 23.8° tilt angle.

aperture plane. Figure 16 shows the power reaching the window with respect to both time and the radius of the window at the aperture plane. Radius of the window was varied from 0.75 m to 12.5 m. Considering a window with a 0.85 m radius, which is the base case radius for my studies, power throughout the day can be as high as 4.4 MWatts and as low as 1.9 MWatt between 8 am to 4 pm.

It is important to point out that the increment in power is decreasing as the radius is increasing despite the equal increment in the radius. The reason is that the solar radiation is highly concentrated to the middle of the aperture plane as it can be seen from the flux map studies shown in Figure 12, Figure 13, and Figure 14.

SPECTRAL VARIATION

MIRVAL does not need the spectral variation for the ray trace, because the mirrors are treated as gray surfaces. However, optical properties of the window such as the transmissivity, the absorptivity, and the reflectivity depend on the wavelength of incoming radiation since the

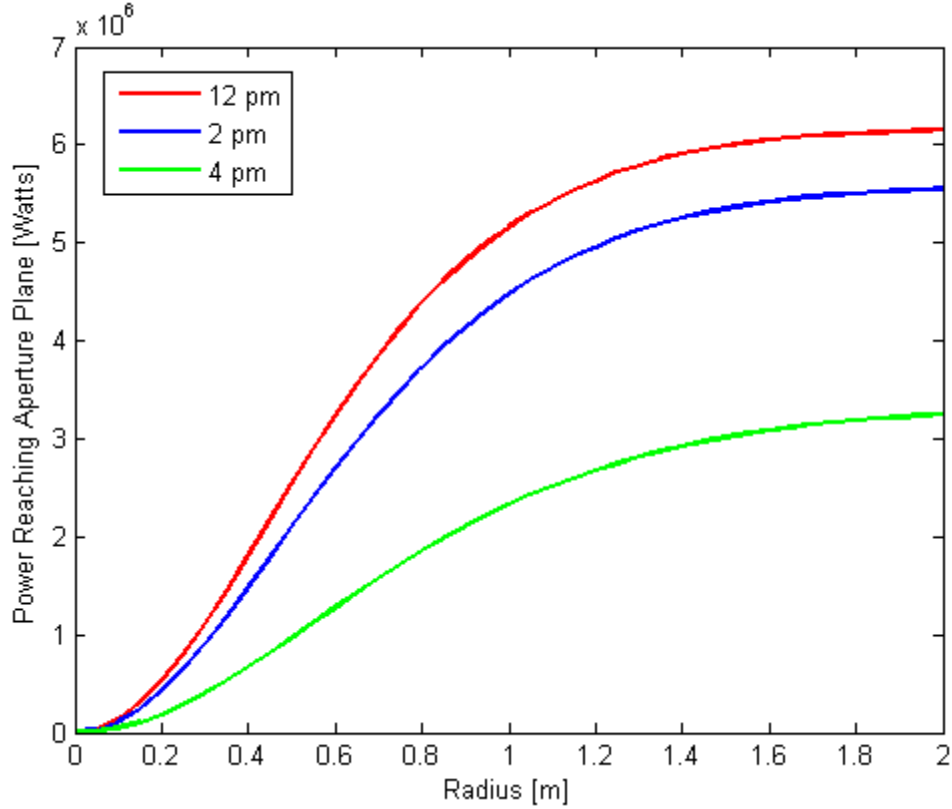


Figure 15. The power reaching the aperture plane vs. radius.

window is a non-gray (spectral) surface. A wavelength is needed to be assigned for each ray. Therefore, MIRVAL is modified to account for the wavelength.

Whenever a ray hits the window a cumulative distribution function (CDF) is used to determine the wavelength. A random number is used to sample the CDF. This CDF is created by using the data for direct circumsolar irradiance, shown in Figure 17 [32]. A sample of the data is given in Table 1 [32]. The data for irradiance is measured at air mass 1.5 which represents the path length of the solar radiation in the atmosphere. The vertical angle of the surface of the measurement device is 37 degrees.

The area under the red line from Figure 17 can be approximated by using the trapezoidal method. The area for each interval is divided by the total area. These values corresponds different wavelength intervals. Thus, the CDF is created. The equations used as followed:

$$area_i = \int_{a_i}^{a_{i+1}} f(x) \approx (a_{i+1} - a_i) * \frac{f(a_{i+1}) - f(a_i)}{2} \quad (1)$$

$$total\ area = \sum_{i=1}^N area_i \quad (2)$$

$$CDF_i = \frac{area_i}{total\ area} \quad (3)$$

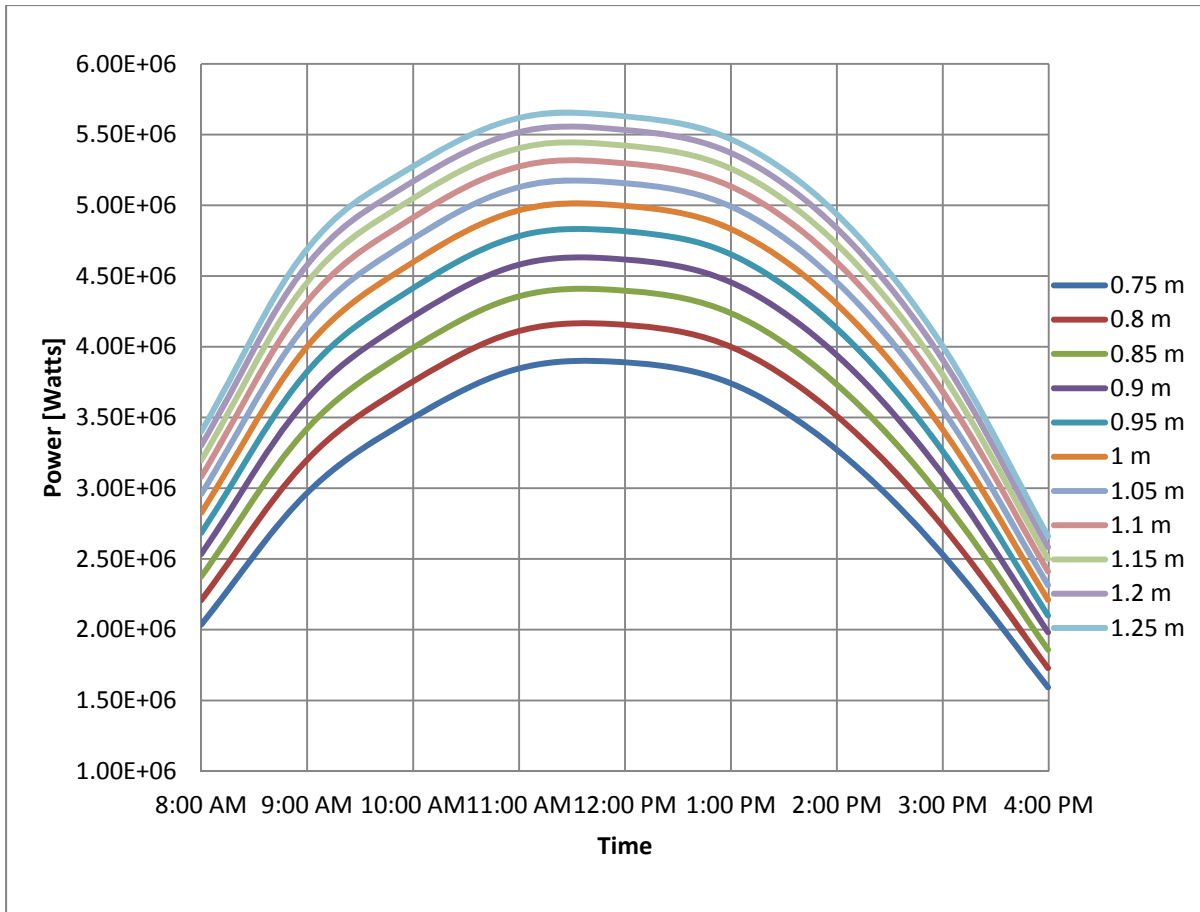


Figure 16. Power vs time depending on the radius on March 21st.

Using equations 1-3, Figure 18 is obtained.

Finally, a random number, representing the cumulative distribution function, is picked to determine the wave length. The interpolation approach is chosen for the numerical inversion of the cumulative distribution function. It used data tables directly. After a random number, between 0 and 1, is picked, it searches and finds what rows it falls in the CDF data. Then, the wavelength is determined by interpolating in between those rows.

A simple search technique would be to start at the first row and continue down the column until the bounding rows are found. This technique would be time consuming for large columns. The binary search algorithm is a much faster method for large sets of increasing numbers, which is sometimes referred to as a bisection method [33]. The algorithm checks to see if the random number is greater or less than the median of the set. The portion of the set that is higher than the median is discarded when the random number is smaller than the median. The

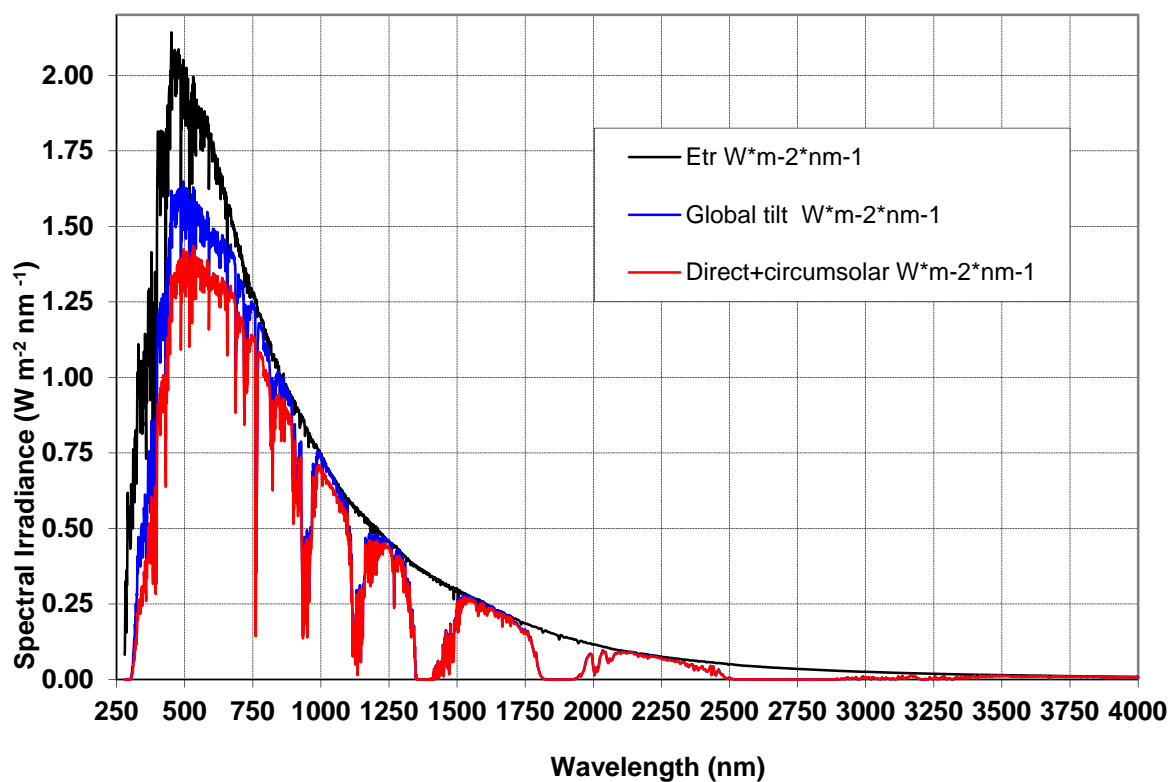


Figure 17. Spectral irradiance vs. wavelength for air mass 1.5 and 37 degree tilted surface Source: American Society for Testing and Materials. “Reference Solar Spectral Irradiance: Air Mass 1.5.” Accessed April 26, 2013. <http://rredc.nrel.gov/solar/spectra/am1.5/>.

Table 1. Direct Circumsolar Irradiance with Respect to Wavelength

| Wavelength (nm) | Direct Circumsolar Irradiance (W/(m ² *nm ²)) |
|-----------------|--|
| 425.0 | 9.9312E-01 |
| 426.0 | 9.6667E-01 |
| 427.0 | 9.3550E-01 |
| 428.0 | 9.4625E-01 |
| 429.0 | 8.7766E-01 |
| 430.0 | 7.0134E-01 |

Source: American Society for Testing and Materials. “Reference Solar Spectral Irradiance: Air Mass 1.5.” Accessed April 26, 2013. <http://rredc.nrel.gov/solar/spectra/am1.5/>.

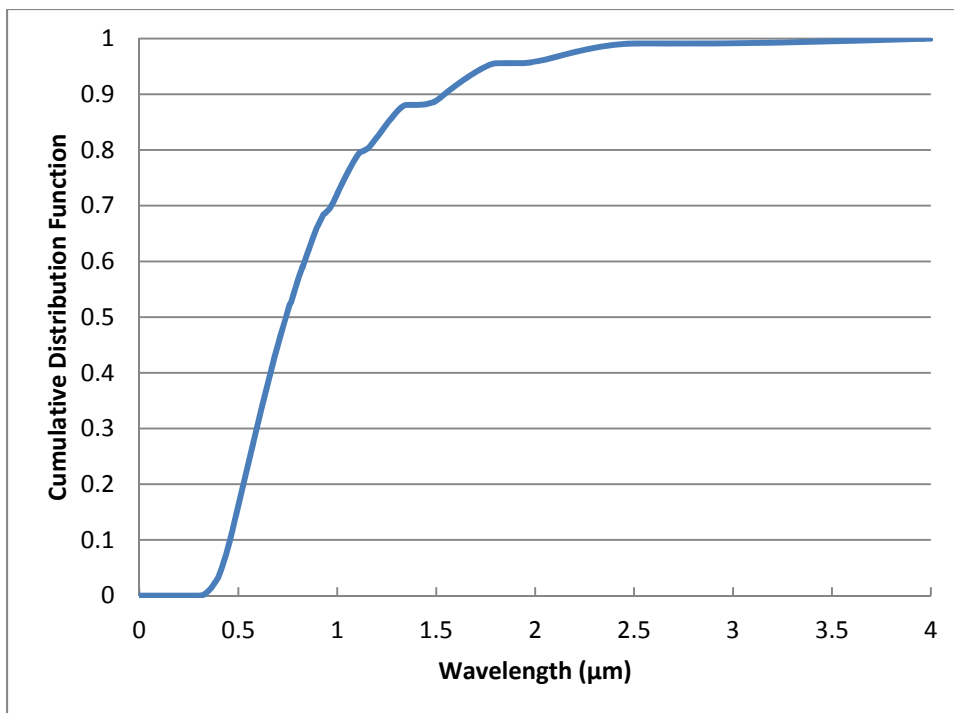


Figure 18. Cumulative distribution function for wavelength (NREL solar spectrum, airmass 1.5).

portion of the set that is smaller than the median is discarded when the random number is higher than the median. This process is repeated until the row bound the random number is identified.

An example is shown in Figure 19. The data used in the figure is obtained from the actual CDF. A random number is picked as 0.7. The median for the second column is 0.8885. Since the random number is smaller than the median, the portion of the set that is higher than the median is discarded. Same process is repeated until row bound the random number, 3th and the 4th rows, are identified. The wavelength is defined as 0.9636 by using the linear interpolation.

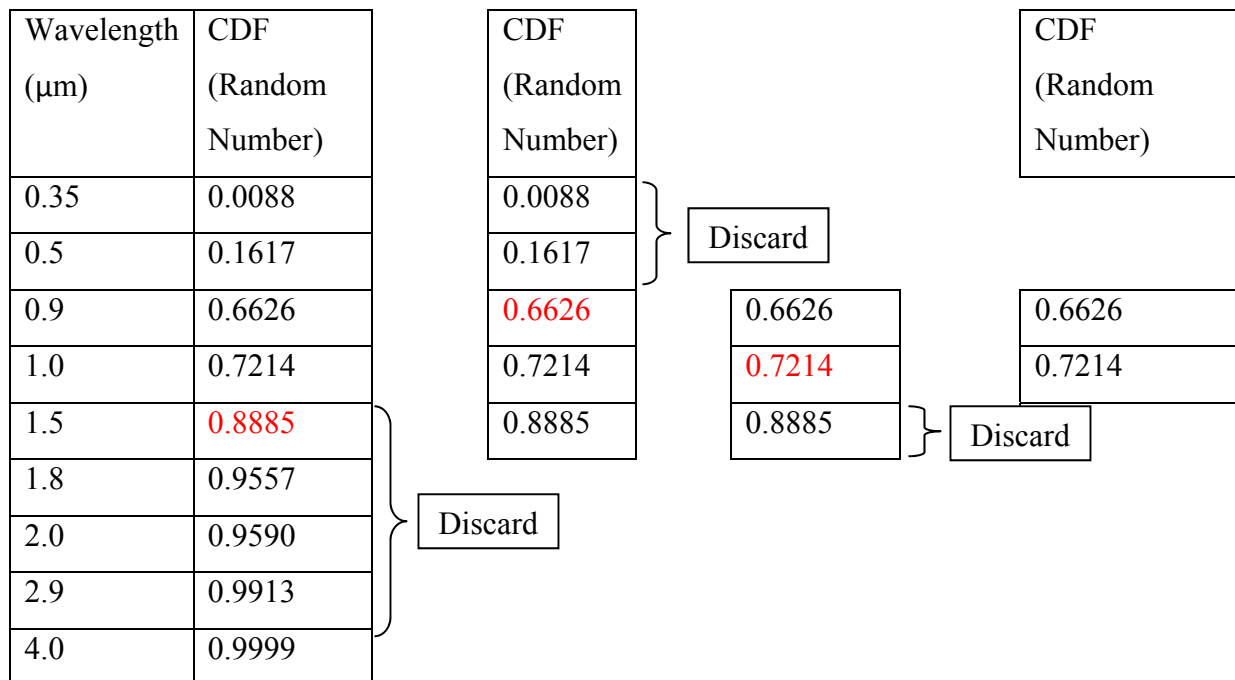


Figure 19. Example of a binary search.

CHAPTER 3

OPTICAL PROPERTIES OF THE WINDOW

In Chapter 2, we have seen the importance and capabilities of MIRVAL. It was mentioned that the heliostat field reflects the sun light to its focal point (aperture plane) where there is a solar receiver with a window located. MIRVAL tracks the rays till the aperture plane. The location and the direction of the rays at the aperture plane are taken from MIRVAL as output. As mentioned spectral variation is added to the MIRVAL. At this point we know enough information about the incident rays to track them all the way to the window thus receiver. We also know that the gap of the curved window is placed to the aperture plane. The rays will be tracked from the aperture plane to the window. One thing missing is the optical properties of the window such as the transmissivity, reflectivity and absorptivity. These optical properties will let us determine the fate of the incoming rays. In other words, these rays will tell us how much radiation will be transmitted, absorbed, and reflected.

There are several processes that will occur at the window after the sun light hits the window. The light can be reflected from the first interface of the window and can hit the window again or leave the system. The light can also get through the first interface and be absorbed by the window or it might reach the second interface of the window. After reaching the second interface two different possibilities occur. One is the light might get transmitted through the window and enters inside the solar receiver. Second is the light might be reflected back. The reflected light might be absorbed by the window or might reach the first interface. Later it might get transmitted and leave the system or might be reflected back to the window and the same incidents might occur. Figure 20 shows all the possible incidents that might occur at the window.

There is also radiation coming from the inside of the receiver hitting the window. The incidents that will occur are the same. Optical properties of the window called the absorptivity, the reflectivity, and the transmissivity are needed in order to keep track of the light at the window. Those properties will then be used to determine the fate of the light at the window. In other words, they will be used to see if the light is transmitted through the window or is absorbed or reflected by the window.

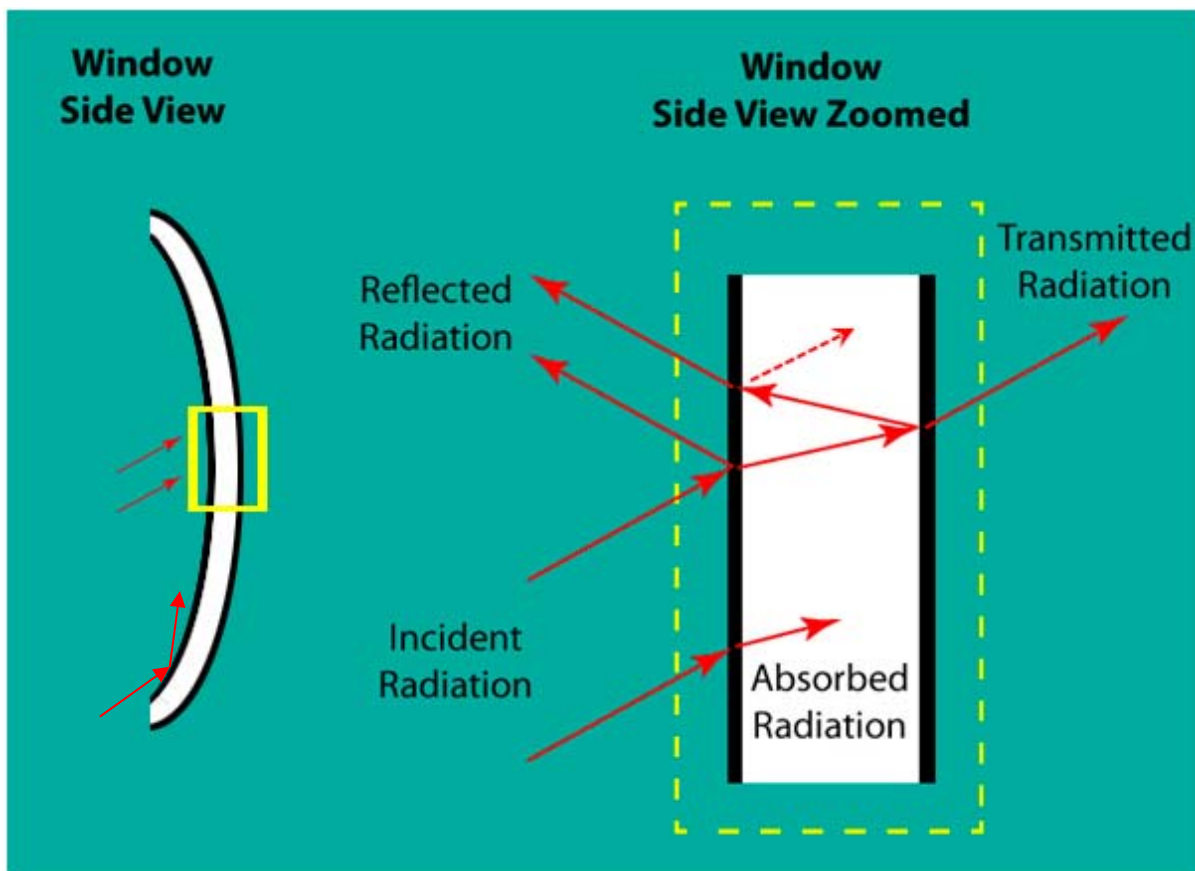


Figure 20. The possible incidents at the window.

The absorptivity is the fraction of the incident radiation on a body that is absorbed by the body. The transmissivity is the fraction of the incident radiation crossing through the body. The reflectivity is the fraction of the incident radiation that is reflected by the body. These optical properties are a function of the wavelength and direction of the incident radiation, and the refractive index and the absorptive index of the material. The material of the window is quartz, but the type or grade of quartz will have a large effect on the optical properties, and that will be discussed in detail here.

Much research has shown that quartz is a selective material which has a high transmissivity in the solar spectrum. Selective material means that the material behaves differently (and beneficially) depending on the wavelength of the incident radiation. Incoming radiation from the heliostat field will be in the solar spectrum. Therefore, high transmissivity in the solar spectrum is needed in order to let as much as radiation inside the receiver. This is one reason why quartz was chosen for the material of the window. The solar spectrum range is in between 0.2 μm to 2.5 μm , Figure 17.

THE INDEX OF REFRACTION AND THE ABSORPTIVE INDEX

Fused quartz is an imperfect dielectric material. A perfect dielectric material does not absorb any incident radiation. Fused quartz glass does, like all real materials, absorb some incident radiation due to the hydroxyl (OH⁻) and metallic impurities, among other things. In addition, quartz possesses some intrinsic absorption beyond 4 μm due to resonance of Si-O-Si. The absorption peaks between 9 μm and 9.5 μm because of asymmetric stretching of Si-O-Si bridges [34]. The amount it absorbs depends strongly on the wavelength and also on the thickness of the glass. In such a material, the incident radiation is attenuated as it passes through the medium. Attenuation in the medium is expressed by replacing the index of refraction of the medium with a complex refractive index \bar{n} . The imaginary part k_λ is called the absorptive index and n_λ is called the index of refraction [35].

$$\bar{n}_\lambda = n_\lambda - ik_\lambda \quad (4)$$

The refractive index and the absorptive index are needed to determine the optical properties such as the absorptivity, the reflectivity, and the transmissivity. The index of refraction is the ratio of the speed of light in the vacuum and in the medium. The absorptive index is a measurement of how radiation gets absorbed in the medium. They are both functions of the wavelength of the radiation and the temperature of the material. The data for these two properties are an excerpt from Dr. Laurent Pilon's research [34]. In the paper, it is shown that most of the experiments are done at room temperature. The effect of the temperature on these properties is not as significant as wavelength.

In Figure 21 and Figure 22, it is shown that much research has been done on the index of refraction and the absorptive index. The data has been reviewed within a wavelength range of 0.1 μm to 50 μm. Most of the values of the absorptive index and the index of refraction in a particular wavelength match in different studies or they are close enough. But in some of the research papers the data are not in agreement. Fit equations in these graphs are needed for calculation purposes. The outliers are taken off, resulting in the graph shown in Figure 23, to obtain a single valued function which is necessary to get accurate polynomial fit equations as well as the wavelength range. Later on, a few data points will be compared with the data from the vendor for several grades of glasses. The effects of the wavelength differ greatly with regard to the index of refraction and the absorptive index as it is seen in the graphs. It is important to find the appropriate wavelength range, since no single fit can cover the entire spectrum.

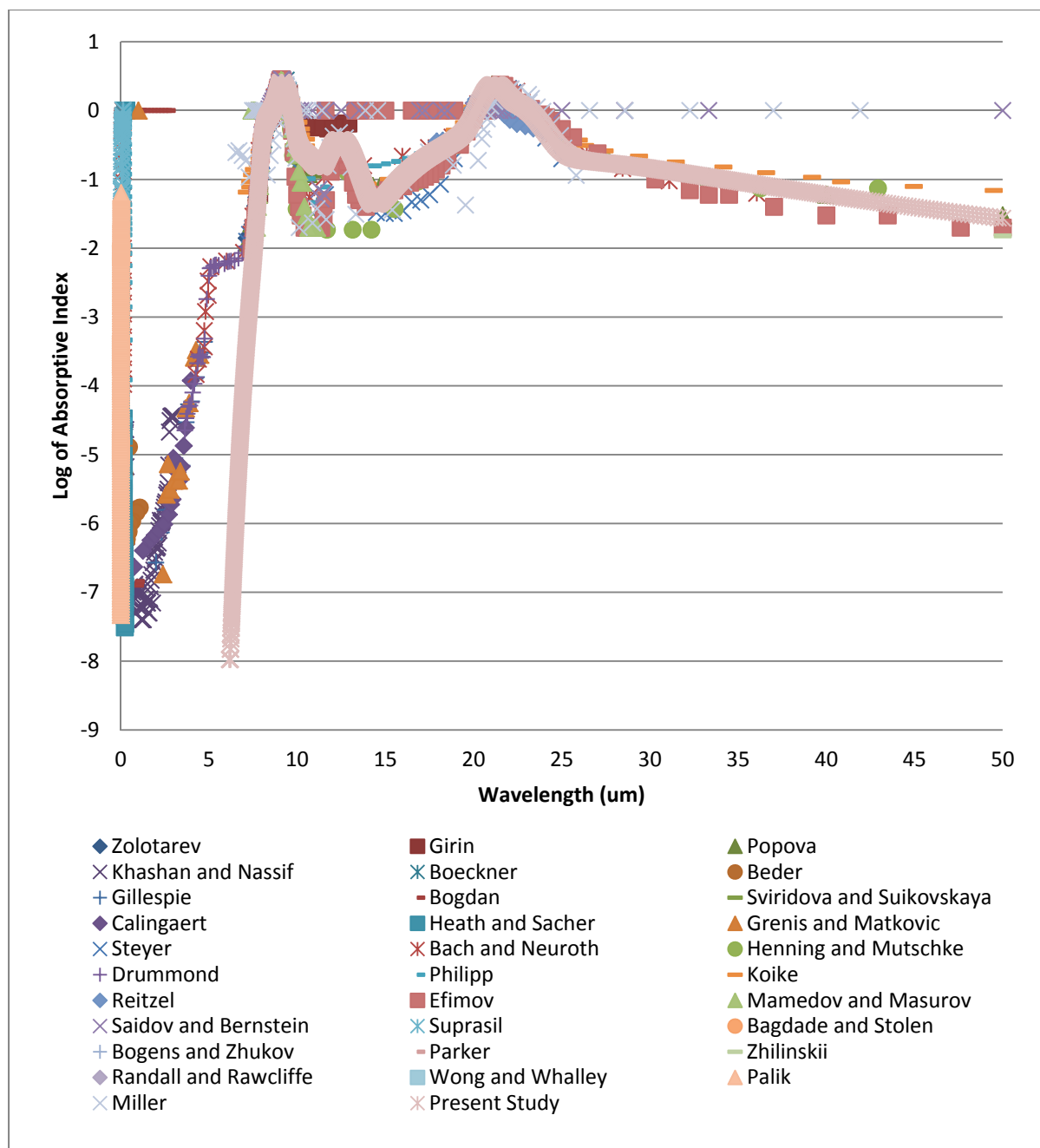


Figure 21. Log of absorptive index vs. wavelength using data from Pilon's research.

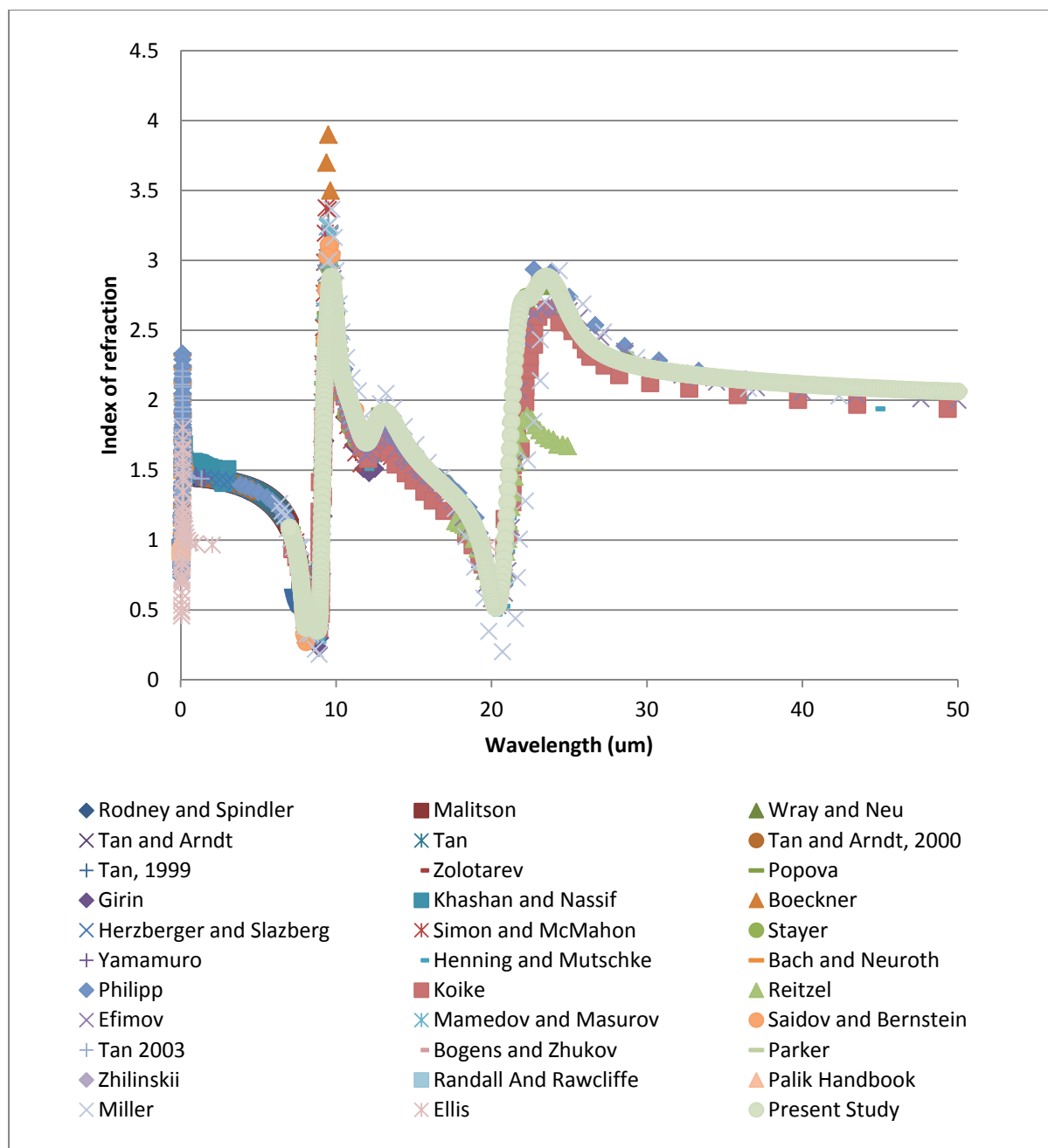


Figure 22. Index of refraction vs. wavelength using data from Pilon's research.

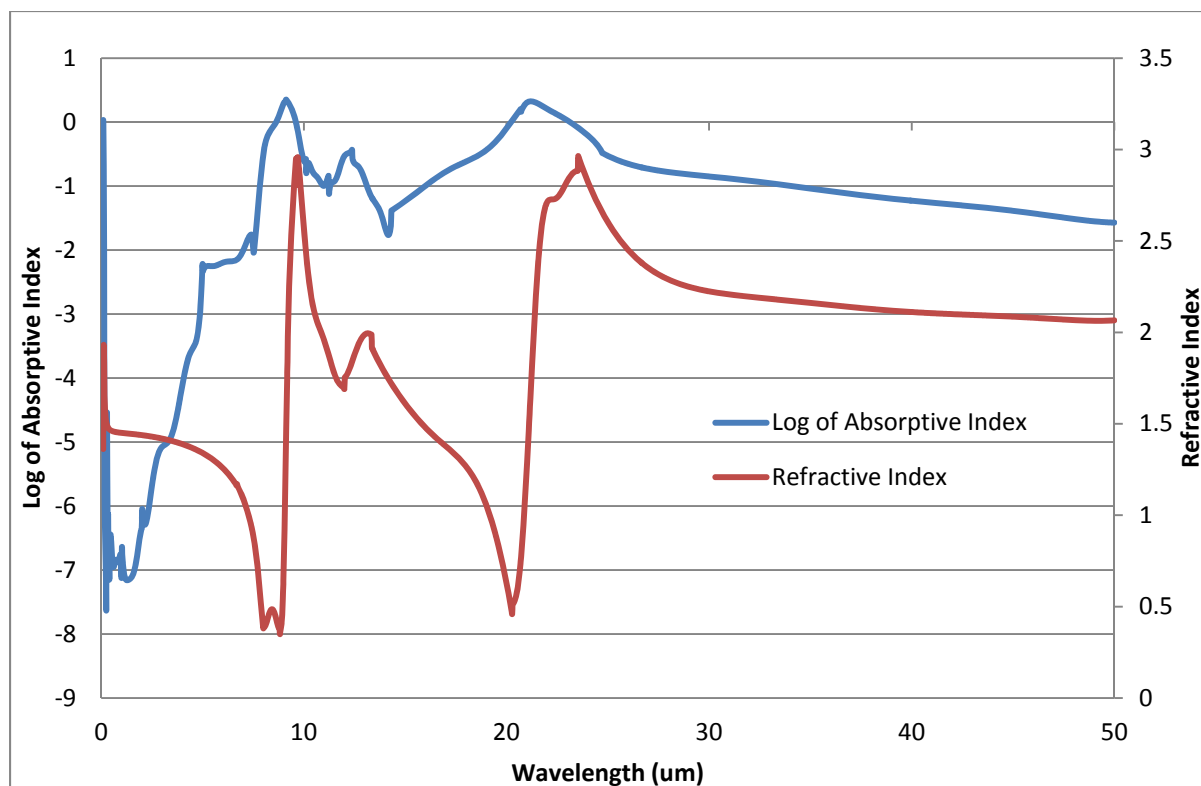


Figure 23. Refraction index and log of absorptive index using the fit equations for the data from Dr Pilon's research.

Considering these two facts, the polynomial fit equations are found, by dividing the wavelength into several intervals that are suitable for fit equations. These polynomial fit equations are then used to find the absorptive index and the index of refraction depending on the wavelength in the following calculations. The polynomial fit equations are added to the Appendix.

THE OPTICAL THICKNESS

The optical thickness is a dimensionless quantity, denoted as $\tau_{\lambda}(S)$. It is also called opacity along the path length S . The attenuation of the radiation at a given wavelength is simply indicated by the optical thickness. If the optical thickness is much bigger than 1, the medium is called optically thick which means that the radiation does not go through the medium instead it is absorbed by the medium. If the optical thickness is much smaller than 1, the medium is called optically thin which means that the radiation goes through the medium. As the optical thickness gets bigger, the medium will become opaque and in contrast to this, the medium will become less participating as the optical thickness gets smaller and eventually the medium will become perfectly transparent [35].

$$\tau_{\lambda} = \int_0^S \beta_{\lambda}(S^*) dS^* \quad (5)$$

Glass is a medium with spatially uniform properties, therefore Equation 5 becomes

$$\tau_{\lambda}(S) = \beta_{\lambda} S \quad (6)$$

$$\beta_{\lambda} = \kappa_{\lambda} + \sigma_{\lambda} \quad (7)$$

In Equations 5 and 6, S is the path length that the radiation travels and β_{λ} is extinction coefficient which represents the attenuation of the radiation that is traveling in the medium. The attenuation can be caused by absorption or scattering. In Equation 7, κ_{λ} is the absorption coefficient and σ_{λ} is the scattering coefficient. Since the glass does not scatter the radiation (assuming bubbles and other inclusions are negligible), Equation 6 becomes

$$\tau_{\lambda}(S) = \kappa_{\lambda} S \quad (8)$$

κ_{λ} , the absorption coefficient, is a function of the wavelength and the absorptive index [34]. It varies drastically with the wavelength. It also varies with the temperature and the pressure, though not as strongly. The data for κ_{λ} for a given wavelength is taken from the polynomial fit equations that are created from the data collected from Dr. Laurent Pilon's research as was mentioned earlier.

$$\kappa_{\lambda} = \frac{4\pi k_{\lambda}}{\lambda} \quad (9)$$

THE ABSORPTIVITY, REFLECTIVITY, AND TRANSMISSIVITY

Depending on the value of the optical thickness, two sets of formulas were used to determine the absorptivity, the reflectivity and the transmissivity. One is called the low opacity method and the other is called the high opacity method.

Low Opacity Method

Low opacity method is used when the absorptive coefficient is very small. When the absorptive coefficient is very small, the optical thickness will be small too. In this case, low opacity, the effect of absorptive index can be negligible from the complex refractive index. Therefore Equation 4 becomes

$$\bar{n}_{\lambda} = n_{\lambda} \quad (10)$$

The generalized Snell's law, which describes the relationship in between the angle of incident radiation and the angle of refraction, is given by Equation 11 [35]. Subscripts 1 and 2

represent different media. In our case, 1 is air and 2 is the glass. The index of refraction is 1 and the absorptive index is essentially 0 for the incident radiation in the air.

$$\frac{\sin \theta_1}{\sin \theta_2} = \frac{\bar{n}_1}{\bar{n}_2} = \frac{n_1 - ik_1}{n_2 - ik_2} \quad (11)$$

This relation cannot be interpreted physically since it is complex. But in the case of low opacity, the absorptive indices are negligible thus Equation 11 becomes

$$n_1 \sin \theta_1 = n_2 \sin \theta_2 \quad (12)$$

θ_1 is the angle of incoming radiation and θ_2 is the angle of refraction, shown in Figure 24.

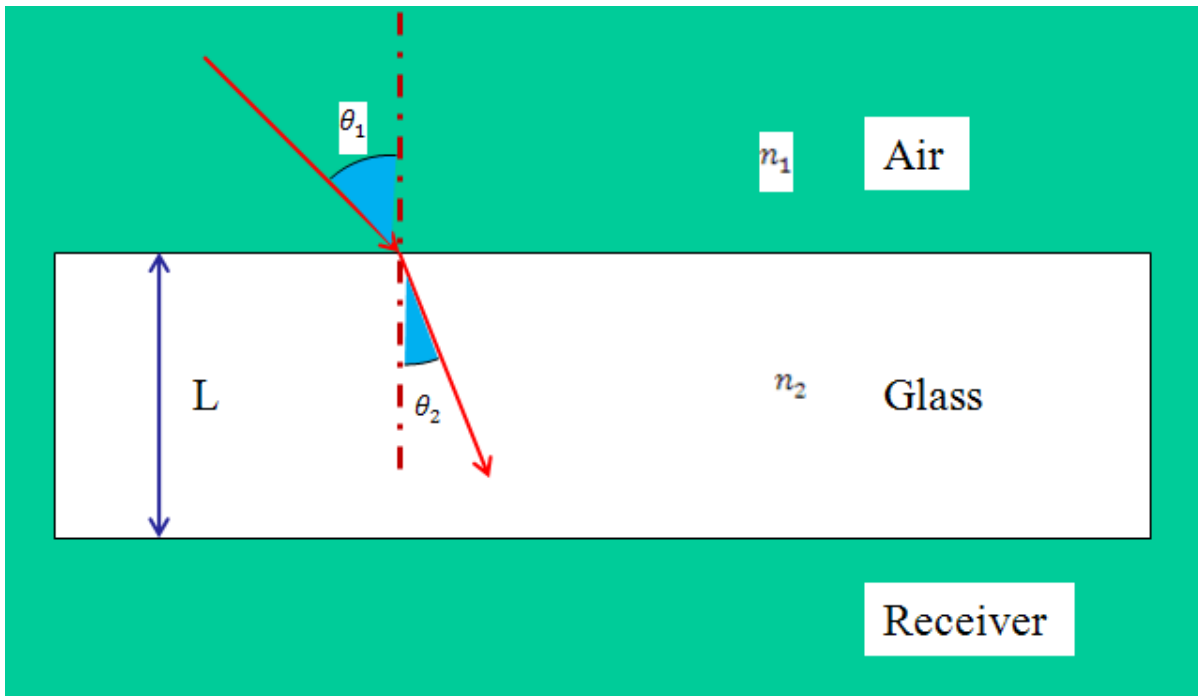


Figure 24. Angles of incoming radiation and refraction.

For smooth surfaces, the expressions for the reflection of unpolarized radiation on passing from medium 1 to medium 2, has derived by Fresnel, are given in Equation 13 to 15 [36]

$$r_{\perp} = \frac{\sin^2(\theta_2 - \theta_1)}{\sin^2(\theta_2 + \theta_1)} \quad (13)$$

$$r_{\parallel} = \frac{\tan^2(\theta_2 - \theta_1)}{\tan^2(\theta_2 + \theta_1)} \quad (14)$$

$$r = \frac{r_{\perp} + r_{\parallel}}{2} \quad (15)$$

Where, r_{\perp} represents the perpendicular component of unpolarized radiation, and r_{\parallel} represents the parallel component of unpolarized radiation. The average of these two components is given in

Equation 15 as r . For the radiation that hits the interface at normal incidence, both incident angle and the refraction angle are zero. Thus, Equation 15 becomes [36].

$$r(0) = \left(\frac{n_1 - n_2}{n_1 + n_2} \right)^2 \quad (16)$$

There are two interfaces at the window. The systems which have two interfaces are called cover system [36]. If the incoming radiation that travels through the window does not get absorbed by the window then it will hit both of the interfaces as it is shown at Figure 25. Therefore the reflection losses from the second interface need be counted for as well as absorption losses.

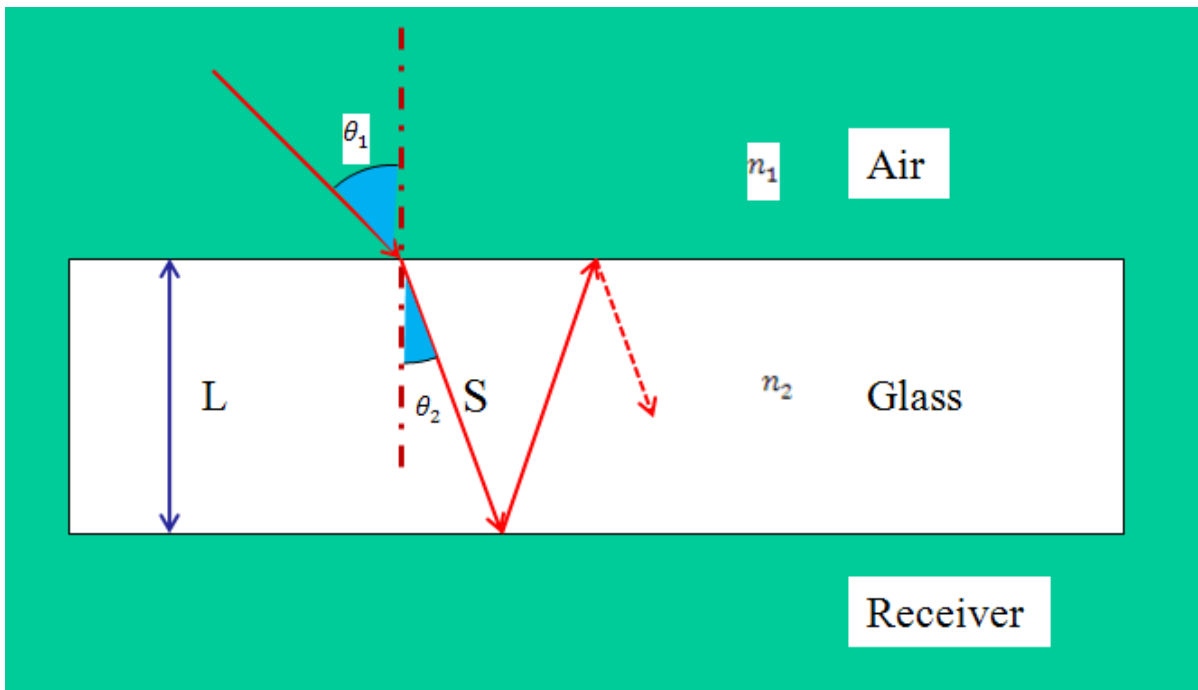


Figure 25. Reflection from the second interface.

The perpendicular component of the transmittance, the reflectance, and the absorptance of a single cover, which is one of the faces of the window in this case, can be obtained either by the net radiation method or by ray tracing methods. The perpendicular component of the transmittance, the reflectance, and the absorptance of a single cover are shown in Equation 17 to 19. Similar results are found for the parallel component of polarization [36].

$$\tau_{\perp} = \frac{\tau_a(1-r_{\perp})^2}{1-(r_{\perp}\tau_a)} = \tau_a \frac{1-r_{\perp}}{1+r_{\perp}} \left[\frac{1-r_{\perp}^2}{1-(r_{\perp}\tau_a)^2} \right] \quad (17)$$

$$\rho_{\perp} = r_{\perp}(1 + \tau_a\tau_{\perp}) \quad (18)$$

$$\alpha_{\perp} = (1 - \tau_a) \left(\frac{1 - r_{\perp}}{1 - r_{\perp} \tau_a} \right) \quad (19)$$

Bouguer's law describes the absorption of incoming radiation in a partially transparent medium such as glass. It is assumed that the absorbed radiation and the local intensity in the medium are proportional to each other. It is given in Equation 20.

$$dI = -I\beta_{\lambda} dx \quad (20)$$

β_{λ} is the extinction coefficient which is absorption coefficient (κ_{λ}) plus scattering (σ_{λ}). It is assumed that there is no scattering in the window. Therefore, β_{λ} is equal to κ_{λ} . x is the path length that radiation travelled in the medium. Integrating Equation 20 in the medium along the path length of S lead us to

$$\tau_a = \frac{I_{transmitted}}{I_{incident}} = \exp(-\kappa_{\lambda}S) \quad (21)$$

$$S = \frac{L}{\cos \theta_2} \quad (22)$$

Where τ_a represents the transmission (only absorption losses considered) and κ_{λ} is absorption coefficient as it was mentioned before. L is the thickness of the glass which changes from 1 cm to 4 cm depending on the study but 2.5 cm is the base case. θ_2 is the refraction angle [36]. The path length S is different for each ray depending on the incident angle, refractive indices of the two media, and the thickness of the glass. The absorption loss will increase as S increases. S is also shown earlier in Figure 25.

Finally the transmissivity, absorptivity and reflectivity for the low opacity case are found by averaging the parallel and the perpendicular components of polarization. They are given in Equation 23 to 25. Since these optical properties are the percentage, they should add up to one [36].

$$\tau = \frac{\tau_{\perp} + \tau_{\parallel}}{2} \quad (23)$$

$$\rho = \frac{\rho_{\perp} + \rho_{\parallel}}{2} \quad (24)$$

$$\alpha = \frac{\alpha_{\perp} + \alpha_{\parallel}}{2} \quad (25)$$

$$\alpha + \rho + \tau = 1 \quad (26)$$

High Opacity Method

In the case of high opacity, which means the optical thickness is much bigger than 1, the absorptive index is high enough that cannot be negligible in developing the interface

reflectivities. Therefore, the simple Snell's law cannot be used since the complex part of the relation depends on the absorptive index. Accordingly, the refraction angle cannot be found. The formulas that are given before in order to calculate the optical properties of the glass have the dependency of the refraction angle. Therefore they cannot be used. However, the glass can be treated as an opaque absorbing medium. The reason is that in this case, there will be no transmission since the medium is optically thick. The radiation then can be only either reflected or absorbed. The parallel and perpendicular components of the reflectivity are given in Equation 27 and 28 for an absorbing medium that is exposed to the radiation coming from air [35].

$$\rho_{\parallel}(\theta_1) = \frac{(n_2\gamma - \alpha/\cos\theta_1)^2 + (n_2^2 + k^2)\alpha - n_2^2\gamma^2}{(n_2\gamma + \alpha/\cos\theta_1)^2 + (n_2^2 + k^2)\alpha - n_2^2\gamma^2} \quad (27)$$

$$\rho_{\perp}(\theta_1) = \frac{(n_2\beta - \cos\theta_1)^2 + (n_2^2 + k^2)\alpha - n_2^2\beta^2}{(n_2\beta + \cos\theta_1)^2 + (n_2^2 + k^2)\alpha - n_2^2\beta^2} \quad (28)$$

Where

$$\alpha^2 = \left(1 + \frac{\sin^2\theta_1}{n_2^2 + k^2}\right)^2 - \frac{4n^2}{n_2^2 + k^2} \left(\frac{\sin^2\theta_1}{n_2^2 + k^2}\right) \quad (29)$$

$$\beta^2 = \frac{n_2^2 + k^2}{2n_2^2} \left(\frac{n_2^2 - k^2}{n_2^2 + k^2} - \frac{\sin^2\theta_1}{n_2^2 + k^2} + \alpha\right) \quad (30)$$

$$\gamma = \frac{n_2^2 - k^2}{n_2^2 + k^2} \beta + \frac{2n_2k}{n_2^2 + k^2} \left(\frac{n_2^2 + k^2}{n_2^2} \alpha - \beta^2\right)^{1/2} \quad (31)$$

As it is seen in the equations, there is no refraction angle dependency. The reflectivity is a function of the index of refraction, the absorptive index and the incident angle. There is an alternative form for calculating the reflectivity which is used to compare it to this form [35]. It is given in the following equations. Comparison showed that both methods give the same results.

$$\rho_{\parallel}(\theta_1) = \frac{a^2 + b^2 - 2a \sin\theta_1 \tan\theta_1 + \sin^2\theta_1 \tan^2\theta_1}{a^2 + b^2 + 2a \sin\theta_1 \tan\theta_1 + \sin^2\theta_1 \tan^2\theta_1} * \rho_{\perp}(\theta_1) \quad (32)$$

$$\rho_{\perp}(\theta_1) = \frac{a^2 + b^2 - 2a \cos\theta_1 + \cos^2\theta_1}{a^2 + b^2 + 2a \cos\theta_1 + \cos^2\theta_1} \quad (33)$$

Where

$$a^2 = \frac{1}{2} \{[(n_2^2 + k^2 - \sin^2\theta_1)^2 + 4n_2^2k^2]^{0.5} + n_2^2 - k^2 - \sin^2\theta_1\} \quad (34)$$

$$b^2 = \frac{1}{2} \{[(n_2^2 + k^2 - \sin^2\theta_1)^2 + 4n_2^2k^2]^{0.5} - (n_2^2 - k^2 - \sin^2\theta_1)\} \quad (35)$$

The reflectivity for the high opacity case is found by averaging the parallel and the perpendicular components. The absorptivity will be 1 minus the reflectivity since the transmissivity is 0 in this case.

$$\rho = \frac{\rho_{\perp} + \rho_{\parallel}}{2} \quad (36)$$

$$\alpha = 1 - \rho \quad (37)$$

$$\tau = 0 \quad (38)$$

For the radiation that hits the interface at normal incidence, the reflectivity is given in Equation 39 [35].

$$\rho_{\lambda,n}(\theta_1) = \frac{(n_2 - n_1)^2 + (k_2 - k_1)^2}{(n_2 + n_1)^2 + (k_2 + k_1)^2} \quad (39)$$

RESULTS FOR THE OPTICAL PROPERTIES

The program called `optical_properties_TD` has been written using Fortran by the author in order to calculate the optical properties of the glass window, which are the transmissivity, absorbtivity and reflectivity. The wavelength range that is used for the calculation purposes is in between 0.1 μm to 50 μm . This wavelength range is chosen in order to match the developed code to the previous code that was created by Ruther for the receiver. In his work, it was explained that the upper wavelength cutoff can be chosen so that the excluded black body fraction is negligible. The approximate wall temperature of the small particle solar receiver is 1000 K. The chosen upper wavelength cutoff is 50 μm . The reason to choose this number is that only 0.11 % of the black body fraction is excluded. This is a very small portion and is negligible [21].

It was mentioned earlier in Chapter 3.2 that the optical thickness is a dimensionless number that defines the opacity of the material. If the optical thickness is much bigger than 1 then the medium is optically thick. This cutoff number is very important to find since there are two different approaches to the calculation depending on this number. The effect of the cutoff number on the optical properties was studied to pick the right cutoff number. The cutoff number was varied from 1 to 15. The incident angle of the incoming radiation and the thickness of the glass are the two important variables that have a tremendous effect on the optical properties such as the absorptivity, the reflectivity, and the transmissivity. Therefore, various incident angles and two different thicknesses for the glass were also studied. The incident angle was varied from 0 degree to 75 degree.

The results of the studies showed that the effect of the cutoff number for the optical thickness is significant in the wavelength interval of approximately 3 μm to 5 μm , depending on the other parameters mentioned earlier. In this wavelength interval, the transition of the glass from being transparent to being opaque can be seen. Two figures are displayed to show the effect

of the cutoff number on the absorptivity. Similar results are observed for the transmissivity and the reflectivity. The displayed figures are only for one specific incident angle because changes in incident angle will of course change the values of optical properties but the effect of the cutoff number is same for different incident angle. Therefore, similar results are also observed with various angles for the transmissivity and the reflectivity.

The significant effect of the cutoff number on the optical properties can be easily seen on Figure 26 and Figure 27. Figure 26 is for 1 cm thick window with 0 degree incident angle. Figure 27 is for 2.5 cm thick window with 0 degree angle. There is very unrealistic jump from absorptivity of approximately 0.6 to 0.98 in both figures. The area between the red line and the blue line in each figure is the extra absorption that is considered when the cutoff number is chosen 1. Extra absorption will show a temperature increase in window temperature when that is eventually calculated. The yellow line in the figures cannot even be seen because 10 and 15 leads the same results. The lines are very smooth and realistic. Therefore, either 10 or 15 can be chosen for the cutoff number. For the calculations, 10 will be used. It should be pointed out that the same cut-off number found regardless of the thickness because the window thickness does not affect the critical opacity. But it affects the value of the optical properties.

Now that the cutoff number is chosen, further calculations can be performed to find the optical properties. The results for the optical properties will be displayed for 1 cm and 2.5 cm thick windows. The incident angle of the incoming ray has a significant effect on the results, therefore, will be defined for each figure. The full wavelength range for this research (0.1 μm to 50 μm) will be studied as well as solar spectrum.

It was mentioned before that quartz is a selective material which has a high transmissivity in the solar spectrum. Figure 28 supports this statement. The transmissivity of the quartz window is over 90% in the solar spectrum. Approximately 3% of absorption and 6% of reflection is also observed in the solar spectrum. The transmissivity drops to 0 percent around 4 μm . In the longer wavelengths, high absorptivity, lower reflectivity, and no transmissivity are encountered.

The effect of incident angle on the optical properties cannot be easily seen in Figure 29 despite the change in incident angle. The change in the optical properties is more obvious as the incident angle increases. This change can be seen in Figure 30 when the incident angle is 60 degree. It was observed that the transmissivity of the window decreases while the reflectivity

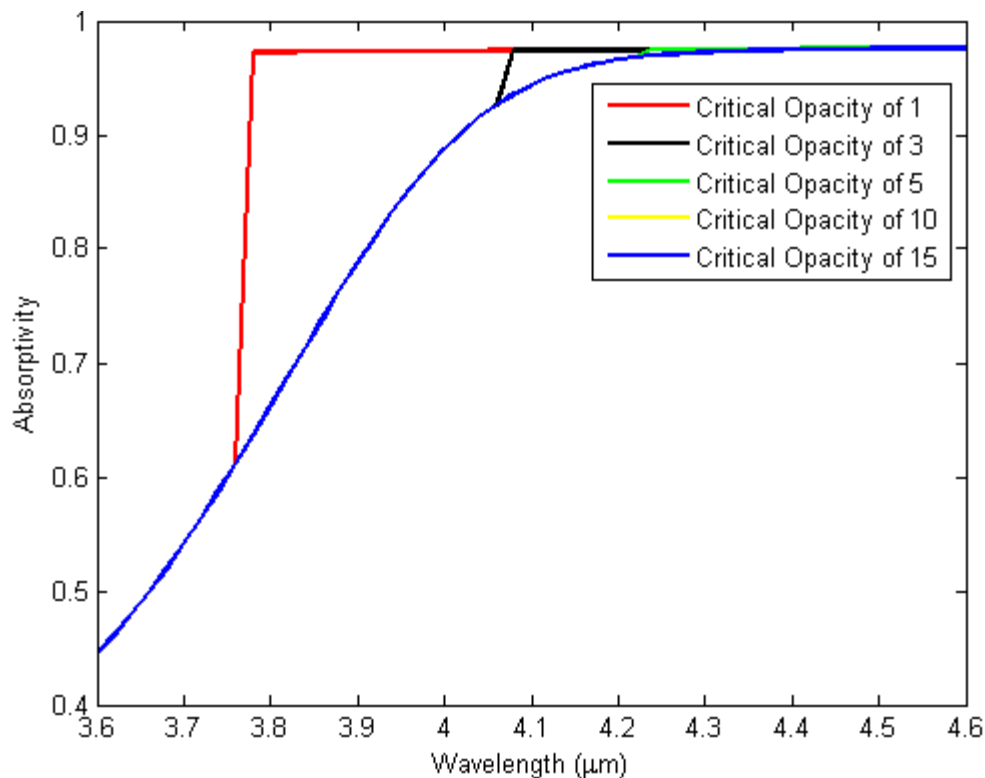


Figure 26. The effect of the cutoff number on absorptivity for 1 cm thick window with 0 degree incident angle.

increases. The absorptivity behaves differently depending on the wavelength of the incoming ray because the change in the extinction coefficient is very rapid depending on the wavelength.

Optical properties were plotted with respect to the incident angle for a chosen wavelength in order to have a better understanding of the affect of the incident angle on the optical properties. The thickness of the window was kept the same as 1 cm while two different wavelengths were studied. The peak of solar spectrum is $0.5 \mu\text{m}$ and the maximum spectral blackbody emissive power from the receiver is reached at approximately $3 \mu\text{m}$. Therefore, these two wavelengths were chosen for the study.

The results show that the affect of the incident angle on the optical properties is more obvious after 40 degree incident angle. The transmissivity decreases, the reflectivity increases, and the absorptivity first increases then decreases, shown in Figure 31 and Figure 32. These patterns always occur despite the wavelength of the incoming radiation, although the magnitude can vary.

The drastic change after 60 degree incident angle on the optical properties brings the worry of having low transmissivity thus transmission. For this reason, the frequency of incident

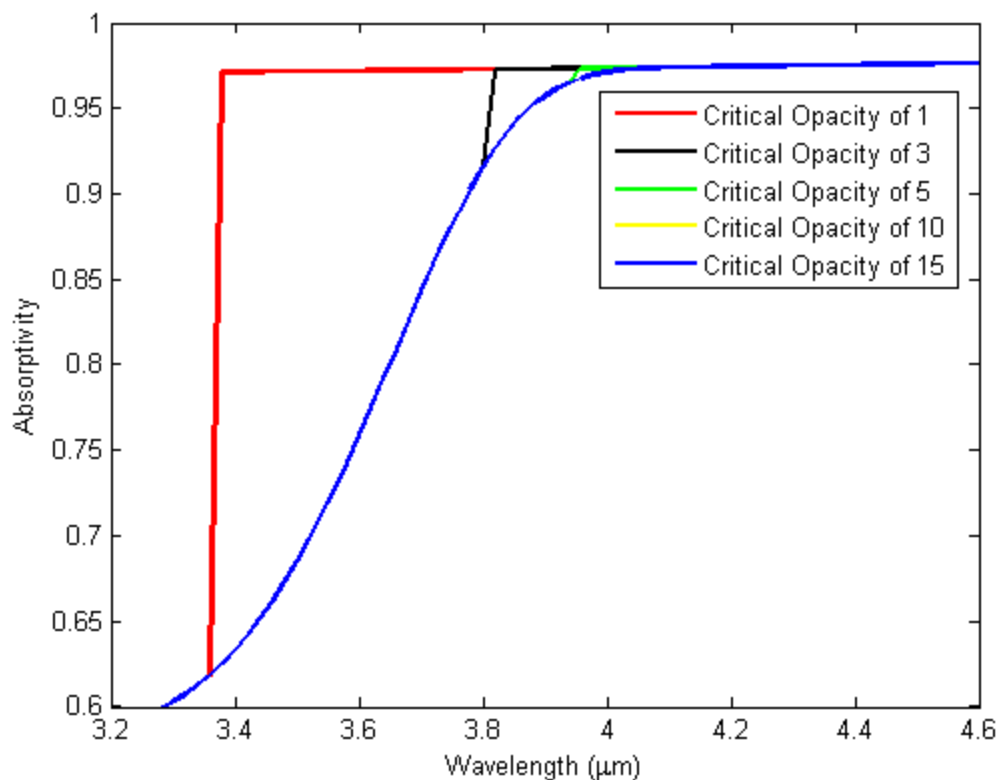


Figure 27. The effect of the cutoff number on absorptivity for 2.5 cm thick window with 0 degree incident angle.

angle of the incoming rays reaching the aperture plane should be determined when the window is flat. This study will be performed again with changing geometry of the window. It was performed now to see the affect if we had a window at the aperture plane. Frequency is reached by dividing the number of the rays for a specific angle by the total number of rays. It is plotted against the incident angle, Figure 33. It is found that zero percentage of the rays has 60 degree and higher incident angle while the highest incident angle is 57.

The results shown in this chapter so far, except one of the critical opacity graph, are for 1 cm thick window although our window will likely be 2.5 cm based on recent structural calculation and suggestions from the vendor. The reason for that the studies on the windows are generally done for 1 cm thick windows in the literature. It would make it easier to compare the results. Now, some of the results will be repeated for 2.5 cm thick window.

Comparing Figure 34 (2.5 cm thick window) with Figure 28, it is observed that there is not an obvious difference between figures. Looking more closely to the figures, the slight difference appears in the solar spectrum. Figure 35 show the optical properties in the solar

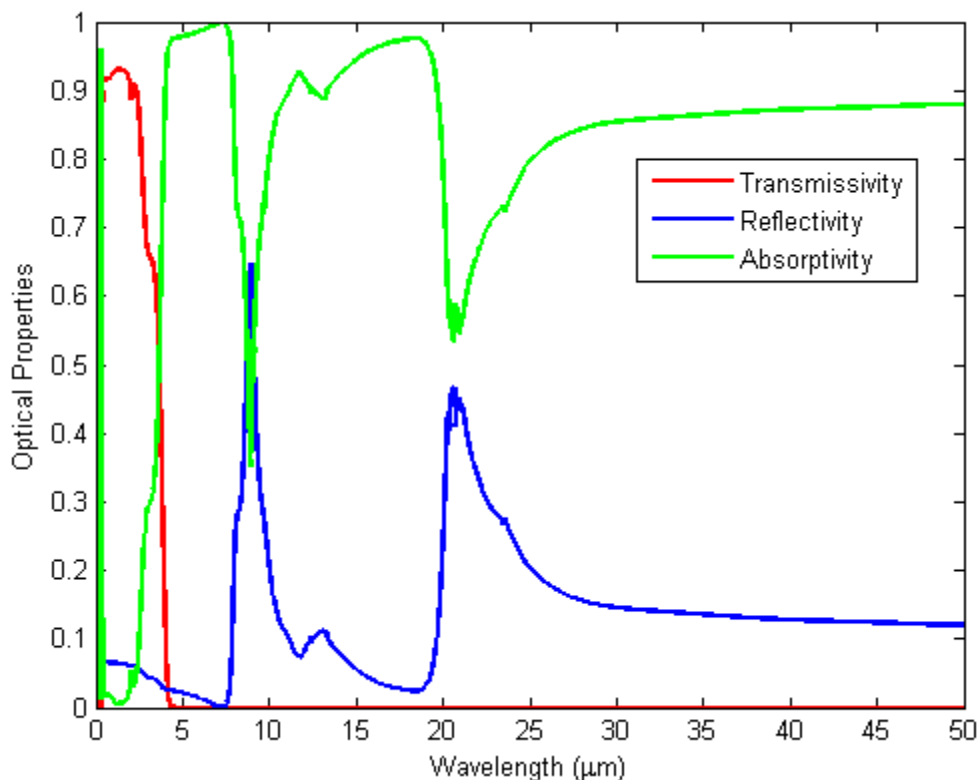


Figure 28. Optical properties of the window (1 cm thick, 0 degree incident angle).

spectrum. Results shows that the transmissivity is slightly lower compare to the 1 cm thick window.

Figure 36 shows the incident angle has the same affect on the optical properties despite the change in thickness of the window. Meaning, as the incident angle increases, transmissivity decreases, and the reflectivity increases. It should be noted that the change in thickness will change the values of the optical properties for a specific wavelength and an incident angle. As seen in the Figure 36, the transmissivity is slightly lower and the reflectivity is slightly higher compare to Figure 31.

The changes are more drastic for 3 μm, Figure 37. The absorptivity is much higher and the transmissivity is much lower compare to Figure 32. The reason is the absorptive index of the material is much higher at the wavelength of 3 μm. Since the transmissivity and the reflectivity are highly depended on the absorptive index, even a small change in the absorptive index will have a strong affect on these optical properties. On the other hand the reflectivity does not change at all. The reason is that the reflectivity is not a function of absorptive index but index of refraction.

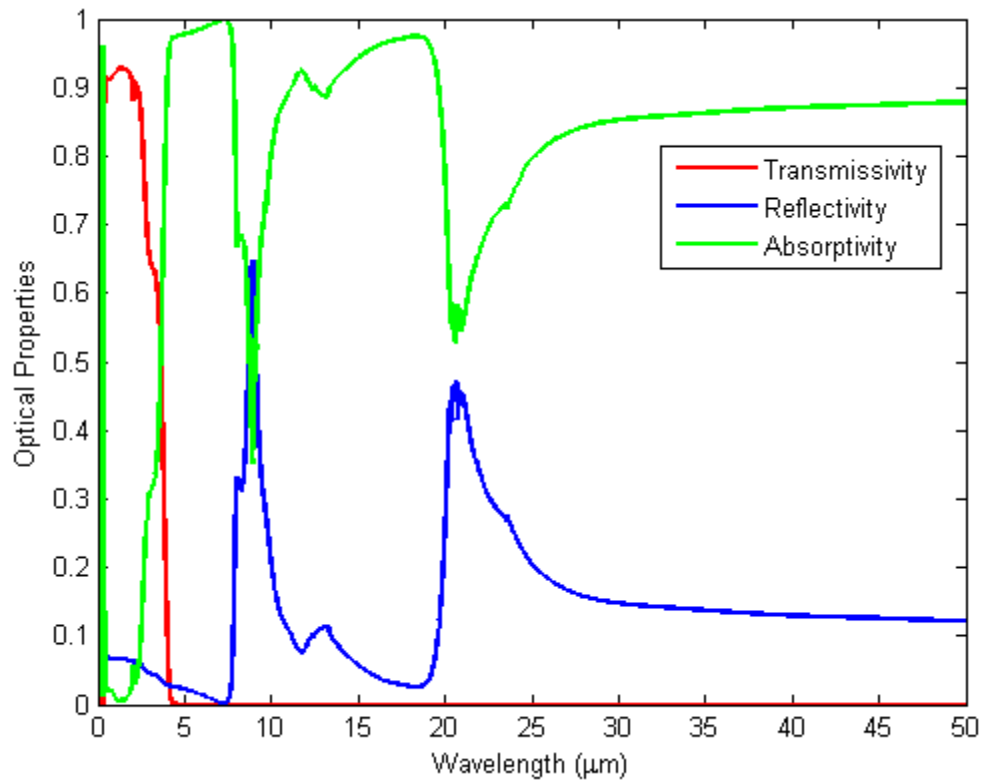


Figure 29. Optical properties of the window (1 cm thick, 30 degree incident angle).

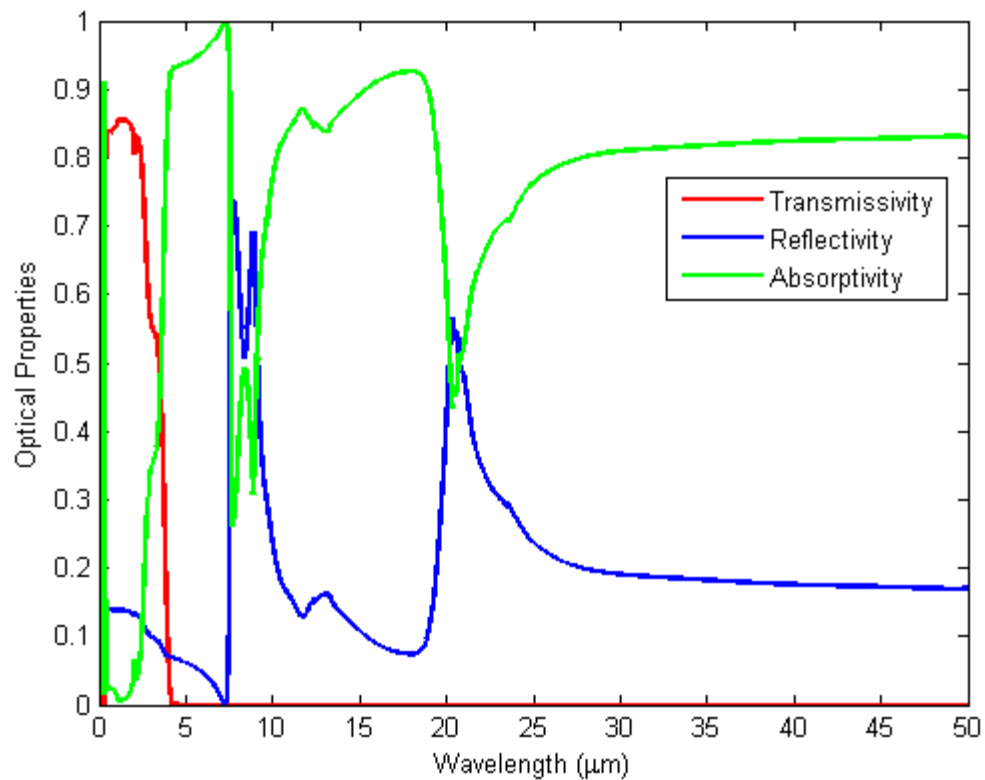


Figure 30. Optical properties of the window (1 cm thick, 60 degree incident angle).

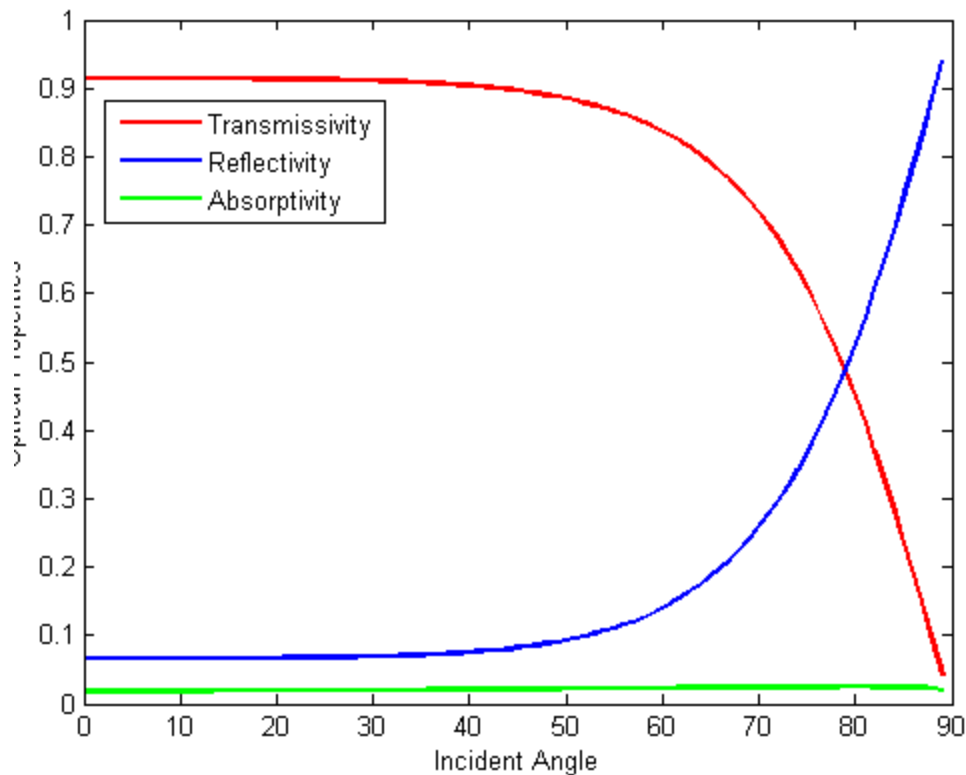


Figure 31. Optical properties of the window (1 cm thick, $0.5 \mu\text{m}$).

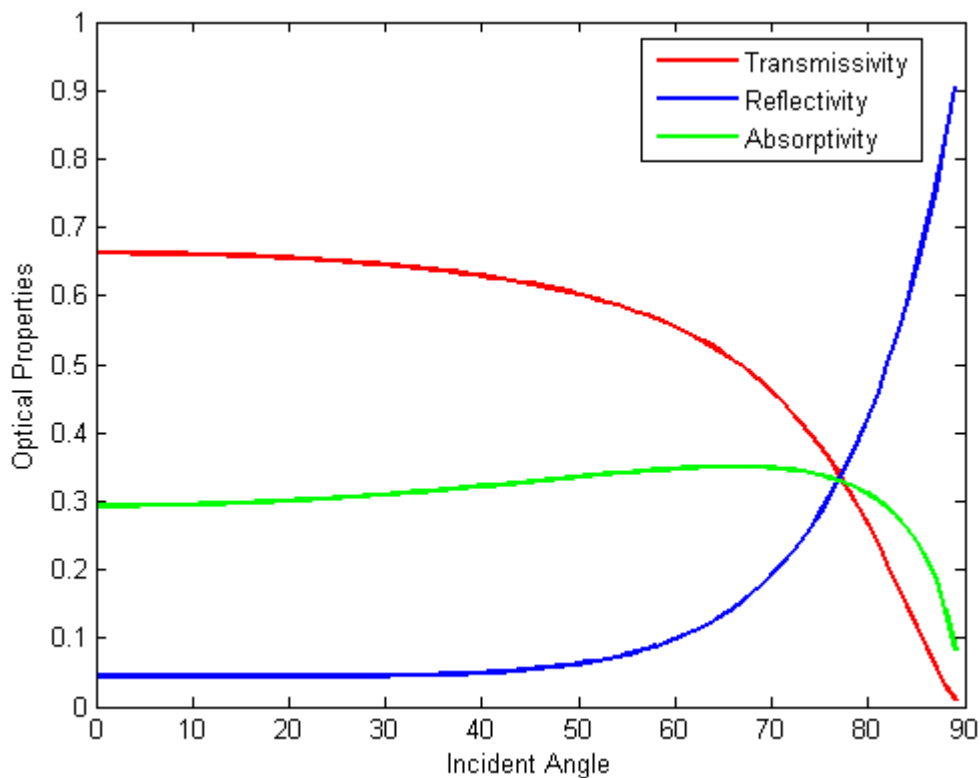


Figure 32. Optical properties of the window (1 cm thick, $3 \mu\text{m}$).

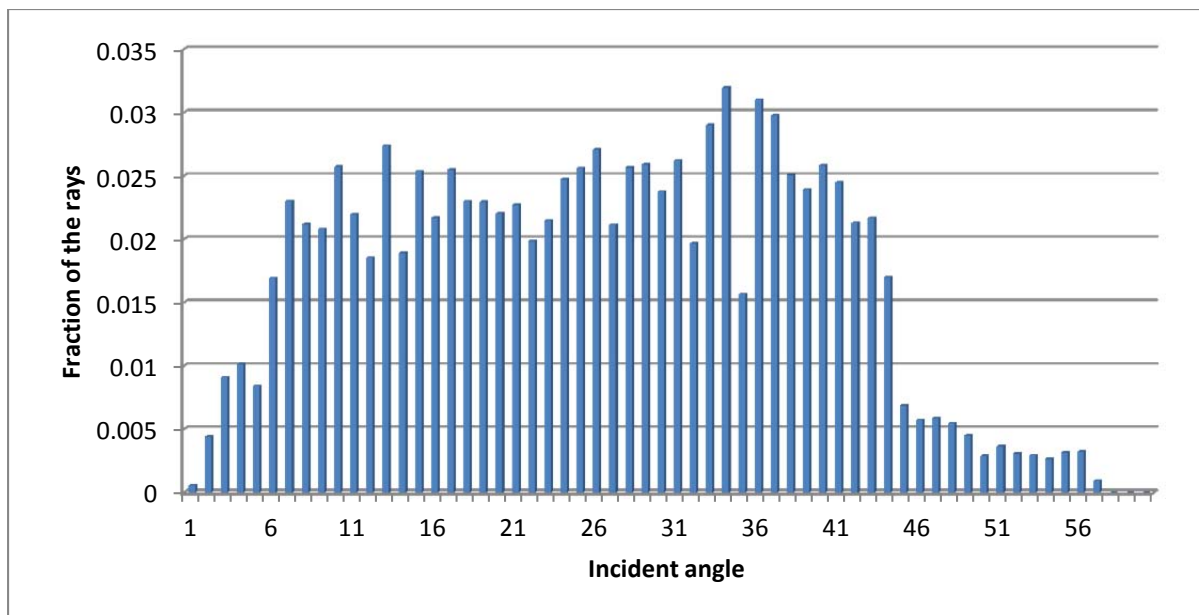


Figure 33. Frequency of the incident angle of the incoming rays to the aperture plane on March 21th at 12 pm (16 million rays).

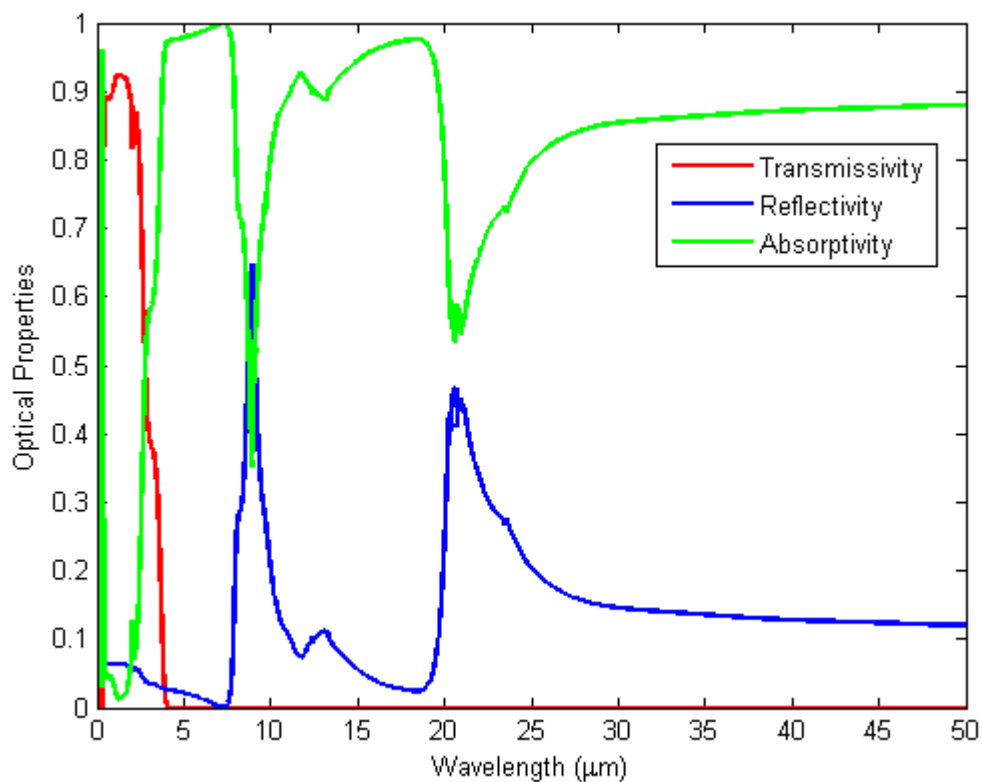


Figure 34. Optical properties of the window (2.5 cm thick, 0 degree incident angle).

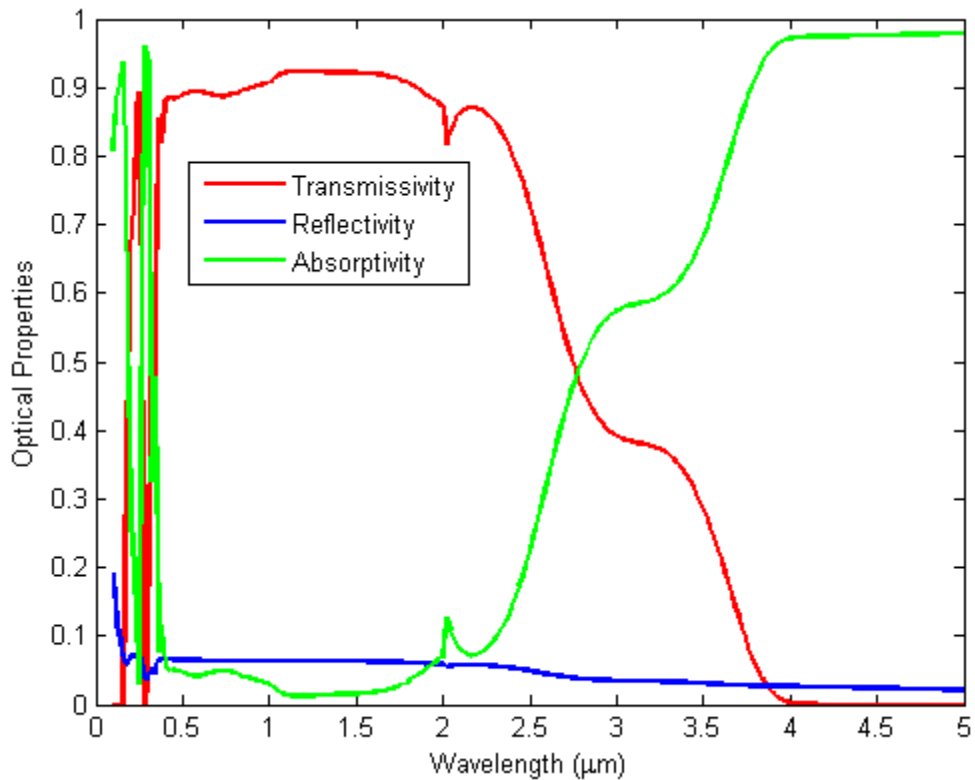


Figure 35. Optical properties of the window in the solar spectrum (2.5 cm thick, 0 degree incident angle).

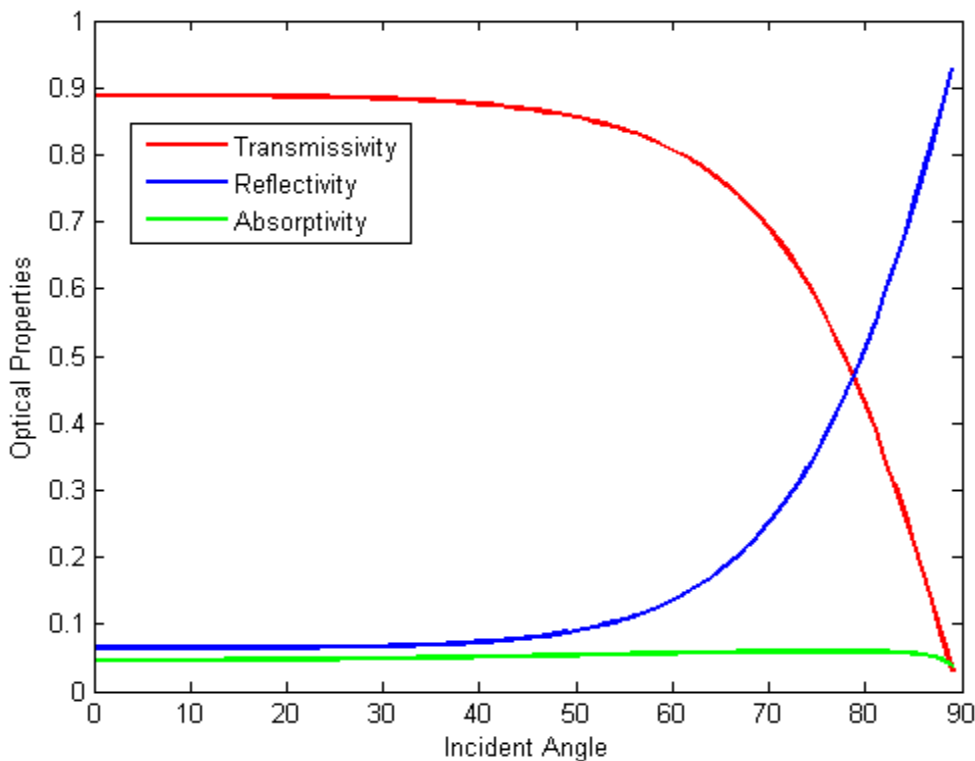


Figure 36. Optical properties of the window (2.5 cm thick, 0.5 μm).

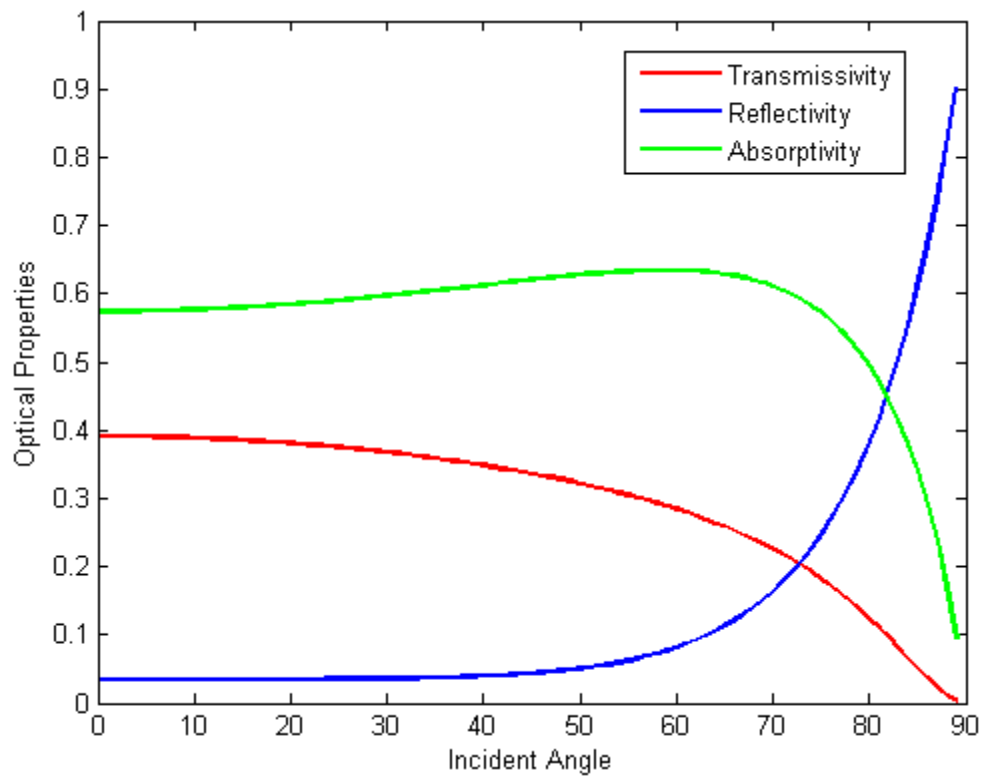


Figure 37. Optical properties of the window (2.5 cm thick, 3 μ m).

CHAPTER 4

WINDOW MATERIAL

Once again, quartz was chosen as the window material because it is that quartz is a selective material with high transmissivity in the solar spectrum and low transmissivity in the infrared region. High transmissivity means that more solar radiation coming from the heliostat field will be let into the solar receiver. There are many types and grades of quartz depending on source and manufacturing method. Earlier in Chapter 3, the results for optical properties shown are for generic fused quartz. The absorptive index and the index of refraction are excerpted from Dr. Pilon's research [34]. Dr. Pilon collected the data from many other researchers. Continuing the calculations with these data, the results showed higher absorptivity and somewhat lower transmissivity in the solar spectrum compared to different materials from the vendor, Heraeus, these comparisons will be explained in detail in this chapter. The lower the absorptivity and the higher the transmissivity, the better it is for our application. The main purpose is to get as much as radiation into the receiver while absorbing the least amount of radiation by the window since absorbed radiation might heat the window up over the operating temperature. Therefore, the optical properties should be investigated closely. Figure 38 shows the optical properties calculated using the data for refractive index and absorptive index for generic fused quartz from Dr. Pilon's research [34] over the solar spectrum for 1 cm thick window with 0 degree incident angle.

Looking deep into Dr. Pilon's paper and looking at his references, it is concluded that the papers do not show enough information about the quartz (in many cases), such as metal impurity, OH- content, source of material, etc. Therefore, the quality of the quartz is unknown. More data are needed to compare the results in order to choose the right material. Since the window will actually be built soon, we contacted our window vendor L-3 Brashear to obtain more realistic data, which they in turn obtained from Heraeus, a quartz supplier. A few data for the optical properties at different wavelengths were provided for comparison.

Figure 39 shows the transmission for three different grades of fused quartz from Heraeus [37] with the transmission from my studies (legend: SDSU). My studies are done with 0 degree incident angle for 1 and 2.5 cm windows. The data from Heraeus is simply obtained by digitizing

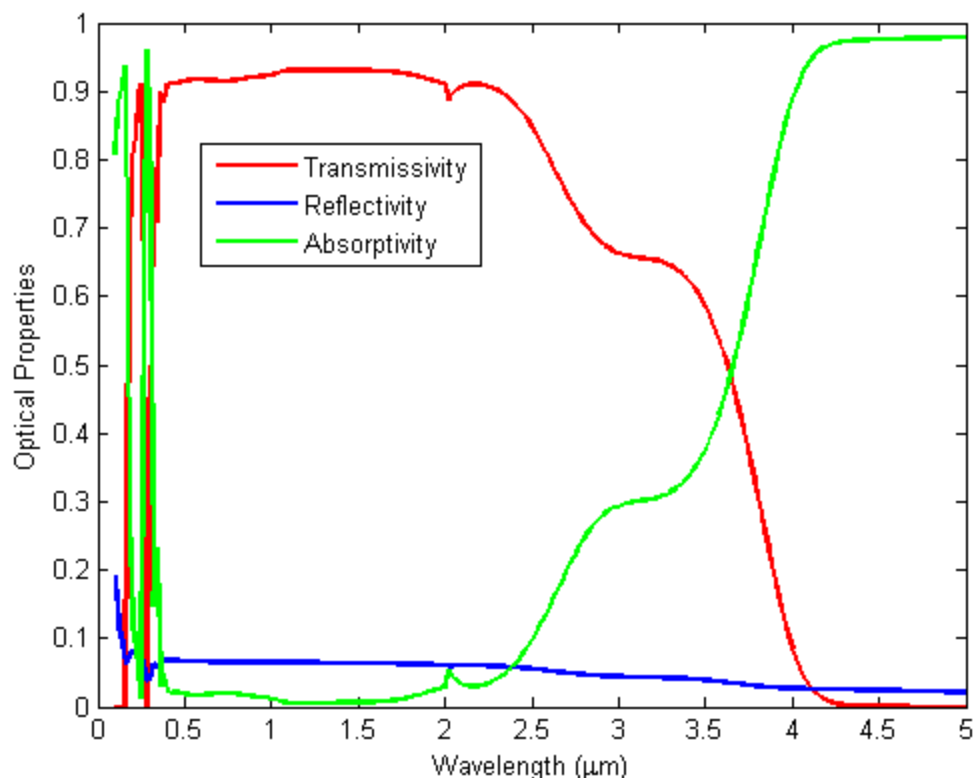


Figure 38. Optical properties of the window in the solar spectrum (1 cm thick, 0 degree incident angle).

the data (figures) in their literature by using a commercial program called Plot Digitizer. The number of data points is chosen appropriately depending on the curve of different grades. By looking at the figure without considering the cost and the production, Surprasil 3001 and HSQ 300 seems like a good option with its high transmissivity in the solar spectrum. On the other hand, HOQ 310 is a cheaper material but the transmissivity of HOQ 310 is lower compared to Surprasil 3001 and HSQ 310.

The absorptive index for Surprasil 3001 and 311 were provided by Heraeus [37]. Further calculations were performed to calculate the absorptivity for both 1 and 2.5 cm thick windows. Figure 40 shows the comparison of these absorptivities with my studies. The data for absorptive index in the wavelength range of 0.9 μm to 1.5 μm was taken from [38]. It is seen in the Figure 40, the absorptivity of Surprasil 3001 is very low compare to the others for given wavelengths.

The absorptivity will get higher as the value of the absorptive index gets higher. There are some other data for the absorptive index that were provided by Heraeus. Figure 41 was created to see the differences in the extinction coefficients for different types of quartz from Heraeus and Dr. Pilon's paper [34, 37]. Dr. Pilon collected the data from [38-40] for the

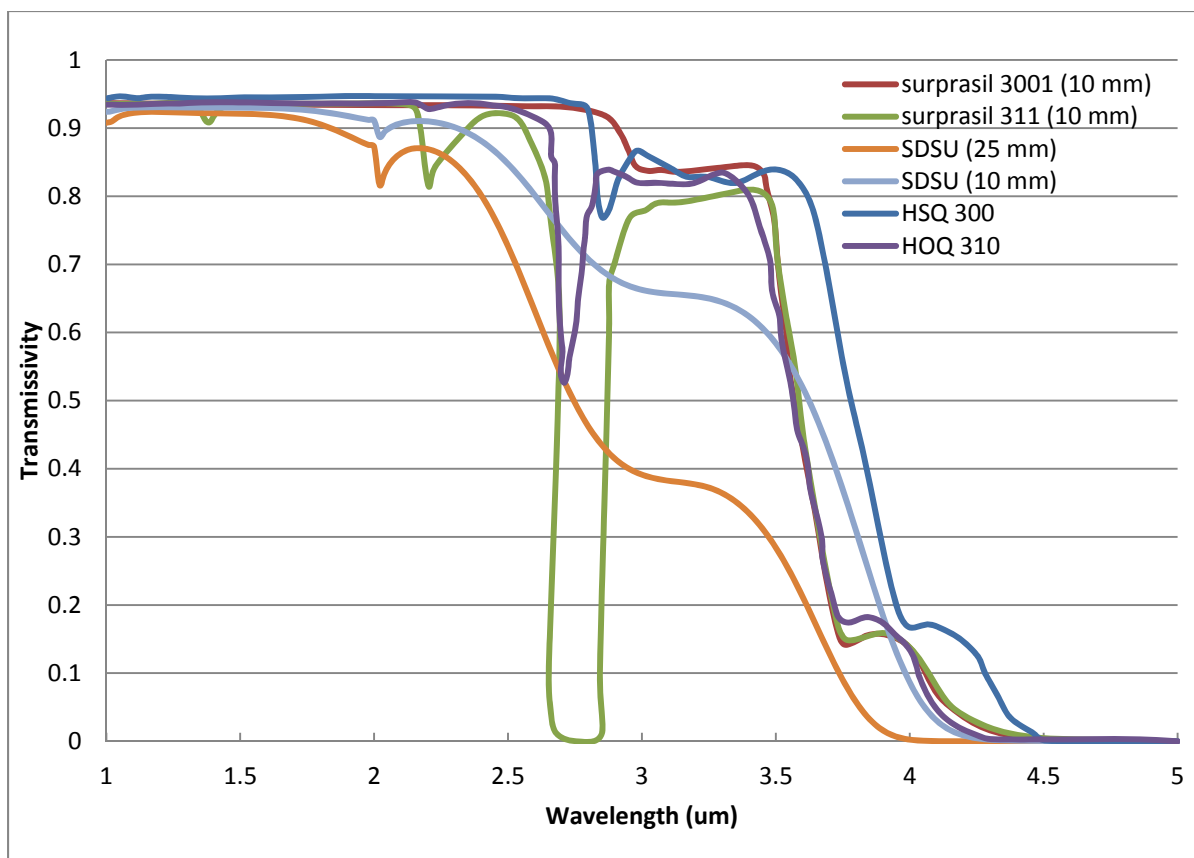


Figure 39. Comparison of spectral transmissivities for 0 degree incident angle.

wavelength range of 0.9 μm to 1.4 μm . These data are for the fused quartz but the quality of the material is unknown due to lack of information regarding the source in the original papers. Comparing these data to the data from Heraeus showed that the data from Khassan and Nassif is closer to the Heraeus data but the difference is still very big. Every data from Dr. Pilon's paper were being considered before comparing to the Heraeus data; SDSU old fit equation in Figure 41. After the comparison, only the data from Khassan and Nassif were used in the calculations, for given wavelength range; SDSU fit equation in Figure 41. The comparison can be seen in Figure 41. On the other hand, it is obvious that the Surprasil 3001/3002/302 is a better material for our window just by looking at this wavelength range. More data is needed for this material in the solar spectrum in order to modify the data for absorptive index for more realistic results. Currently, we are in touch with the vendor to get the data we need.

The reason why we have limited spectral data from Heraeus is that they are only interested in certain wavelengths. Their wavelengths of interests are 946nm, 1040nm, 1064nm, 1080nm, and 1319nm. 946nm is typical Laser Diode wavelength, used for pumping and material

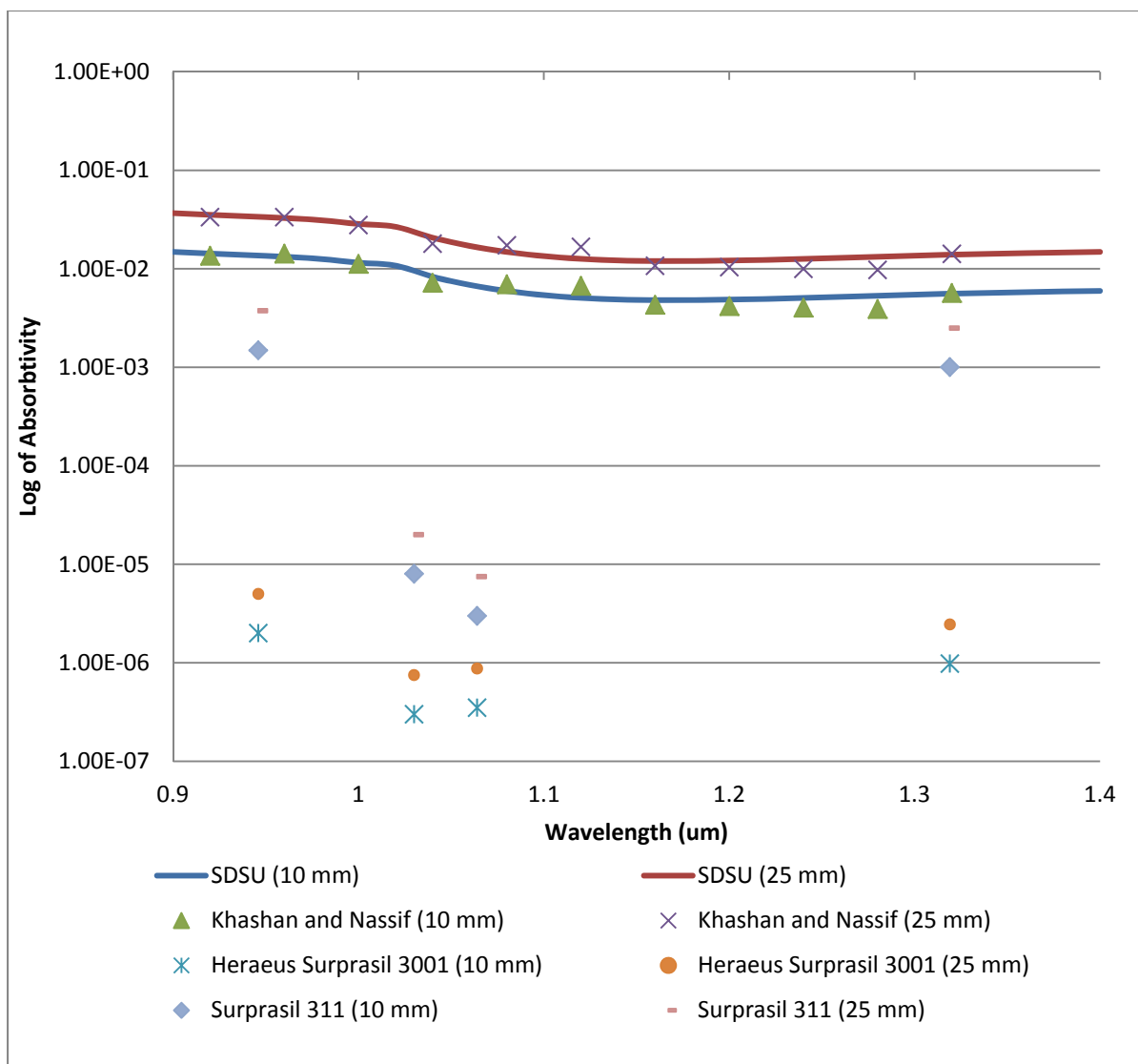


Figure 40. Comparison of absorptivities for 0 degree incident angle.

processing. 1040nm, 1064nm, 1080nm are used in Nd-doped Lasers for material processing. 1319nm is also used in ND-doped Lasers but for medical applications. Their most suitable glasses for these applications are Suprasil 3001, 3002, 300, 311, 312, and Infrasil 301, 302. They claim that Suprasil 3001, 3002, 300 are the best choices for IR. Suprasil 311, 312 is very good for 1064 nm and Infrasil 301, 302 is also very good for longer wavelength [37].

There are two important factors that influence the absorption in optical materials: : Natural OH- absorption bands, and total metal impurity and OH- content within the material. During the manufacturing process, there is an intermediate step reduces the OH- content of the

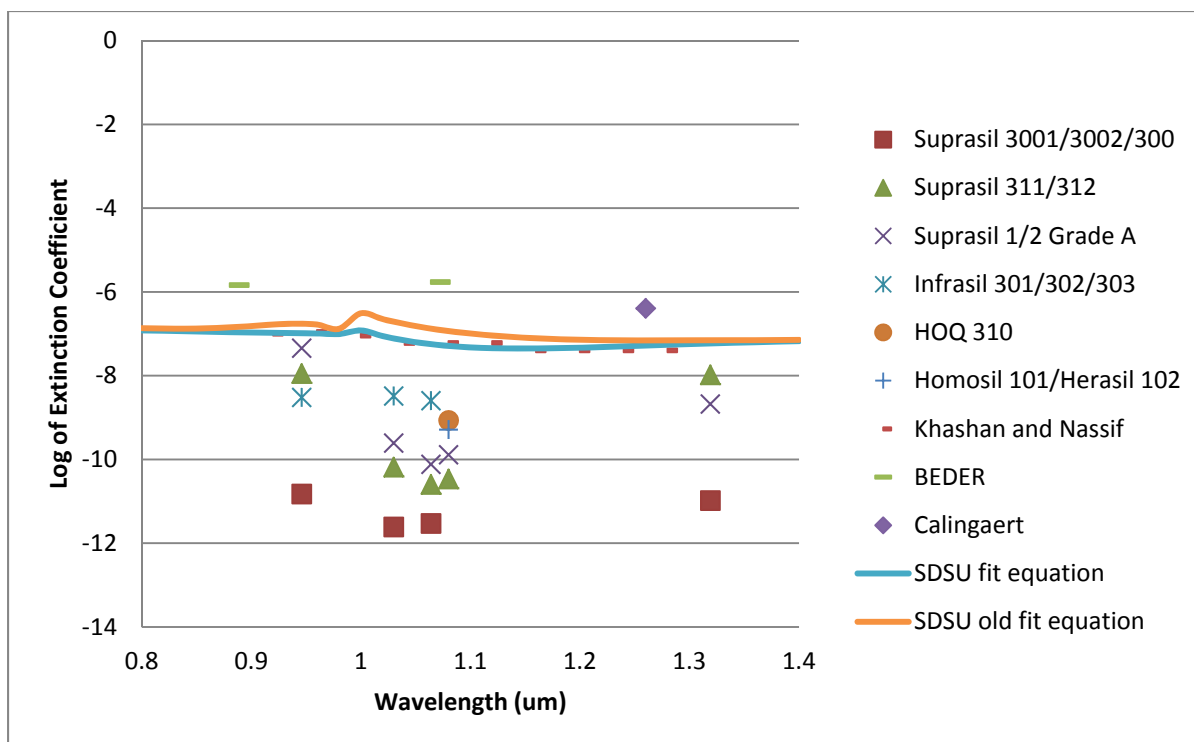


Figure 41. The comparison of absorptive coefficients.

glass for Suprasil 3001, 3002, and 300. A chlorine content of 1000 ppm – 3000 ppm is material inherent and results in a slight shift of the UV-absorption edge to the longer wavelength region.

Figure 42 shows the effect of the OH⁻ concentration on the extinction coefficient for different materials at designated wavelengths. Lower OH⁻ concentration in the material for a specific wavelength will lower the extinction coefficient, thus, absorption.

As mentioned earlier HOQ 310 is a cheaper material but the transmissivity of HOQ 310 is lower compare to Surprasil 3001 and HSQ 310. We have a lack of information for the absorptive index of all three materials. The only optical property that is known is the transmissivity up to 4 μm [37]. Although it will not be exact, the absorptive index can be found by trying different values until reaching the right transmissivity for a specified wavelength, since the refractive index is known. Figure 43 is reached by using this method. The wavelength range shown is from 1 μm to 4 μm because the change in behavior is almost the same for different grades of quartz for shorter wavelength. The blue line is the transmissivity for HOQ 310 and taken from Figure 39. The red line is the transmissivity obtained by trying different absorptive index values. The index of refraction from Dr. Pilon's paper is used for these calculations. The absorptivity and the reflectivity are found by using the absorptive index that is found and the

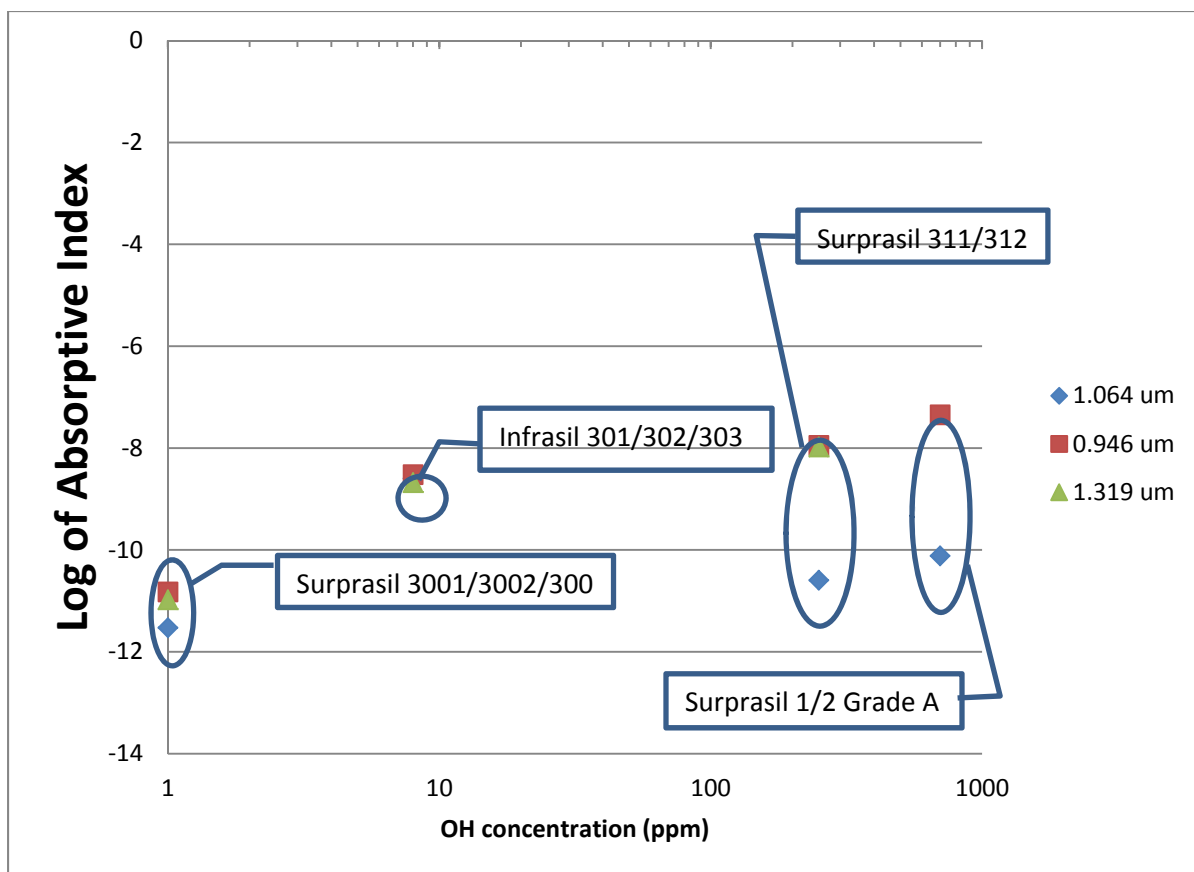


Figure 42. The effects of OH- concentration on the absorptive index.

index of refraction. These values are not exact but approximate. We can get a good sense of how the material will behave optically for now. Therefore, these optical properties will be used for further calculations in this research until the exact values are obtained from the vendor.

The same procedure is followed to find the optical properties of HSQ 300. The results are shown in Figure 44.

Three different materials are being considered so far in this research. First material (base material) is the generic fused quartz. This material is compared with several grades of fused quartz from Heraeus. HSQ 300 for having high transmissivity in the solar spectrum and HOQ 310 for relatively high transmissivity in the solar spectrum and low cost are picked to continue with the research. Another important variable needs to be known before continue with ray tracing is the window geometry.

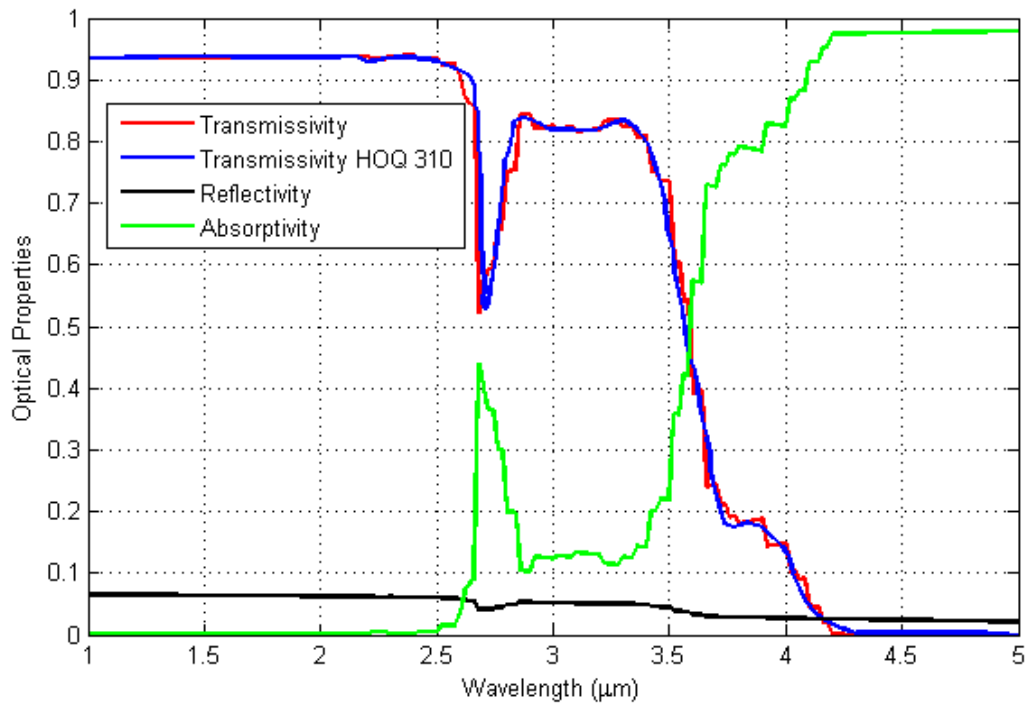


Figure 43. The optical properties of HOQ 310 from both the data taken from the vendor (blue line) and the calculated data (red, green, and black lines) (1 cm thick, 0 degree incident angle).

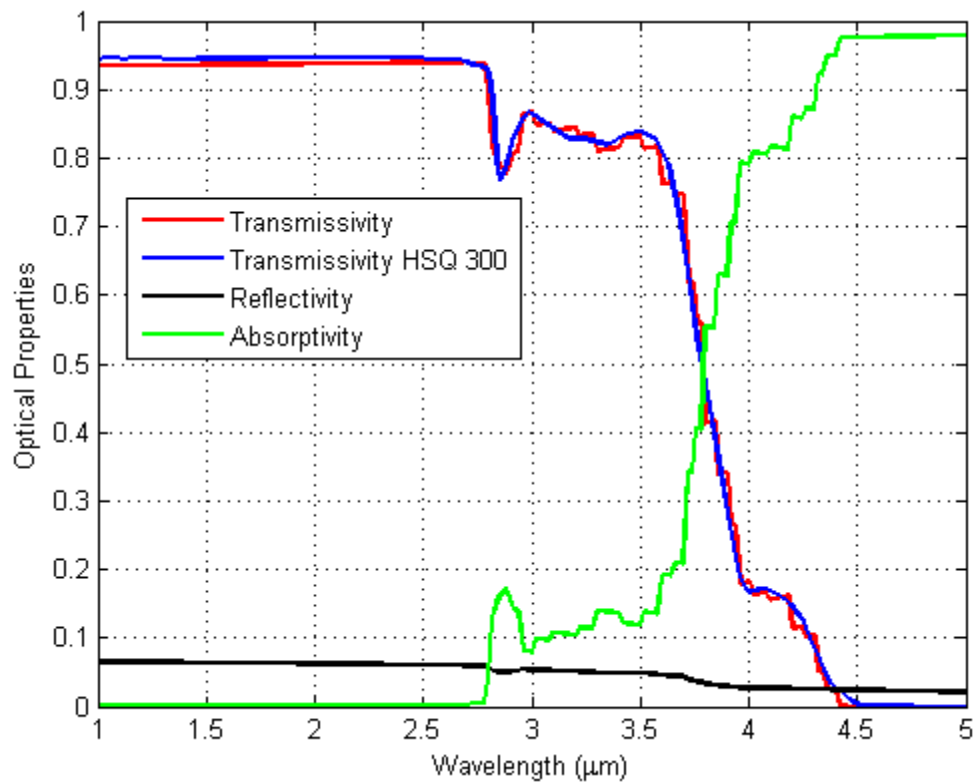


Figure 44. The optical properties of HSQ 300 (1 cm thick, 0 degree incident angle).

CHAPTER 5

WINDOW GEOMETRY

There are two main window shapes being considered so that the window will withstand the pressure within the receiver and help minimize the stresses caused by thermal loading as well as the amount of quartz needed.

The first shape is a spherical cap. One example is shown in Figure 45, 60 degree spherical cap. It is shown that this shape minimizes the amount of the material needed in order to avoid buckling [41]. This shape is easier to manufacture compare to the second shape. The one drawback of this shape is that the tensile stresses near the bottom of the window are not minimized. There are several people in Combustion and Solar Energy Laboratory at San Diego State University still working on the seal design for this window shape to handle tensile stresses. In this research, the different cap angles varying from 0 to 90, in other words from flat to hemisphere, for spherical window will be studied to provide a wide range of results. The cap angle is shown in Figure 46. Another variable, denoted as cr , which is the radius of the circle or window (not the radius of the sphere) is also shown in Figure 46. The equation for spherical cap window is as followed:

$$x^2 + y^2 + (z + r \cos \Phi)^2 = r^2 \quad (40)$$

The second shape is an ellipsoidal shape that Onkar Mande, a former member of Combustion and Solar Energy Laboratory at San Diego State University, came up with [28]. Figure 47 shows the shape. It has been proven that in theory the tensile stresses are eliminated and the entire window is under compression. This shape is harder to manufacture but preferable from a mechanical stand point for quartz. Seal design for this shape is relatively easier. This shape will be compared to the spherical cap for their optical performance. The equation for ellipsoidal window is:

$$\frac{x^2}{cr^2} + \frac{y^2}{cr^2} + \frac{z^2}{\left(\frac{cr*\sqrt{2}}{2}\right)^2} = 1 \quad (41)$$

Where cr is the radius of the circle or window thus $2*cr$ is the diameter of the circle which is shown in Figure 47.

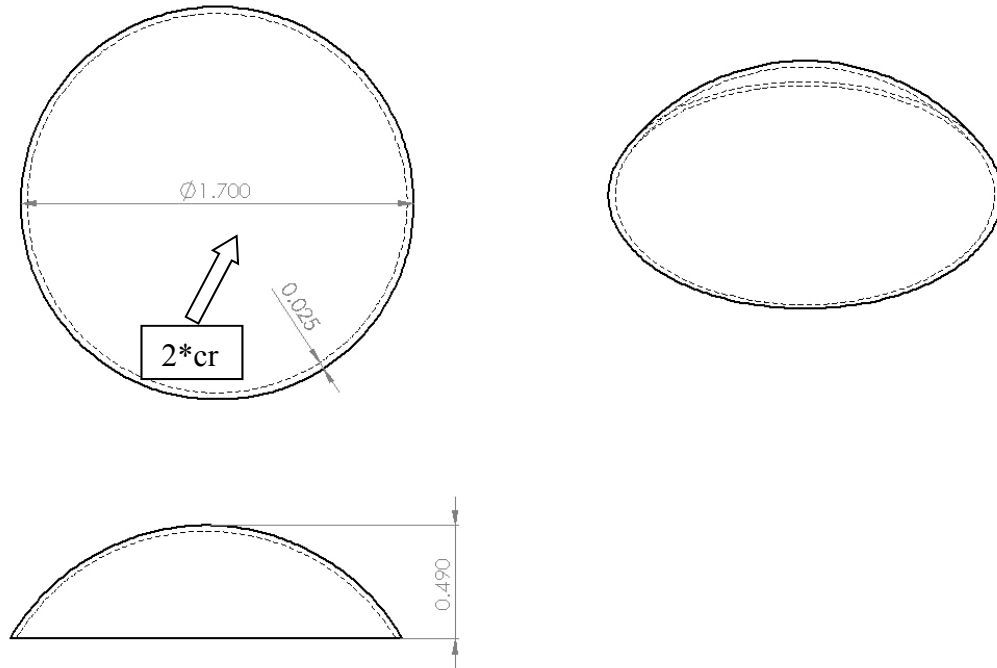


Figure 45. 60 degree spherical window (dimensions are in meters).

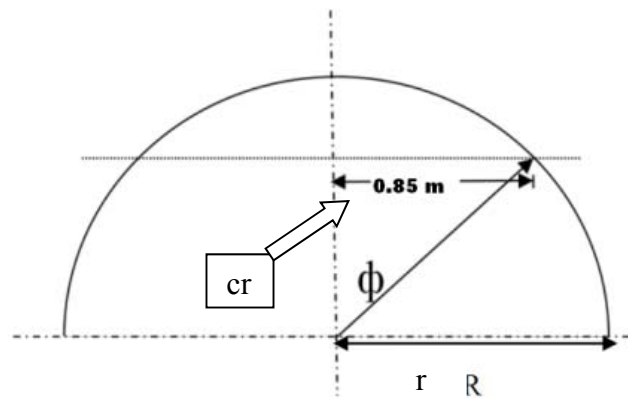


Figure 46. Cap angle.

The radius of the window will be within the range 0.85 to 1 m to allow up to 5 MW solar power to the receiver at the NSTTF, Figure 48. This range is reached by calculating the power reaching the aperture plane depending on the radius of the window. MIRVAL is used for the calculations. In this research, the radius is picked 0.85 m. The optimized radius will be reached eventually after accounting the radiation losses from inside the receiver, something we are currently calculating. The recommended thickness, provided by the vendor, is 2.5cm for this radius.

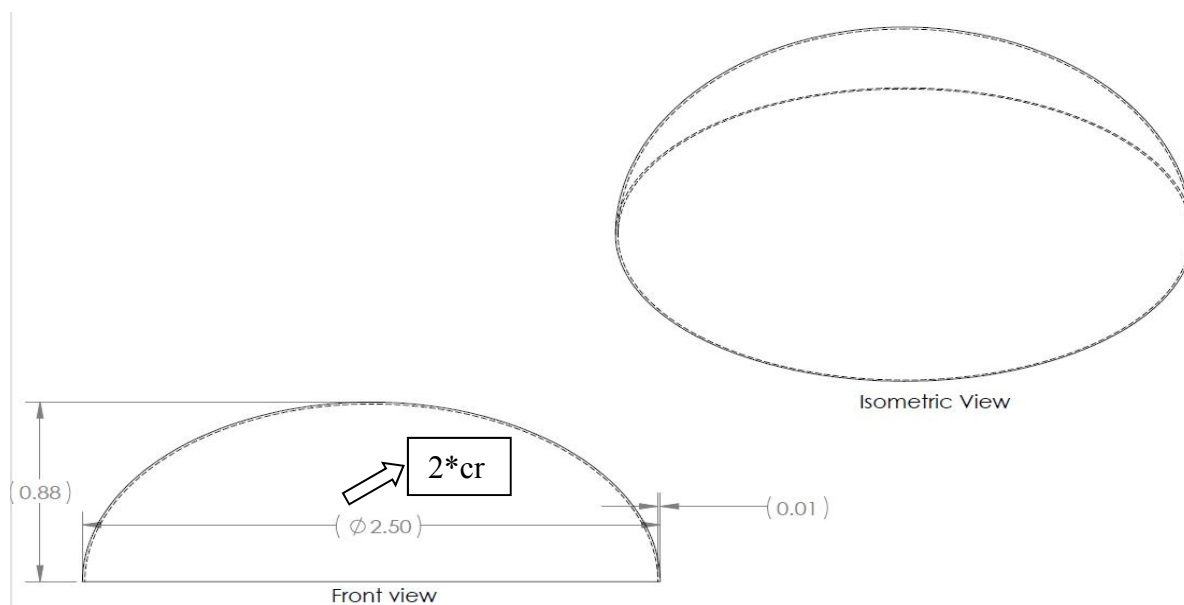


Figure 47. Ellipsoidal window (dimensions are in meters).

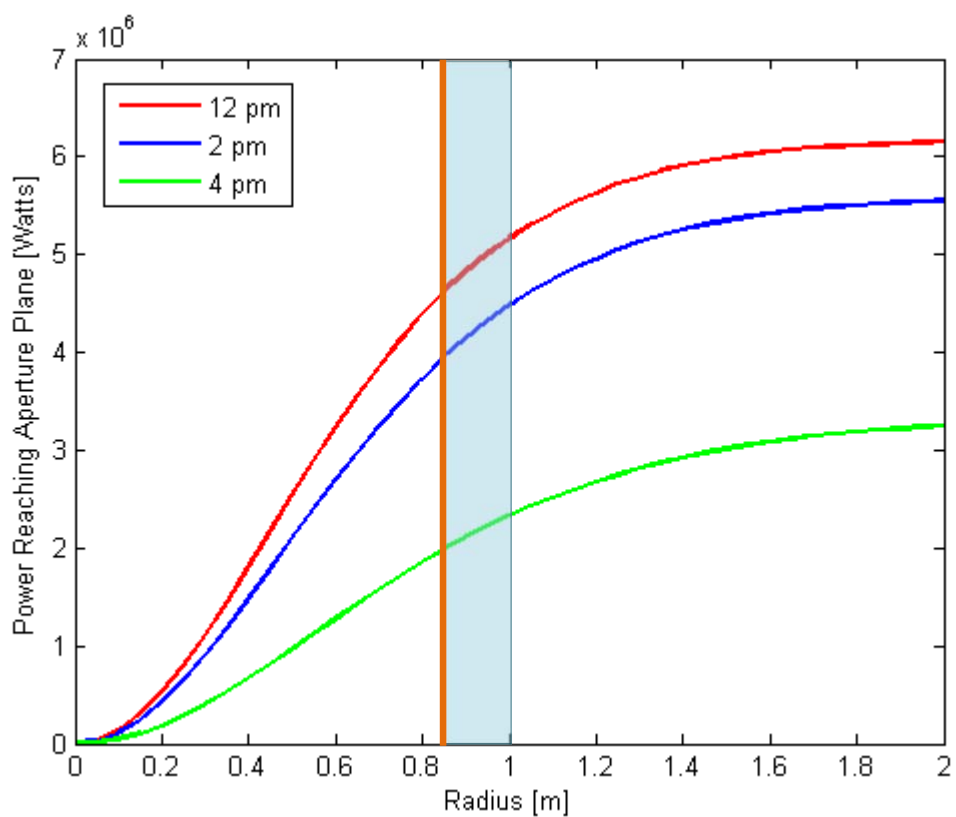


Figure 48. Power vs. radius at the aperture plane considering the range of interest for the diameter of the window.

CHAPTER 6

MONTE CARLO RAY TRACE

Accurate modeling for radiation heat transfer between surfaces with a nonparticipating medium can be done regarding the type of the surfaces by using diffuse transfer analysis or exchange of thermal radiation among nondiffuse nongray surface method [35, 42]. Geometric view factors for each method are needed as input parameters. These view factors can be very difficult to define when complex geometries are involved. The term nondiffuse means the emissivity, reflectivity, transmissivity, and absorptivity can all depend on direction. Nongray means the optical properties can depend on wavelength [35]. The quartz window is a specular nongray surface. Specular surfaces provide reflected radiation at the same magnitude of the angle from the surface normal for incident radiation from a single direction [35].

The Monte Carlo method is another approach for solving radiation heat transfer between surfaces. It is a statistical approach that uses probability concepts to create models for physical events. The Monte Carlo Ray Trace (MCRT) method includes physical events such as photon emission, reflection, absorption, and transmission. It involves tracing rays of photon bundles from the source of emission or reflection through a nonparticipating (or participating) media until they are absorbed by a surface or they leave the problem domain. The direction of the rays and the physical events when a ray encounters a surface are determined by generated random numbers compared with appropriate probability functions. To sum up, there are two main steps to this method. The first step is to create appropriate rays each assigned with a power, and a direction. The second step is to track these rays and keep score of the rays that are leaving the problem domain or absorbed.

These steps are done in MIRVAL for the heliostat field. MIRVAL creates imaginary rays leaving the sun assigned with power. These rays travel through air which is a nonparticipating medium (for the analysis run here) and reach the heliostat field. Then, some reflected rays from the heliostat field reach the power tower as shown in the earlier figures. These two steps constitute the first step of MCRT on the window. The direction, the location at the power tower, and the power of each ray that reached the power tower is recorded. Therefore, these data are the first step of MCRT on the window.

There is one addition to these steps in case of a nongray surface (window). Spectral analysis need to be done for nongray surfaces which means the wavelength of the rays need to be known. MIRVAL does not include the spectral analysis since the heliostats are treated as a gray surface. Therefore, MIRVAL is modified to account for wavelength as explained in Chapter 2, Spectral Variation. Now that the wavelength is known, the second step can be continued.

A computer code called window_TD was developed by the author, by using the MCRT method explained as followed, to trace the rays that are incident on the window as they get absorbed, reflected, or transmitted by the window. Reflected rays were traced until they leave the problem domain or absorption or transmission occurs.

The core of MCRT method is the ray trace part. It is purely a geometrical problem for specular surfaces. The ray trace starts at the aperture plane on the power tower. Important information about the rays such as the location, the direction, the power, and the wavelength are already known at that point. These rays are tracked in a system where there is a curved window until some certain events occur. In this section, tracking these rays will be explained step by step.

There is an algorithm to track rays. This algorithm consists following steps:

1. Choose a location where the emission starts (Given by MIRVAL).
2. Choose a wavelength for the ray if the system has a nongray surface (Added to MIRVAL).
3. Choose the direction of propagation of the ray (Given by MIRVAL)
4. Determine the new location where the ray intersects a surface which is the window. If the ray is a reflected ray, check if the ray hits beyond the boundaries of the window (lost ray). If so, store the information.
5. Decide if the ray is reflected or absorbed or transmitted at the new location (intersection point) using the formula described previously.
6. If the ray is absorbed or transmitted store the information.
7. If the ray is reflected, find the direction of the ray then go to step 4.
8. Repeat step 1 to 6 for adequate number of rays (Chapter 2.1).

There is a new program developed by using Fortran for this research to track the rays by following the steps above. This program is called Window_TD. The data taken from MIRVAL, for the first 3 steps, are in Cartesian coordinate system. Therefore, the same coordinate system was used in Window_TD for most of the calculations. $P_0 = \langle x_0, y_0, z_0 \rangle$ is the location of the departure at the aperture plane. z_0 is always 0 since the coordinate systems for both MIRVAL

and Window_TD are aligned. $\vec{r}^g = \langle r_x^g, r_y^g, r_z^g \rangle$ is a unit vector that defines the direction of incoming rays. PWT is the power of the rays. Wave is the wavelength of the ray in μm .

The equation for the window geometry needs to be known at this point in order to find the intersection point. Several different window geometries are studied. One of the shapes is an ellipsoidal window. The equation for an ellipsoidal window is given in Equation 40. The other shape is a spherical cap and the equation is given in Equation 41.

The location and the direction of the departure are known as well as the equation for the window. Knowing this information, the intersection point at the window can be found by using parametric equations and the equation for the window. Parametric equations (γ) are used to find the relation and are given in Equation 42 to 45.

$$\vec{\gamma}(t) = t * (\vec{r}^g) + P_0 \quad (42)$$

Thus,

$$x = t * r_x^g + x_0 \quad (43)$$

$$y = t * r_y^g + y_0 \quad (44)$$

$$z = t * r_z^g + z_0 \quad (45)$$

Where, t is a scalar.

These parametric equations are plugged in the equations for different windows to find t . An example for a 60 degree spherical cap is shown in Equation 46.

$$(t * r_x^g + x_0)^2 + (t * r_y^g + y_0)^2 + ((t * r_z^g + z_0) + r \cos 60)^2 = r^2 \quad (46)$$

Thus, intersection point $P_i = \langle x, y, z \rangle$ can be found. These calculations lead us to step 5 after finding intersection point.

Step 5 is to decide what happens to the ray at the intersection point. Optical properties of the window are needed at this point. The wavelength of the ray, the thickness of the window, and the incident angle which is defined in Chapter 3 are needed to be passed to optical_properties_TD to find the optical properties. The wavelength of the rays is already known since the information is taken from MIRVAL. The thickness of the window can be chosen once before running the program as a constant variable. The incident angle needs to be calculated.

The translation from global coordinate system to local coordinate system is necessary to simplify the calculations. An imaginary coordinate system will be created at the intersection

point. The origin of the local coordinate system will be aligned with the intersection point. The normal vector at the intersection point will be picked as one of the axes (the local z-axis) of the local coordinate system. The local z-axis will always be pointing inside the receiver. For a surface given, $\emptyset(x, y, z) = ax^k + bx^l + cx^m + d$, the normal vector denoted as \vec{F} is defined as the gradient of the function \emptyset , Equation 47.

$$\vec{F} = \text{Grad } \emptyset = \left\langle \frac{\partial \emptyset}{\partial x}, \frac{\partial \emptyset}{\partial y}, \frac{\partial \emptyset}{\partial z} \right\rangle \quad (47)$$

Unit vectors will be used for all the calculation since the size of a vector does not matter. Thus equation 48 becomes;

$$u\vec{F} = \frac{\vec{F}}{|\vec{F}|} = \vec{z}^l = \langle z_1^l, z_2^l, z_3^l \rangle \quad (48)$$

The other two axes will be defined on the tangent plane at the intersection point. The equation for the tangent plane is given in Equation 49.

$$\text{Grad } \emptyset(x_0, y_0, z_0) \cdot \langle x - x_0, y - y_0, z - z_0 \rangle = 0 \quad (49)$$

A random point will be picked at the tangent plane to define the second axis (local x-axis). A random x and y will be picked and plugged in the equation for tangent plane to find z .

Thus, the local x-axis can be defined as $\vec{x}^l = \langle x_1^l, x_2^l, x_3^l \rangle$

After finding the x-axis and knowing the z-axis, y-axis can be found by taking the cross product of x and z axes. Local y-axis can be defined as $\vec{y}^l = \vec{z}^l \times \vec{x}^l = \langle y_1^l, y_2^l, y_3^l \rangle$.

The direction of the ray is known in the global coordinate system from MIRVAL. It should be transformed to the local coordinate system to find the incident angle. Global and the local coordinate systems are shown in Figure 49. A translation matrix, $[R]$, needs to be formed to handle this process. Such matrix should satisfy the following conditions;

$$[R] \begin{bmatrix} x_1^l \\ x_2^l \\ x_3^l \end{bmatrix} = \begin{bmatrix} 1 \\ 0 \\ 0 \end{bmatrix} \quad (50)$$

$$[R] \begin{bmatrix} y_1^l \\ y_2^l \\ y_3^l \end{bmatrix} = \begin{bmatrix} 0 \\ 1 \\ 0 \end{bmatrix} \quad (51)$$

$$[R] \begin{bmatrix} z_1^l \\ z_2^l \\ z_3^l \end{bmatrix} = \begin{bmatrix} 0 \\ 0 \\ 1 \end{bmatrix} \quad (52)$$

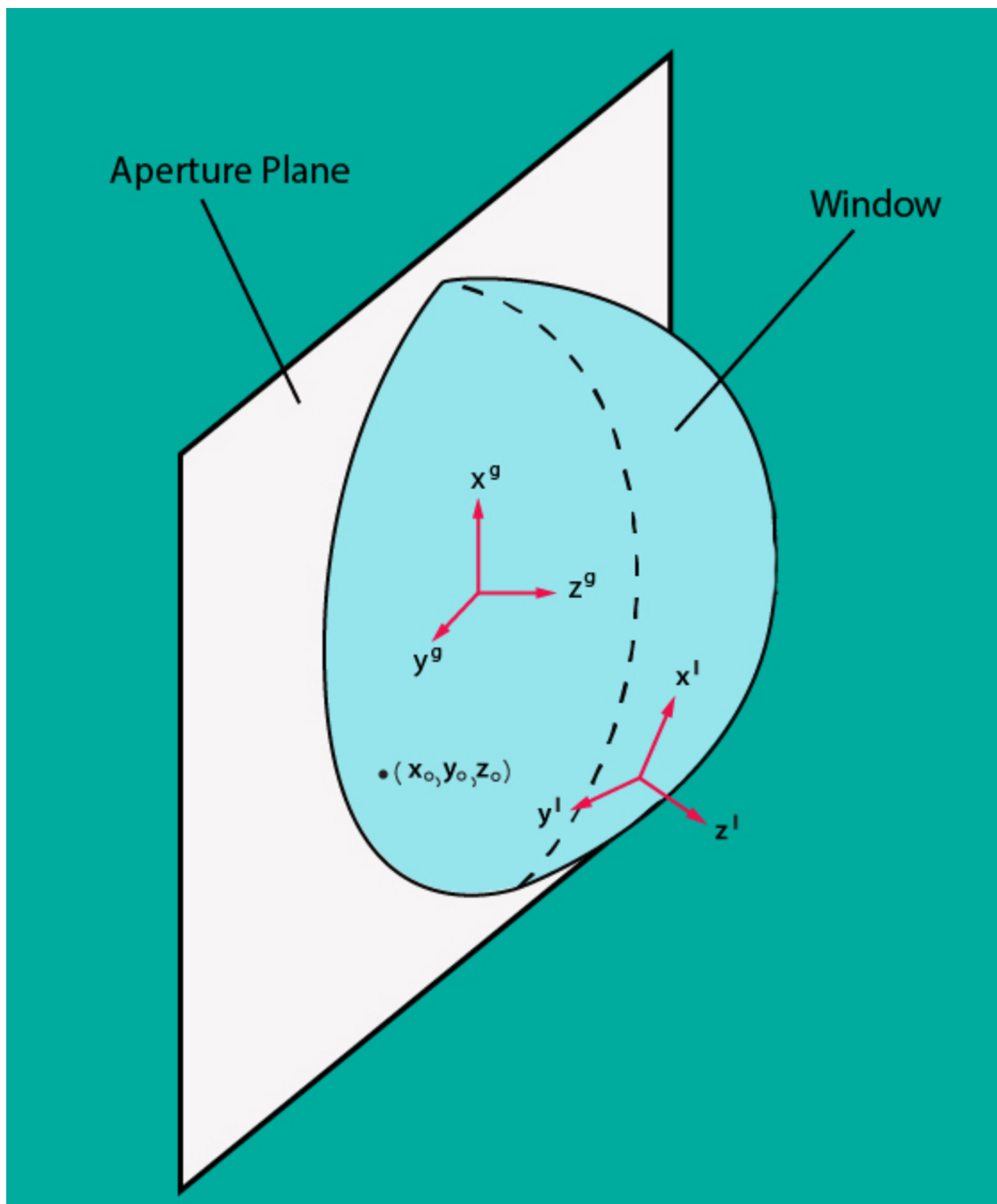


Figure 49. Global and local coordinate systems and the departure at the aperture plane.

Translation matrix should be a 3*3 matrix, defined as:

$$[R] = \begin{bmatrix} R_{11} & R_{12} & R_{13} \\ R_{21} & R_{22} & R_{23} \\ R_{31} & R_{32} & R_{33} \end{bmatrix} \quad (53)$$

Using the condition above a new matrix multiplication can be defined as $A \times x = b$ following:

$$\begin{bmatrix} x_1^l & x_2^l & x_3^l & 0 & 0 & 0 & 0 & 0 & 0 \\ 0 & 0 & 0 & x_1^l & x_2^l & x_3^l & 0 & 0 & 0 \\ 0 & 0 & 0 & 0 & 0 & 0 & x_1^l & x_2^l & x_3^l \\ y_1^l & y_2^l & y_3^l & 0 & 0 & 0 & 0 & 0 & 0 \\ 0 & 0 & 0 & y_1^l & y_2^l & y_3^l & 0 & 0 & 0 \\ 0 & 0 & 0 & 0 & 0 & 0 & y_1^l & y_2^l & y_3^l \\ z_1^l & z_2^l & z_3^l & 0 & 0 & 0 & 0 & 0 & 0 \\ 0 & 0 & 0 & z_1^l & z_2^l & z_3^l & 0 & 0 & 0 \\ 0 & 0 & 0 & 0 & 0 & 0 & z_1^l & z_2^l & z_3^l \end{bmatrix} \begin{bmatrix} R_{11} \\ R_{12} \\ R_{13} \\ R_{21} \\ R_{22} \\ R_{23} \\ R_{31} \\ R_{32} \\ R_{33} \end{bmatrix} = \begin{bmatrix} 1 \\ 0 \\ 0 \\ 0 \\ 1 \\ 0 \\ 0 \\ 0 \\ 1 \end{bmatrix} \quad (54)$$

Where,

$$A = \begin{bmatrix} x_1^l & x_2^l & x_3^l & 0 & 0 & 0 & 0 & 0 & 0 \\ 0 & 0 & 0 & x_1^l & x_2^l & x_3^l & 0 & 0 & 0 \\ 0 & 0 & 0 & 0 & 0 & 0 & x_1^l & x_2^l & x_3^l \\ y_1^l & y_2^l & y_3^l & 0 & 0 & 0 & 0 & 0 & 0 \\ 0 & 0 & 0 & y_1^l & y_2^l & y_3^l & 0 & 0 & 0 \\ 0 & 0 & 0 & 0 & 0 & 0 & y_1^l & y_2^l & y_3^l \\ z_1^l & z_2^l & z_3^l & 0 & 0 & 0 & 0 & 0 & 0 \\ 0 & 0 & 0 & z_1^l & z_2^l & z_3^l & 0 & 0 & 0 \\ 0 & 0 & 0 & 0 & 0 & 0 & z_1^l & z_2^l & z_3^l \end{bmatrix} \quad (55)$$

$$b = \begin{bmatrix} 1 \\ 0 \\ 0 \\ 0 \\ 1 \\ 0 \\ 0 \\ 0 \\ 1 \end{bmatrix} \quad (56)$$

$$x = \begin{bmatrix} R_{11} \\ R_{12} \\ R_{13} \\ R_{21} \\ R_{22} \\ R_{23} \\ R_{31} \\ R_{32} \\ R_{33} \end{bmatrix} \quad (57)$$

This matrix can be solved by using two different methods since x is unknown. One is to take the inverse of A and multiply it with both sides and solve for x . The other is to use the LU decomposition method. LU decomposition method is chosen because the computation time for LU decomposition is faster for this problem. Calculations below are followed:

$$A = L \times U \quad (58)$$

$$A \times x = L \times U \times x = L \times y = b \quad (59)$$

$$L \times y = b \quad (60)$$

$$U \times x = y \quad (61)$$

Solve Equation 60 for y then solve Equation 61 for x . Thus, the translation matrix $[R]$ is formed.

The direction of an incoming ray was given as $\vec{r}^g = \langle r_x^g, r_y^g, r_z^g \rangle$ in global coordinate system. Multiplying this direction vector with the translation matrix will give the direction in the local coordinate system, $\vec{r}^l = \langle r_x^l, r_y^l, r_z^l \rangle$.

$$\begin{bmatrix} R_{11} & R_{12} & R_{13} \\ R_{21} & R_{22} & R_{23} \\ R_{31} & R_{32} & R_{33} \end{bmatrix} \begin{bmatrix} r_x^g \\ r_y^g \\ r_z^g \end{bmatrix} = \begin{bmatrix} r_x^l \\ r_y^l \\ r_z^l \end{bmatrix} \quad (62)$$

Thus the incident angle, the zenith angle, can be defined as, $\theta = \cos^{-1}(r_z^l)$.

At this point, the incident angle, shown in Figure 50, and the wavelength are known. Therefore, the optical properties of the glass can be found by following the methods explained in Chapter 3. The optical properties; the absorptivity, α , the transmissivity, τ , and the reflectivity, ρ , will add up to 1. A random number, Ran , with the range of $0 \leq Ran \leq 1$ is picked to decide what will happen to the ray. If the random number is smaller than the value of transmissivity then the ray will be transmitted. If the random number is bigger than the value of transmissivity, and smaller than the sum of the absorptivity and transmissivity, then the ray will be absorbed.

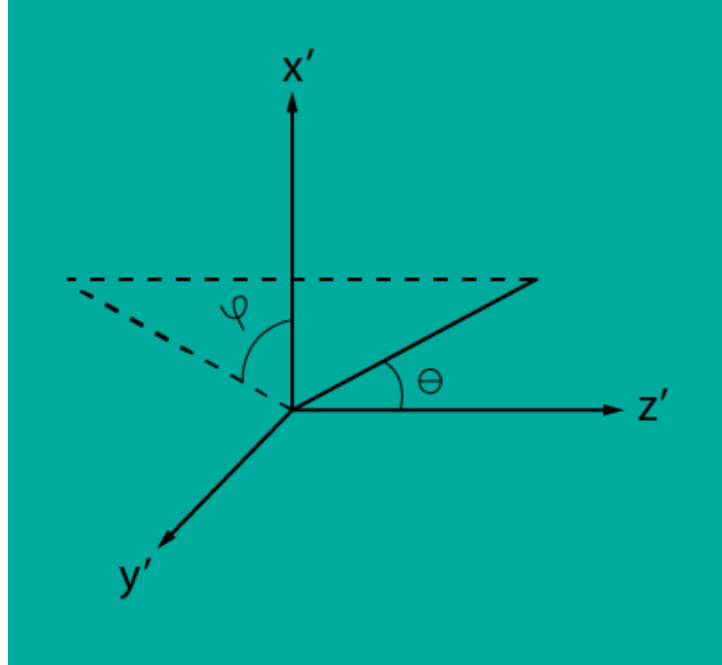


Figure 50. Incident angle.

Finally, if the random number is bigger than the sum of the absorptivity and transmissivity then the ray will be reflected. This decision will conclude step 5.

Step 6 is to store the information in case of absorption and transmission to use later for different studies.

Step 7 is to find the direction of the reflected ray. As it is seen in Figure 51, zenith angle for reflected ray will remain the same while azimuth angle is changing. The direction of the ray will also change along z-axis. The direction of the reflected ray is $\vec{r}_{ref}^l = \langle r_{x,ref}^l, r_{y,ref}^l, r_{z,ref}^l \rangle$ and each component is defined in following equations.

$$r_{x,ref}^l = -\sin(\theta) \cos(\varphi + \pi) \quad (63)$$

$$r_{y,ref}^l = -\sin(\theta) \sin(\varphi + \pi) \quad (64)$$

$$r_{z,ref}^l = -\cos(\theta) \quad (65)$$

Where,

$$\varphi = \tan^{-1} \left(\frac{r_y^l}{r_x^l} \right) \quad (66)$$

After finding the direction of the reflected ray, step 4 can be followed again with redefining some information. First intersection point will be treated as if it is the location where departure starts just like step 1. On the other hand, the direction will be treated as if it is the

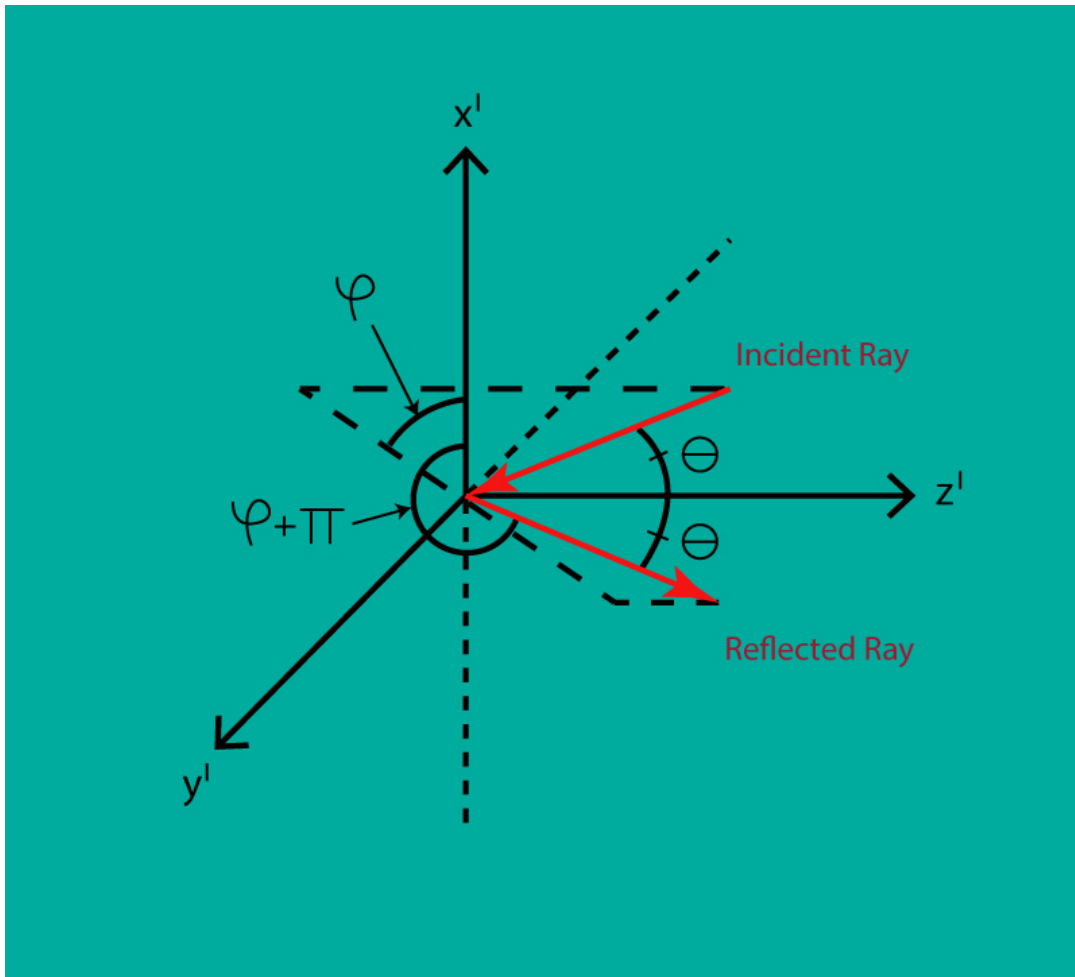


Figure 51. Zenith and azimuth angles for the reflected ray.

direction of the emission just like step 3. Wavelength will remain the same, step 2. Thus, the necessary information was redefined to follow step 4.

Final step, step 8, is to repeat step 1 to 7 for adequate number of rays. This number is related to the number of grids as it is explain earlier in Chapter 2.

CHAPTER 7

RESULTS

There are several points discussed in this thesis so far. First, the concept of power tower systems, which is one of the concentrated solar power systems, was discussed. Second, how to use MIRVAL and how it is modified was discussed. Third, the optical properties of the window were determined. Forth, the material of the window was discussed as well as the geometry. Finally, the Monte Carlo Ray Trace was explained. At this point we have all the pieces to finish the puzzle and determine heat load on the window and the transmission through the window.

MIRVAL, the computer code written in Fortran, calculates the solar flux at the aperture plane at the power tower. Optical_properties_TD, the computer code written in Fortran, calculates the optical properties of the window. Window_TD, the computer code written in Fortran, traces the rays from the aperture plane to the window. All these codes were coupled to calculate determine heat load on the window and the transmission through the window. After coupling, we now have a complete code, MIRVAL_Window_TD that can trace the rays coming from the sun until they enter the receiver through the window.

The final code, MIRVAL_Window_TD, is capable of calculating the solar radiation that is absorbed by the window and solar radiation that enters the receiver by passing the window as well as reflective losses to the ambient from the window. These events are highly important to determine. Absorbed radiation will affect the temperature of the window. Transmitted radiation will help us determine outlet temperature of the flowing fluid inside the small particle solar receiver realistically. There are several other events that will be determined by using this code but these two are the most important events. Considering these events, the window is the key component of the small particle solar receiver.

There are several parameters can be adjusted according to the needs of MIRVAL_Window_TD. The main ones are the tilt angle and the location of the receiver at the power tower, the shape and the thickness of the window, the time and the day of the year. All these parameters except the location of the receiver were varied and studied as shown in the following sections in this chapter.

TILT ANGLE STUDY

The very first study that is done is the tilt angle study. Tilt angle is represented by DELTAD in MIRVAL, Figure 8. Power reaching the aperture plane or the window is dependent on the tilt angle as well as the direction and the location of the rays. The main purpose for our studies is to get as much as solar radiation at the aperture plane, thus window, within a certain radius. Power reaching the aperture plane will be always higher than the power reaching the window since the projected area of the window at the aperture plane is smaller than the area of the concentrated solar radiation at the aperture plane. The concentrated solar radiation received by the window is more important for our studies. Therefore power reaching the window is studied with respect to the tilt angle in the following graphs.

Figure 49 shows the power reaching the window depending on the tilt angle. The study is done on March 21st at 12 pm. 200 million rays were used for the computations for consistency although 16 million rays were enough for this particular study. The flux maps that are shown in Chapter 2 are created for the tilt angle of 23.8. It was mentioned that this angle was picked because at this angle the receiver points to the middle of the heliostat field. It was assumed that the highest heat flux would be accomplished with this angle. We can tell that this assumption is not a valid assumption by looking at Figure 49. In the figure, the highest power, approximately 4.6 MW, is achieved at 26.5 degree tilt angle. The heat flux is the power divided by the area of the window. The radius of the window is 1.7 m and kept the same for different tilt angles. Therefore the highest power will give the highest average heat flux. The reason why 23.8 degree tilt angle is not valid is because the heliostats in the field are not evenly distributed. Some rows have more heliostats than the others, Figure 7.

Surely, power reaching the window will give a lot of information but power entering the receiver through the window is actually what we are interested in. That will not only depend on the power reaching the window but also the geometry of the window. The geometry of the window will affect the incident angle of the incoming radiation at the window. That will, along with the thickness of the window and the wavelength of the incident radiation, affect the optical properties of the window. So the transmission will be different for different geometries. Therefore, the power entering the receiver through the window should be studied depending on the geometry and the tilt angle. Figure 52 gives a nice clue about where to start the study.

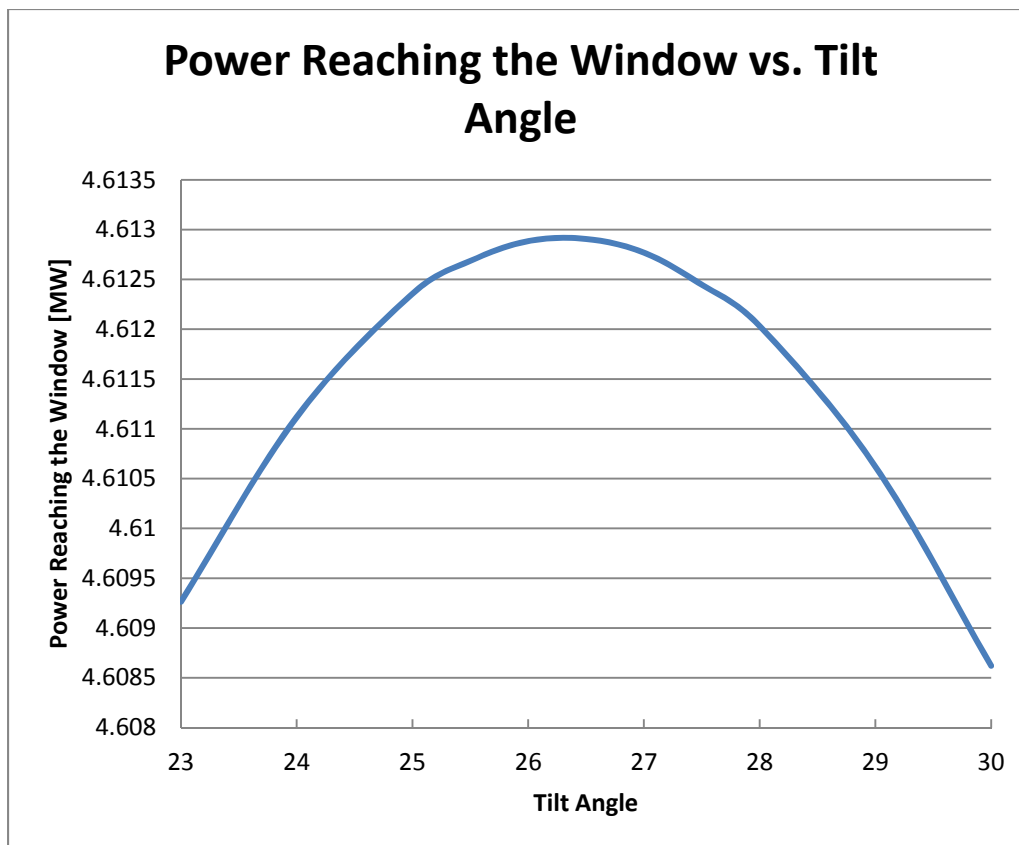


Figure 52. Power reaching the window vs. tilt angle on 3/21 at 12 pm.

Figure 53 shows the power entering the receiver with respect to the tilt angle for different window shapes. Results show that the maximum power entering the receiver is reached at different tilt angles depending on the window shape. For ellipsoidal window and 45 degree spherical window, 26.5 degree tilt angle is the best. For 60 degree spherical window this number is 26.0.

The same study is done in the same conditions except the time is changed to 2 pm, Figure 54. Results show that for ellipsoidal window and 45 degree spherical window, 27 degree tilt angle is the best. For 60 degree spherical window this number is 25.5. Comparing the results, it is concluded that for both ellipsoidal window and the 45 degree spherical window 26.5 degree cap angle and for 60 degree spherical window 25.5 degree tilt angle are good tilt angles. It is also concluded that time does not have a large role in determining the optimal tilt angle and window shape is more important than tilt angle.

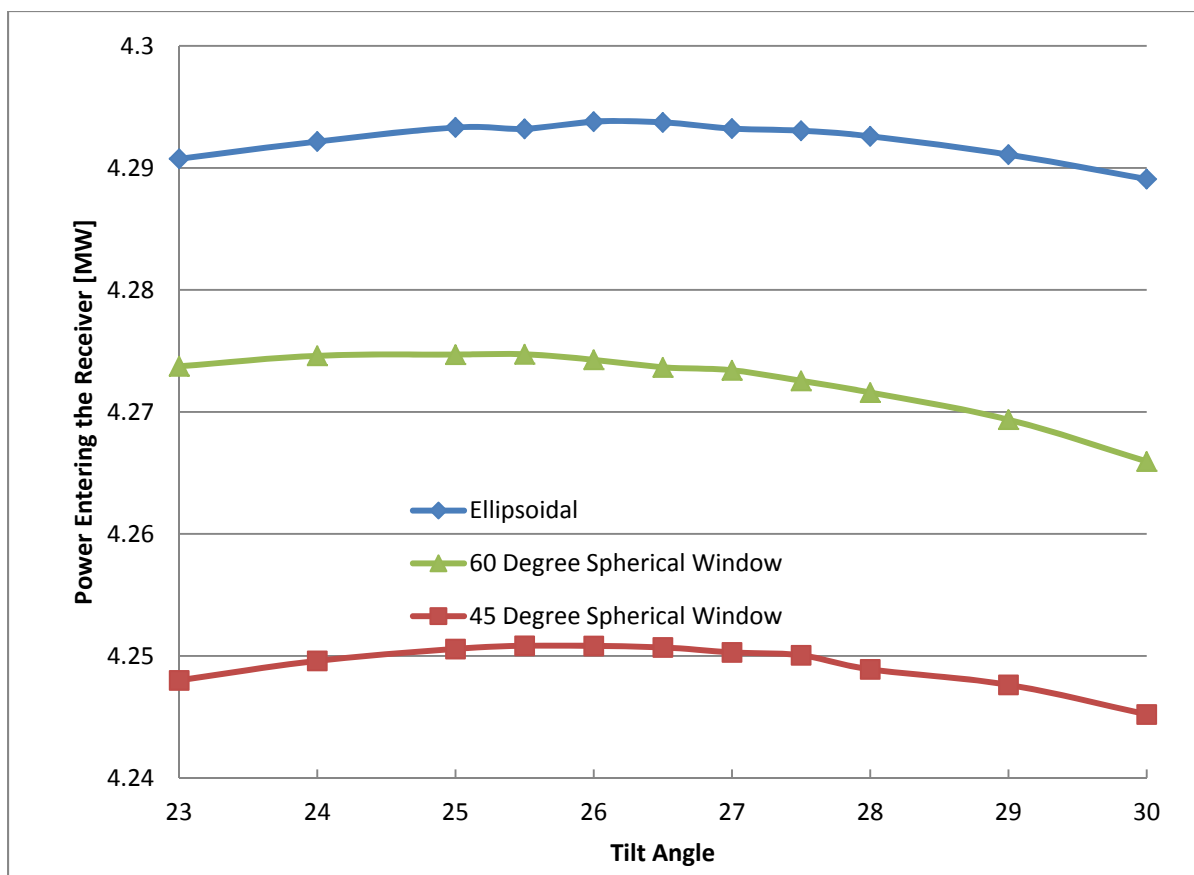


Figure 53. Power entering the receiver vs. tilt angle on 3/21 at 12 pm.

The HOQ 310 (window material) is used for all the tilt angle studies. Although the power entering the receiver will be different depending on the material, the material will not have an effect on the tilt angle.

INCIDENT ANGLE STUDY

In Chapter 3, the incident angle at the aperture plane (i.e, a flat window) was studied. The reason is that the drastic change after 60 degree incident angle on the optical properties brings the worry of having low transmissivity. Now that all the codes are coupled, we can determine the incident angle of the incoming rays reaching the window for different window geometries. Figure 55 for ellipsoidal window, Figure 56 for 60 degree spherical window, and Figure 57 for 45 degree spherical window, all show that only small percentages of the rays that are hitting the window have a 60 degree or higher incident angle, for the time calculated.

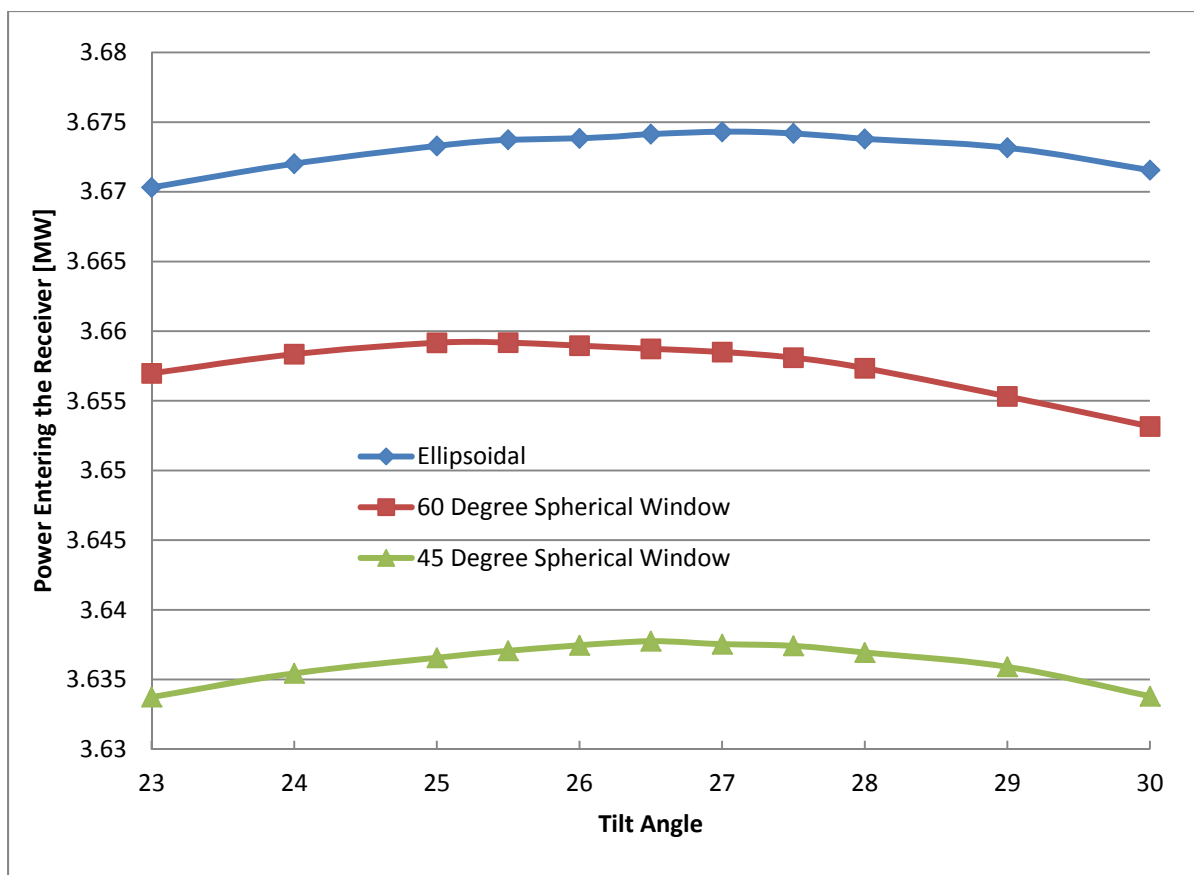


Figure 54. Power entering the receiver vs. tilt angle on 3/21 at 2 pm.

THICKNESS STUDY

The thickness of the window is one of the key elements affecting the optical properties of the window, thus the absorption, transmission, and reflection losses. The absorption is the ratio of the absorbed radiation in the body (window) to the incoming radiation on the body. The transmission is the ratio of the transmitted radiation through the body to the incoming radiation on the body. The reflection loss is the ratio of the lost radiation after the reflection from the body to the incoming radiation on the body. Here it should be clear that the reflected radiation from the window (body) will not be lost in every case unless the window is flat. Some of the reflection might hit the window again in the case of a curved window.

The effect of thickness of the window for different geometries is studied with the transmission, absorption, and the reflection. The following studies are done on March 21st at 12 pm and 200 million rays are used. The tilt angle for both the ellipsoidal window and the 45 degree spherical window is 26.5 and it is 25.5 for 60 degree spherical window. Absorption in the

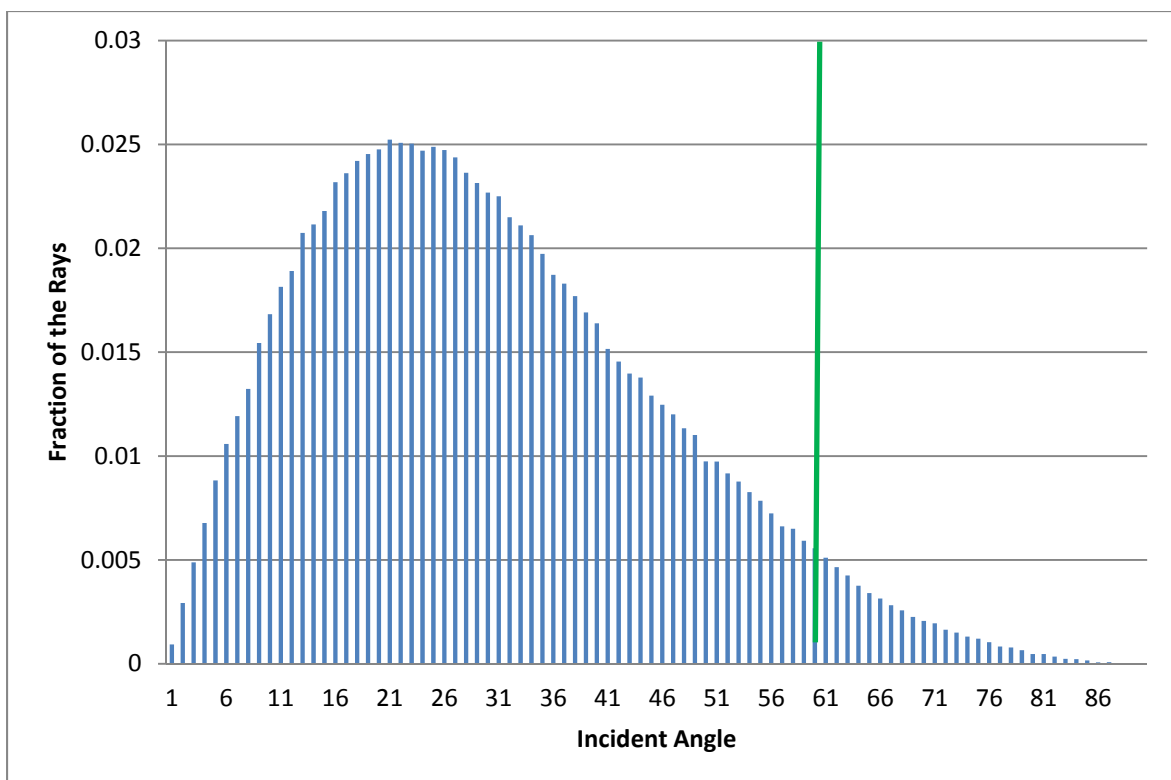


Figure 55. Frequency for ellipsoidal window.

window is expected to increase as the thickness of the window increases. The reason is that the radiation will have a longer path length to travel within the window. Figure 58 proves this expectation. The window thickness is varied from 10 mm to 40 mm. There are three window shapes studied: 45 spherical window, 60 degree spherical window, and ellipsoidal window. It is observed that the absorption for different windows is almost the same for a specific angle since the path length of the radiation will not be affected much for different window shapes however the absorbed flux is different since the total power is the same but the surface area of the windows is different.

Transmission vs. thickness is shown in Figure 59. The transmission decreases as the window thickness increase. The reason is that more absorption is gained by the window. It is observed that the ellipsoidal window will have more transmission than both spherical windows. This difference in transmission for a chosen thickness is coming from reflected radiation. As mention earlier, the reflected radiation might hit the window again depending on the window shape. This phenomenon is the case here. If the transmission is higher for ellipsoidal window and

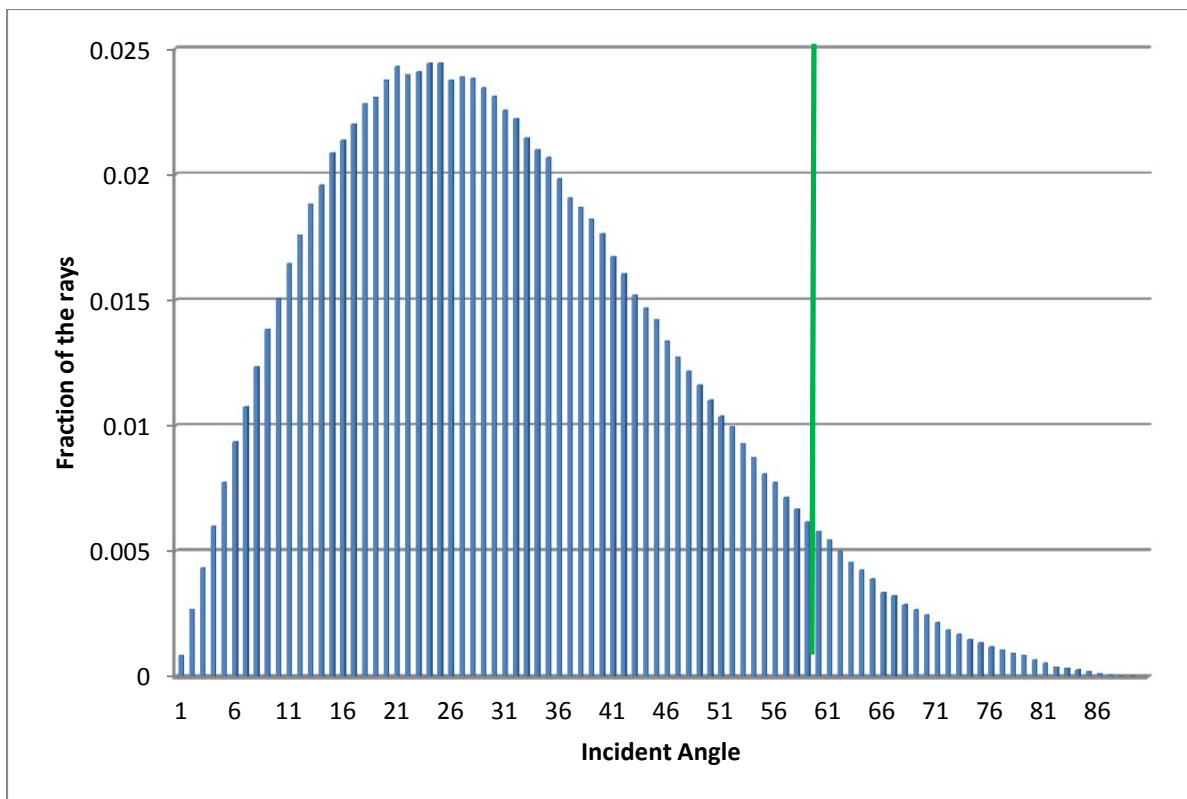


Figure 56. Frequency for 60 degree spherical window.

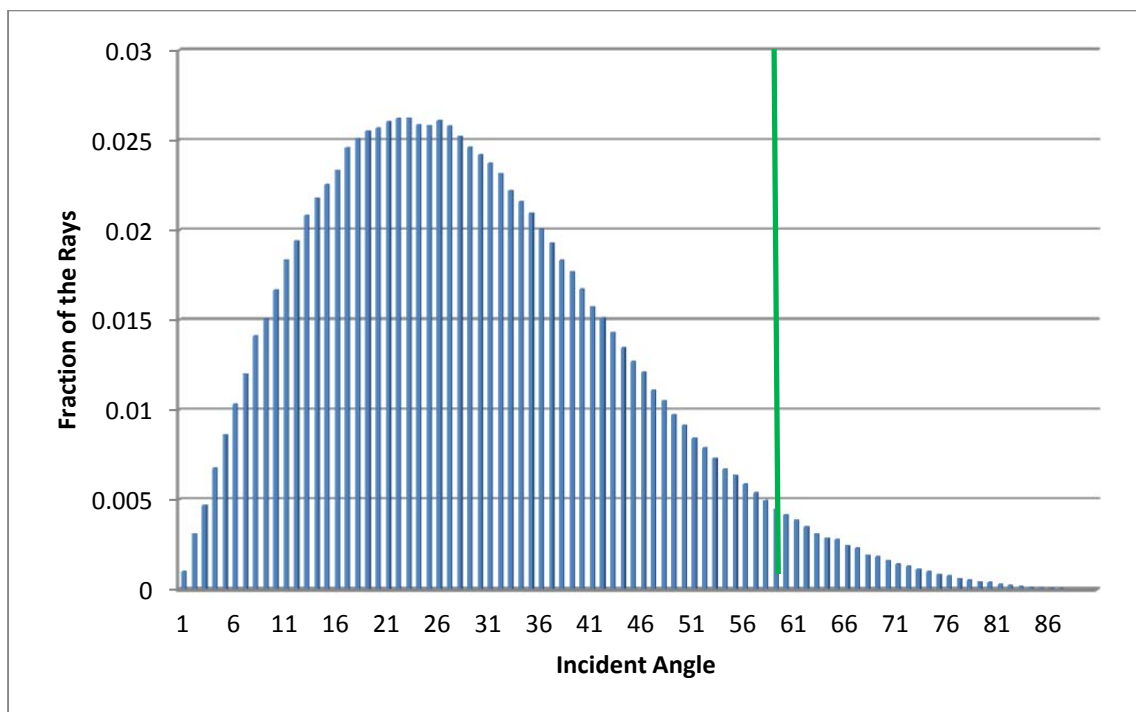


Figure 57. Frequency for 45 degree spherical window.

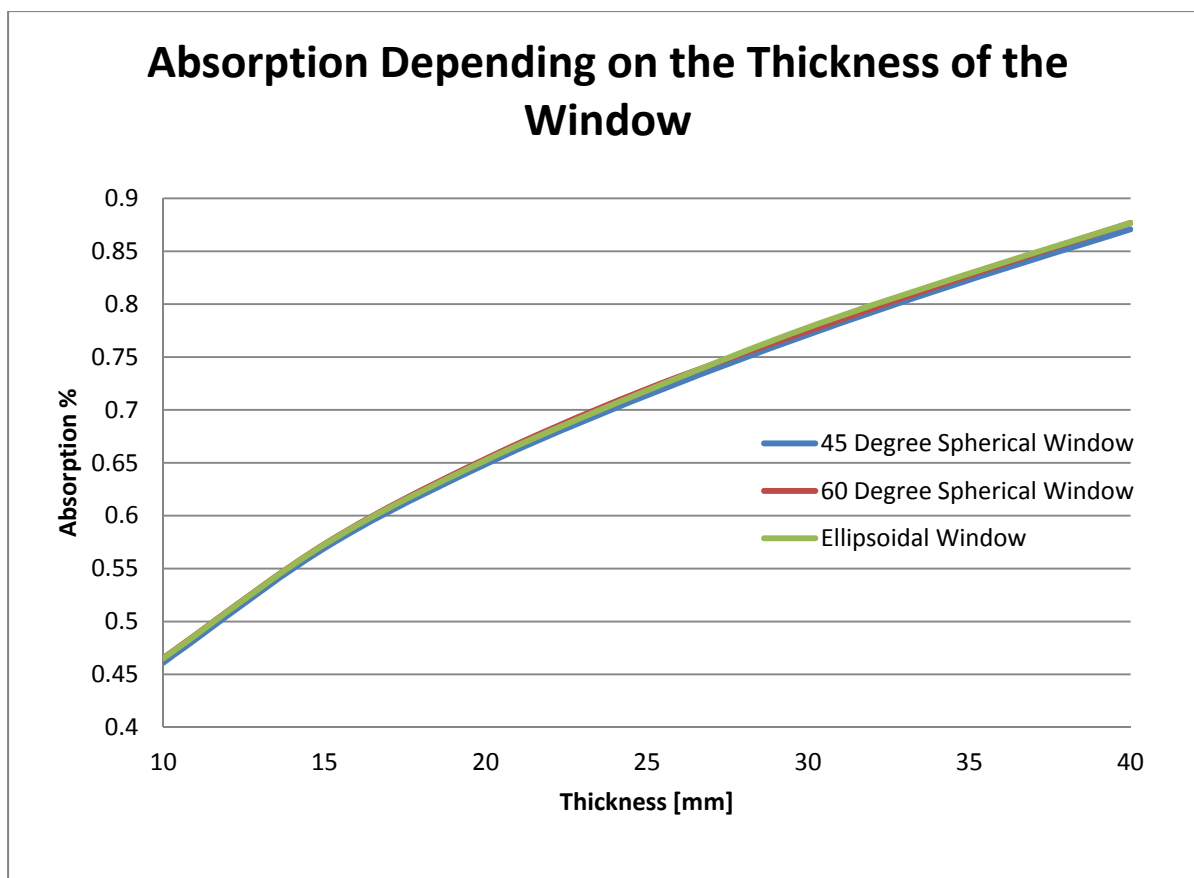


Figure 58. Absorption for different geometries and thicknesses (HOQ 310).

the absorption is almost the same compared to the other window shapes, it is expected that the reflection losses will be less for ellipsoidal window, Figure 60.

Figure 60 shows that reflection is essentially not changed at all by the window shape. On the other hand, the amount of energy absorbed doubles over the thickness range studied. This basically tells that the thicker window will be hotter. Therefore, cooling load will increase for the window.

The suggested window thickness from the vendor is 25 mm, as mentioned earlier. For 25 mm ellipsoidal window, the absorption is a little bit over 0.7%, the transmission is approximately 93.1%, and the reflection losses is 6.2% . For 25 mm 45 degree spherical window, the absorption is a little bit over 0.7%, the transmission is approximately 92.15%, and the reflection losses is 7.15% . For 25 mm 60 degree spherical window, the absorption is a little bit over 0.7%, the transmission is approximately 92.65%, and the reflection losses is 6.65%.

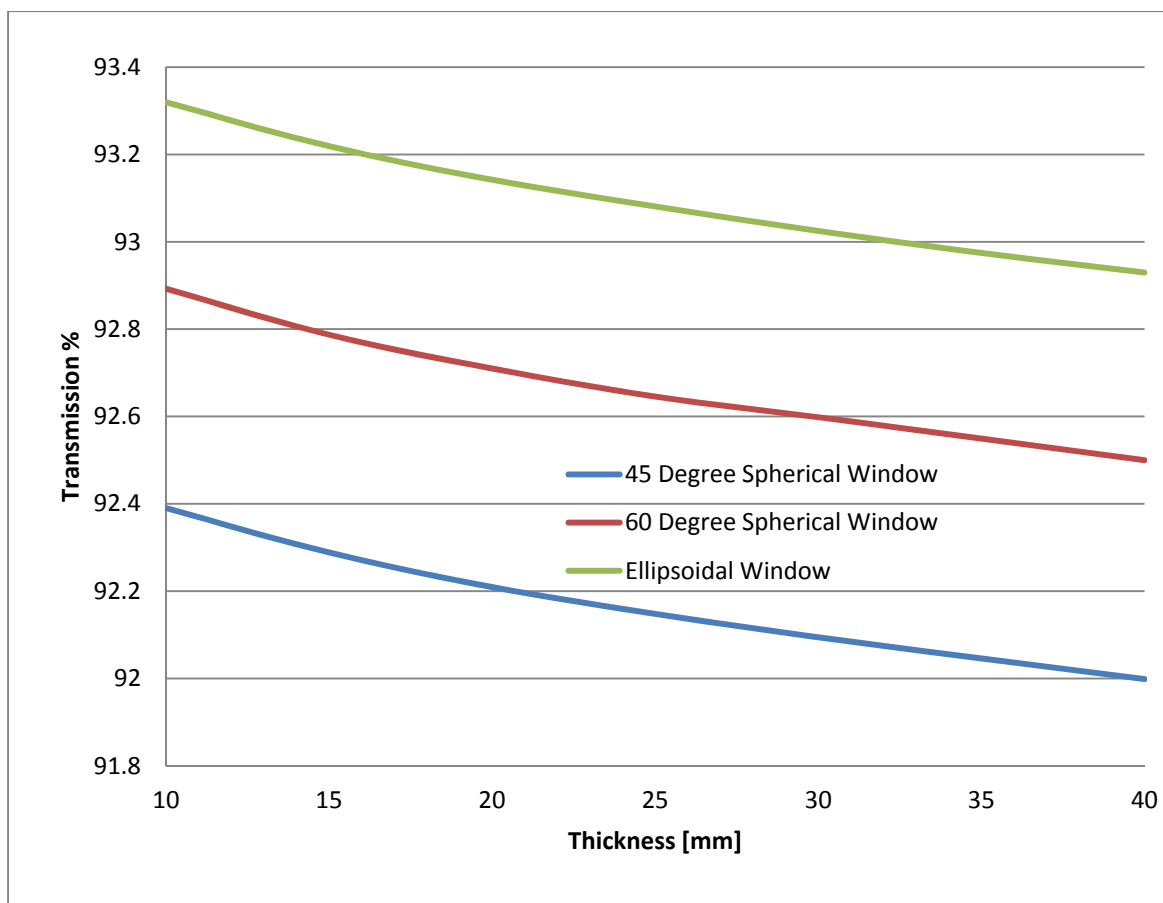


Figure 59. Transmission for different geometries and thicknesses (HOQ 310).

THE EFFECTS OF THE GEOMETRY

The effects of the geometry can be somewhat seen for only three window shapes in the previous study when looked at the transmission for a chosen thickness. In this section, the cap angle for spherical cap is varied from 0 degree to 90 degree and compared with the ellipsoidal window. Zero degree cap angle means flat window and 90 degree cap angle means hemisphere. The studies are done on March 21st at 12 pm and 200 million rays are used again. Tilt angle for both ellipsoidal window and the spherical windows is 26.5. In these studies, the effect of the window material is also important. Three different materials are considered. One is the generic fused quartz from Dr. Pilon's research [34]. The other two are HSQ 300, considered because of high transmission, and HOQ 310, considered because of relatively high transmission and cheaper material [37].

The transmission study, Figure 61, shows that the transmission decreases as the cap angle increase until 45 degree then it starts to increase. The reason is that the incident angle of the

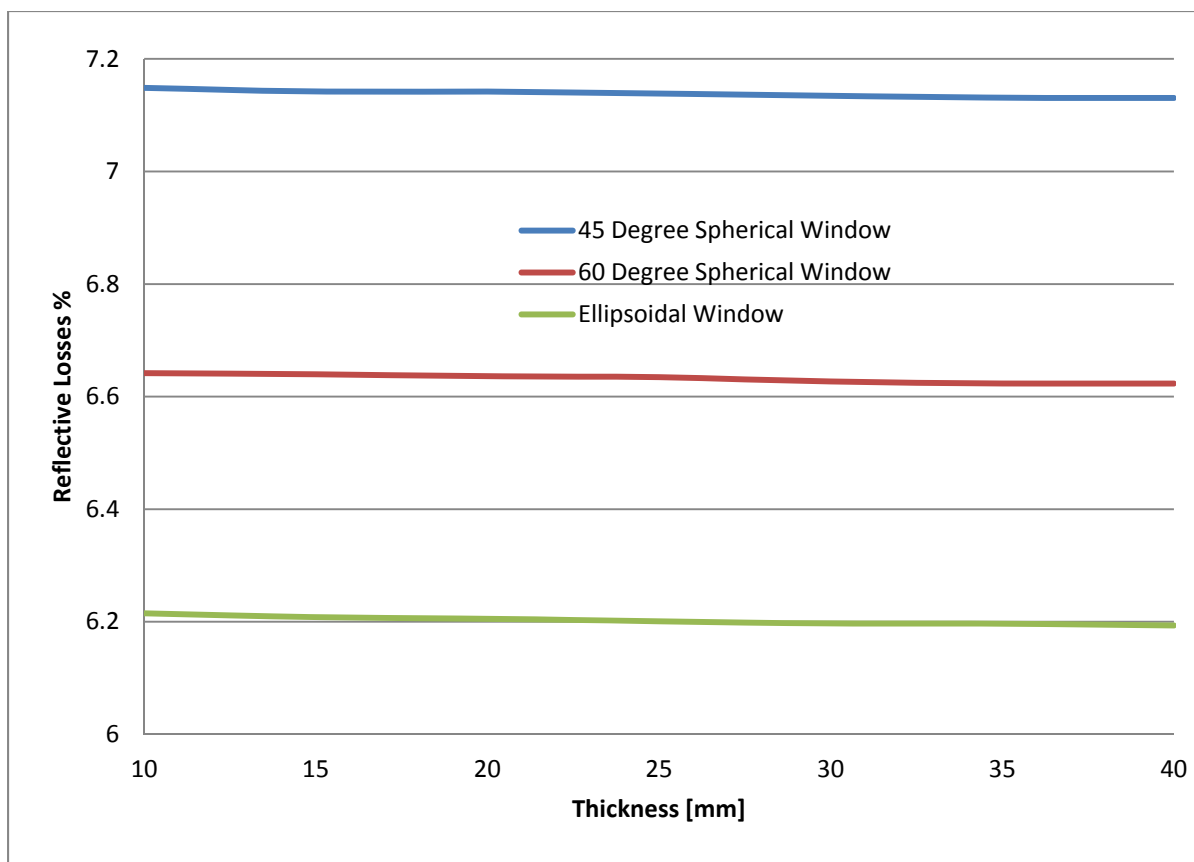


Figure 60. Reflective losses for different geometries and the thicknesses.

radiation changes with the geometry. The higher incident angle will result in higher reflection and most of the reflection is lost until 45 degree cap angle. After 45 degree cap angle the most of the reflection will hit the window again and most of it is transmitted. In another words, more radiation is captured. This phenomenon increases the transmission. The highest transmission is reached for hemisphere window. Transmission for ellipsoidal window correspond the transmission for 70 degree spherical window. The highest transmission is reached when HSQ 300 is used. The difference is slight between HSQ 300 and HOQ 310. On the other hand, the transmission for the generic fused quartz is very low compare to HSQ 30 and HSQ 310.

The absorption always increases as the cap angle increases. But Figure 62 shows that the increase is higher when cap angle is higher than 45 degree because more radiation will hit the window after reflection. On the other and the reflection losses behave exactly opposite compared to the transmission. HSQ 300 has the least amount of absorption and the generic fused quartz has the most amount of absorption.

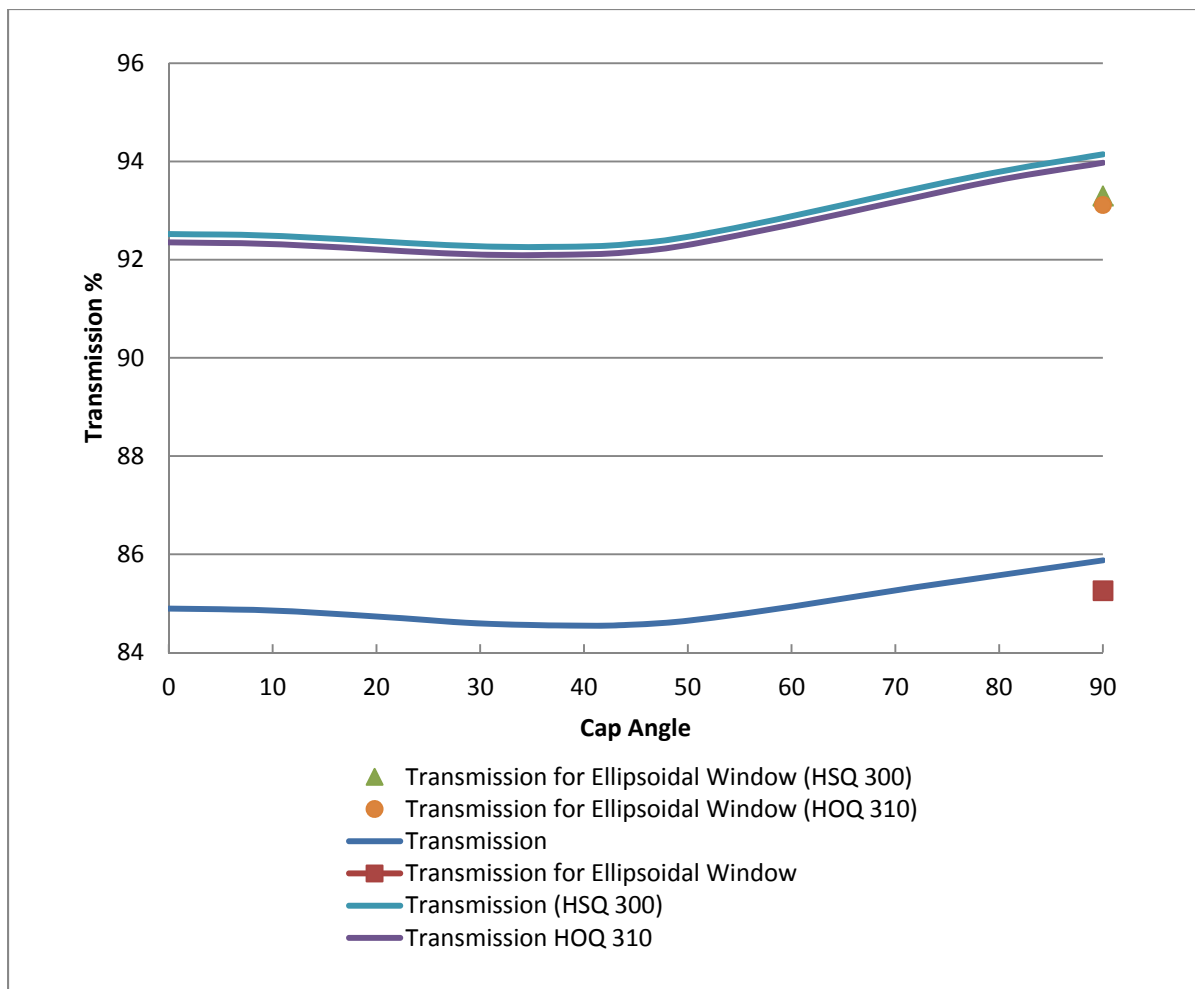


Figure 61. Transmission for different geometries and types of quartz.

ABSORPTION MAPS ON THE WINDOW

There are several reasons why the absorption (absorbed flux) maps on the window are needed. One of the reasons is to have a better understanding of how well the concentrated flux is focused on the window. Another reason is to figure out the location of the highest concentration and how it changes throughout the day. The highest concentration will occur where the absorption is highest at the window. The third reason is that the value of the highest flux can be determined, which can be a limiting factor for the window since the window has to operate under 1000 K. High absorption might bring the temperature up to 1000 K. The fourth reason is to get the thermal loading on the window for the use of calculating thermal gradient throughout the window, thus, calculating the stresses.

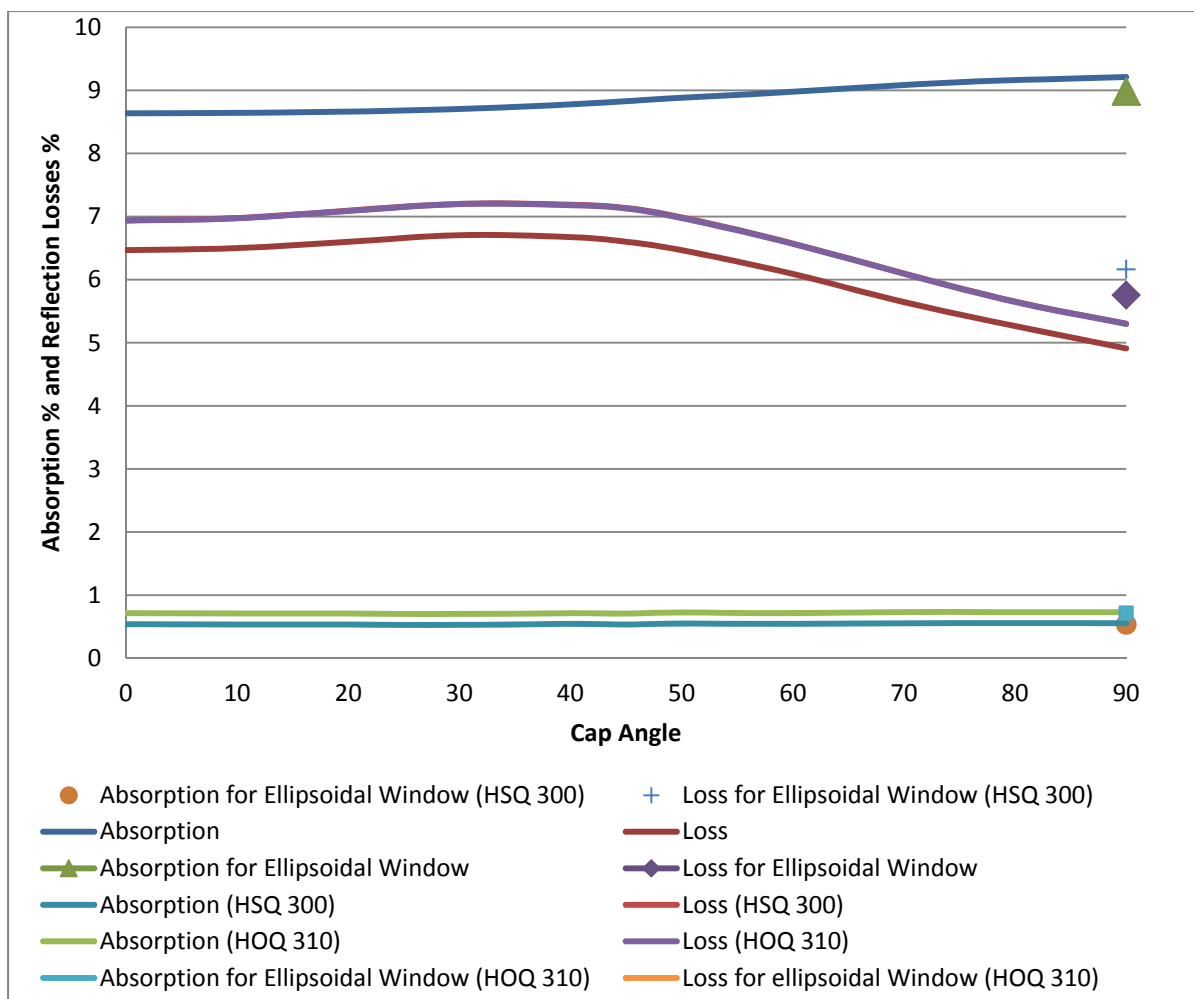


Figure 62. Absorption and reflection losses for different geometries.

The grid map shown in Figure 10 is used except this time the z axis is also needed since the window is not flat. There are 1600 grid cells. As mentioned in Chapter 2, 16 million rays would be enough to get good numerical results. This number will not be enough for the absorption maps. The reason is that the number of the rays per grid cell is very low and this will bring display issues. For example, the absorption for HOQ 310 is approximately 0.7% for 60 degree spherical cap. If there were 16 million rays used, 112000 rays would be absorbed. If every single grid cell had same amount of absorbed rays, then each grid cell would have 70 rays. But the concentration of the rays hitting the center is much higher than the rays the outer edges. In this case some cells will not have any rays and the flux will be zero unless we have enough rays. Several numbers of rays were studied but 900 million rays showed good results for the display. Therefore 900 million rays are used for each absorption map.

Three different window shapes (60 and 45 degree spherical windows and ellipsoidal window) were studied on March 21st at 12 pm. In order to show the difference throughout the day, the absorption map for 60 degree spherical cap was studied on March 21st at 4 pm. The tilt angle for both ellipsoidal window and the 45 degree spherical window is 26.5 and it is 25.5 for 60 degree spherical window.

An isometric view of the absorption map for a 60 degree spherical window is shown in Figure 63 and the top view is shown in Figure 64. It is seen that the solar concentration is a little bit over the center of the window because the heliostat field is looking up towards the receiver. This pattern will be seen for each absorption map. The highest heat flux is approximately 3.5×10^4 Watt/m².

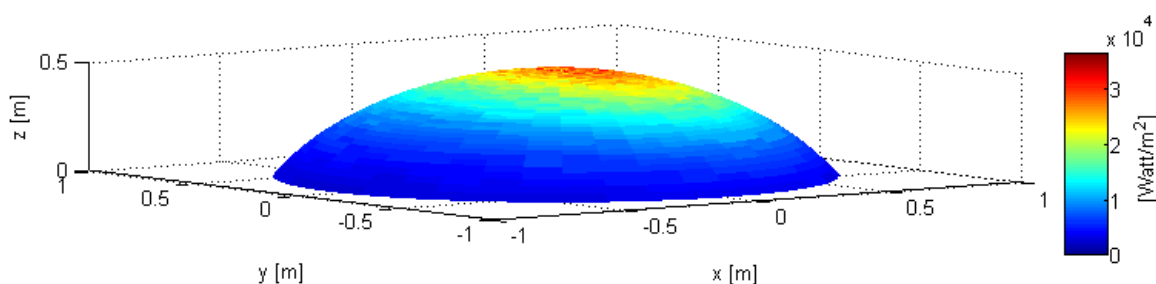


Figure 63. Absorption map for 60 degree spherical cap on 3/21 at 12 pm.

An isometric view of the absorption map for a 60 degree spherical window at 4 pm is shown in Figure 65 and the top view is shown in Figure 66. The solar concentration is a little bit over the center of the window but to the left because the location of the sun is different (south west). The highest heat flux is approximately 13000 which is much lower than 12 pm because the solar radiation is not as intense since the sun light will travel longer in the atmosphere.

An isometric view of the absorption map for a 45 degree spherical window is shown in Figure 67 and the top view is shown in Figure 68. The solar concentration here is also a little bit over the center of the window because the heliostat field is looking up towards the receiver. The highest heat flux is also approximately 3.5×10^4 Watt/m².

An isometric view of the absorption map for an ellipsoidal window is shown in Figure 69 and the top view is shown in Figure 70. The solar concentration pattern here is also similar to the other geometries (for 12 pm on March 21st). The highest heat flux is also approximately 3.5×10^4 Watt/m². All the windows show similar results because the change in geometry does not have a significant effect on the absorption since the thickness is the same. One difference in ellipsoidal

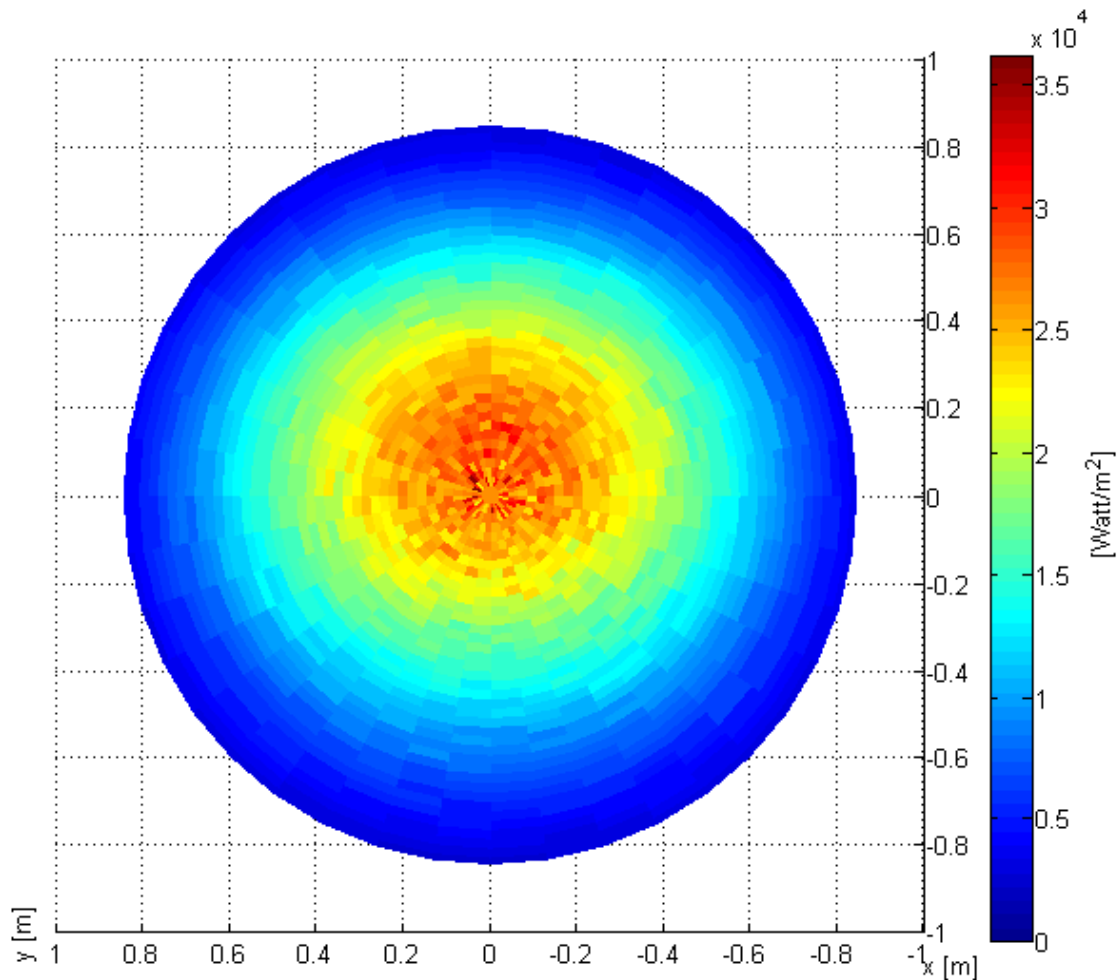


Figure 64. Absorption map for 60 degree spherical window on 3/21 at 12 pm top view (looking from inside the receiver).

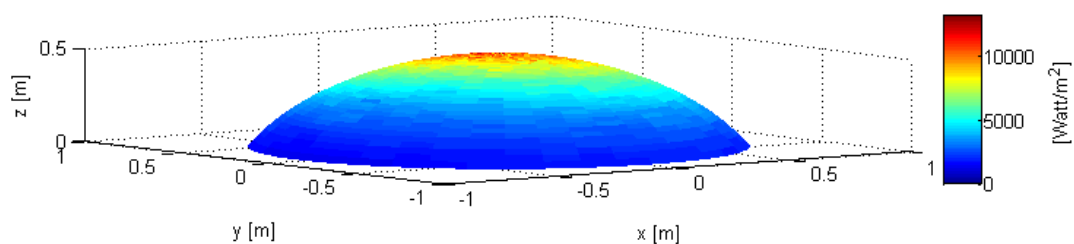


Figure 65. Absorption map for 60 degree spherical window on 3/21 at 4 pm.

window is that it has lower heat flux along the edges of the window. This is observed because the edges of ellipsoidal window are steeper. That means higher area along the edges and the solar radiation input is almost the same.

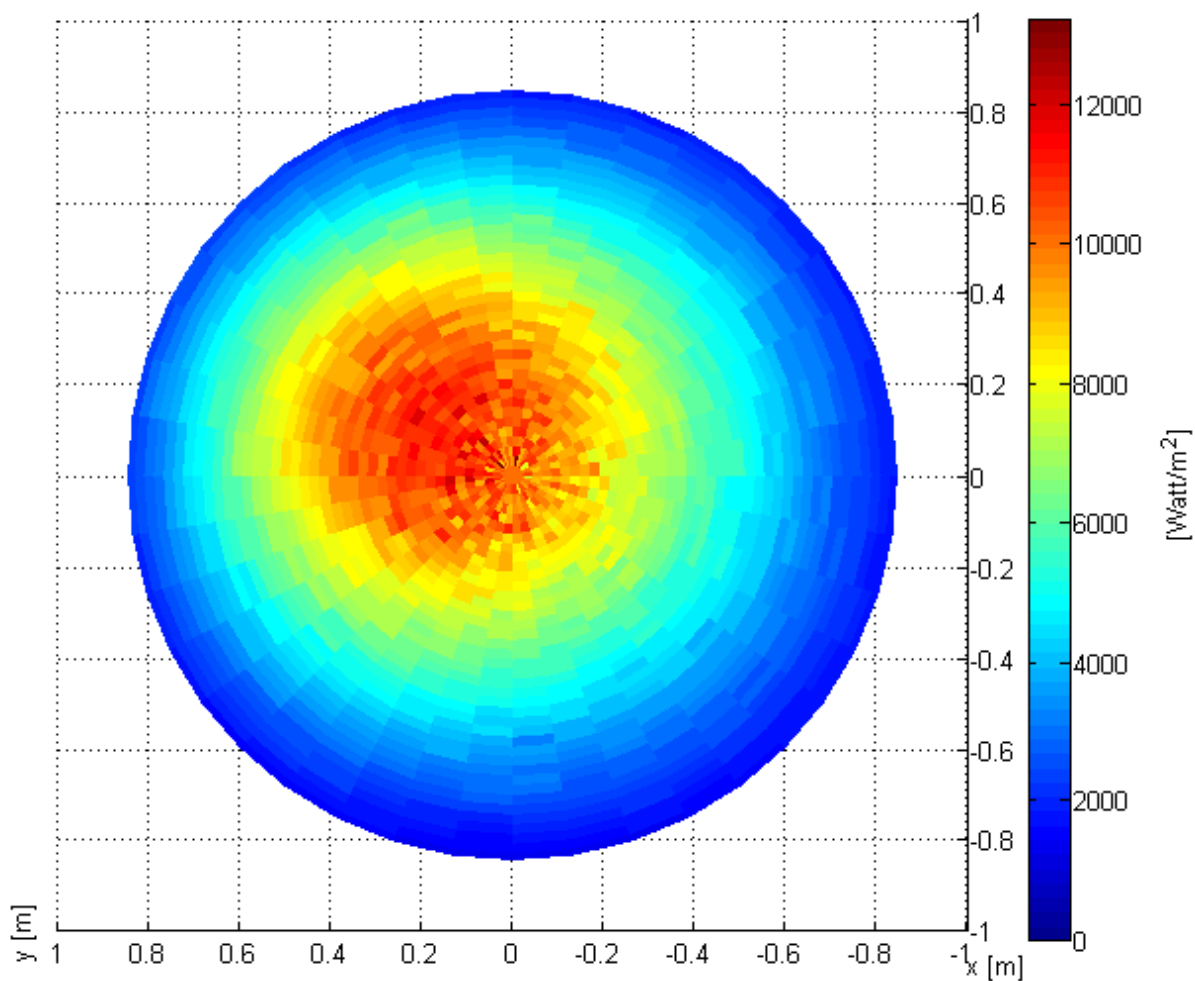


Figure 66. Absorption map for 60 degree spherical window on 3/21 at 4 pm top view (looking from inside the receiver).

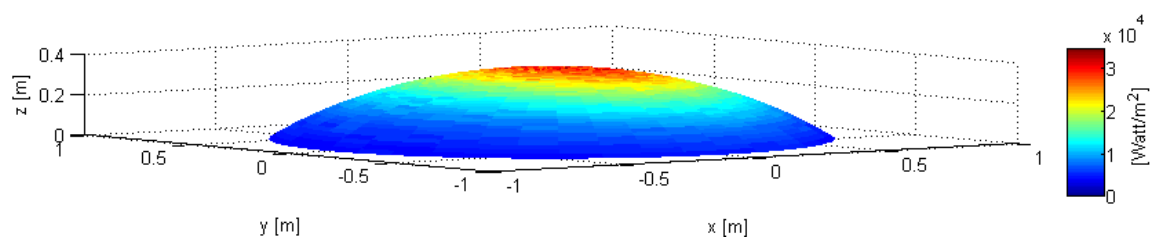


Figure 67. Absorption map for 45 degree spherical window on 3/21 at 12 pm.

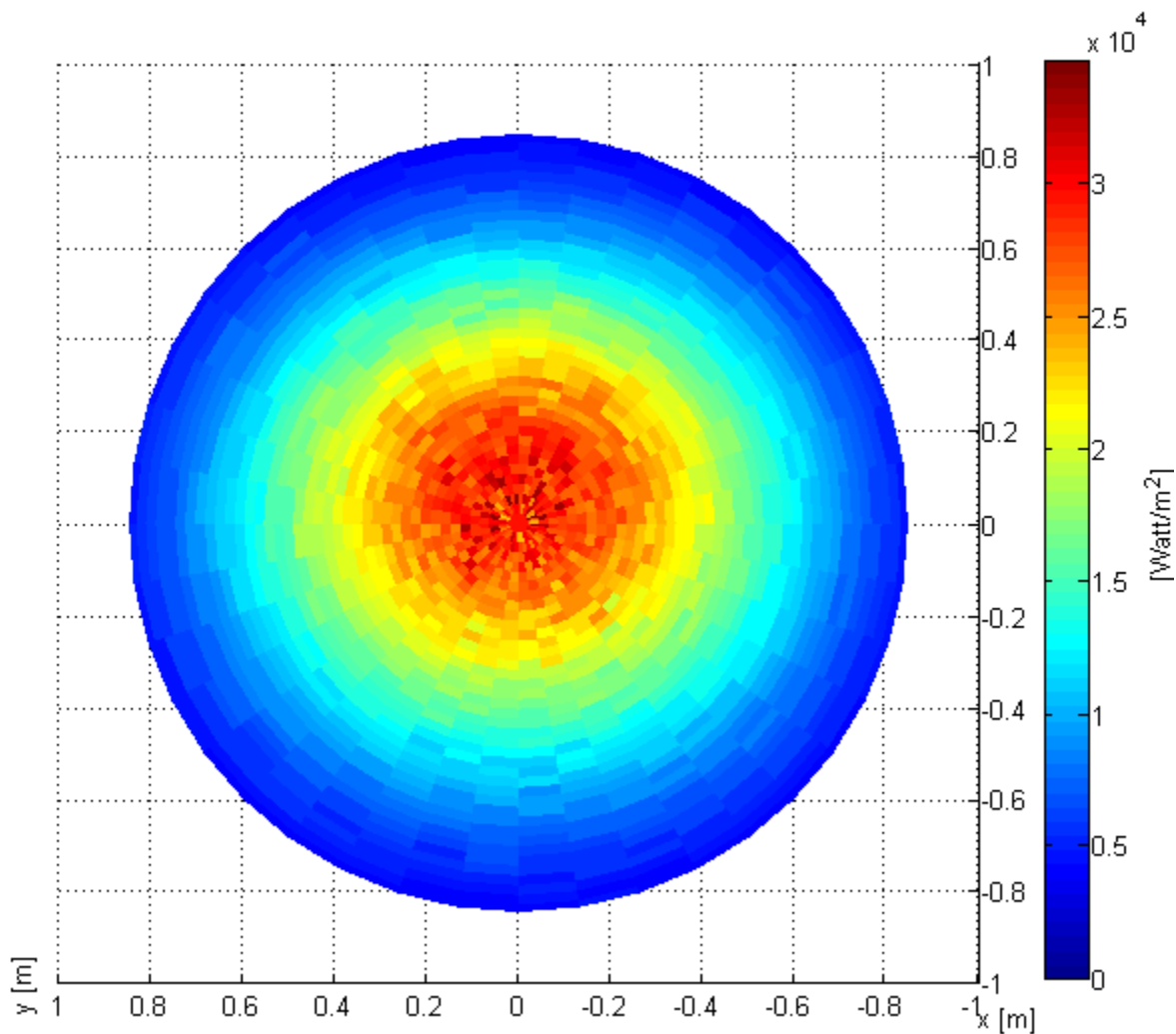


Figure 68. Absorption map for 45 degree spherical window on 3/21 at 12 pm top view (looking from inside the receiver).

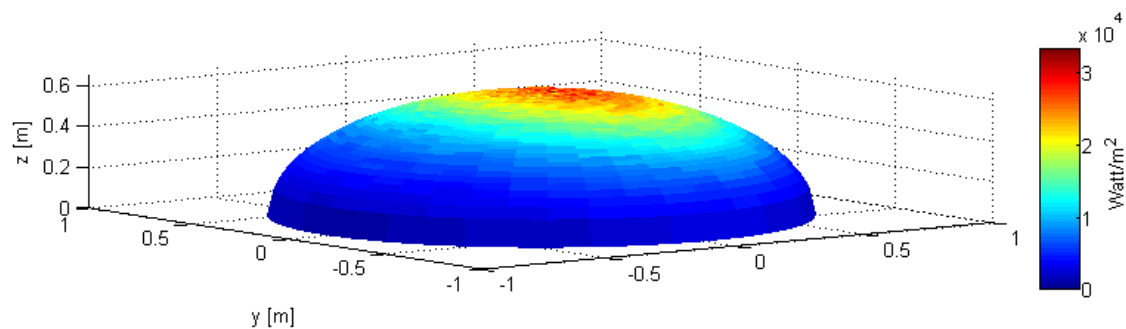


Figure 69. Absorption map for ellipsoidal window on 3/21 at 12 pm.

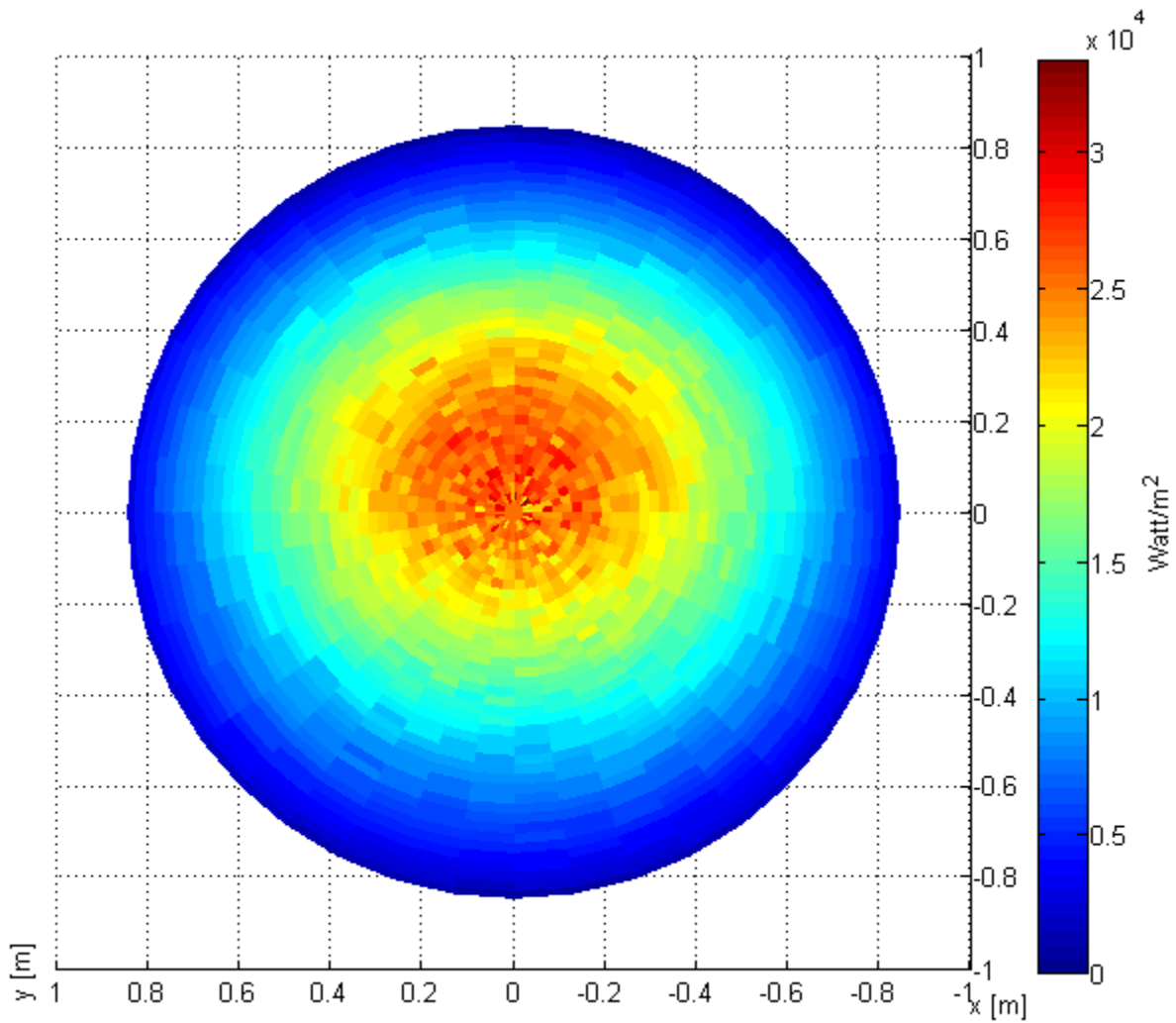


Figure 70. Absorption map for ellipsoidal window on 3/21 at 12 pm top view (looking from inside the receiver).

CHAPTER 8

CONCLUSIONS

The work presented in this thesis determines the thermal load on the window from the heliostat field depending on the time of day and day of the year. Different thicknesses and geometries of the window are studied as well as the tilt angle of the receiver from a fixed location at the power tower for different grades of fused quartz.

First, solar irradiation at the aperture plane on the power tower was studied and the results showed that the window needs to have a radius of at least 0.85 m or higher in order to get approximately 5 MW power on its surface for the base case of 12 noon on March 21st. After determining this number and contacting the vendor, 0.85 m was picked for window radius at the aperture plane. This value was suggested by the vendor because if the window is bigger than that the production is going to be much harder since more than one glass blank need to be used, therefore the cost of the window will be drastically higher. Again according to the vendor, a minimum 25 mm thickness for the window was suggested for handling purposes, although we studied thicknesses from 10 mm to 40 mm in some cases to determine the effect of thickness on the window optics.

Determining the radius of the window at the aperture plane and the thickness of the window allowed us next study the shape of the window. It was concluded in previous research that the window needs to be curved in order to withstand the pressure inside the receiver [28]. Therefore, an ellipsoidal window and spherical windows with different cap angles were studied in this research.

The main objective of this research was then to determine the overall transmission, absorption, and the reflective losses from these variously shaped windows. It is highly important to determine these quantities because each of them has a tremendous effect on the efficiency of the receiver. An eventual goal pursued by another student in the lab is to find the temperature of the window depending on the results from this research. The temperature of the window is a very important design factor. It has to be less than 1000 K to preserve the stability of the quartz. This makes the window a key component of the receiver. It should be pointed out that the window is

also the most expensive part of the receiver. Therefore considering the temperature effect and the cost, this research is very important to pick the right window material and geometry.

Knowing the importance of the transmission, absorption, and the reflective losses, first the optical properties of the window such as the transmissivity, reflectivity, and absorptivity were studied [34]. The results showed that the optical properties of the window are highly dependent on the absorptive index of the material. First, generic fused quartz was studied. It was concluded that generic quartz has a high absorptivity and low transmissivity and it is not preferable for our window. Then it is understood that higher quality quartz is needed. Some data on the absorptive index for different grades of quartz are provided for specific wavelengths by the vendor. The results showed much better transmissivity and much lower absorptivity.

In this research, the data for absorptive index is needed over a wide wavelength range (solar spectrum). The vendor unfortunately could not provide this information. But the transmission for a 10 mm thick window was given. Back tracking from this information the author obtained the approximate absorptive index data and continued with the calculations to find the optical properties. Two of the materials were mainly studied: HSQ 300 and HOQ 300. The accuracy of this method depends on both digitizing the transmissivity from the figures and how absorptive index was picked. The accuracy for digitizing is approximately 2% and the absorptive index is within 10-20% depending on how small the value of the absorptive index is.

The next step was to trace the rays from the aperture plane (where they are known from MIRVAL) to the curved window. The transmission, absorption, and reflective losses for different window geometries and materials were calculated by using the optical properties along with tracing rays. Results showed that a 90 degree cap angle had higher transmission compared to any other spherical window or the ellipsoidal window. The ellipsoidal window showed similar results to the 70 degree spherical window. The 45 degree spherical window showed the least amount of transmission. But the vendor suggested the lower the degree of the cap angle the easier and the cheaper to manufacture. Thus, there will be a trade-off between window efficiency and window manufacturability and cost.

The results of this research indicate that tilt angle and time of day did not have a significant effect on the transmission and absorption of the window. On the other hand, window thickness, geometry, and material type had a tremendous impact on the results. It is found that the absorption on the window is less than linear with thickness. Certain grades of quartz from

Hereaus were found to be much better than generic quartz, although a final conclusion on this is still open since we were unable to obtain a reliable data set of absorptive index across a wide wavelength range. Optically, the hemispherical window showed the best results for all window geometries. However, there are other factors, such as manufacturing constrains, mounting, cost, and heat losses from inside of the receiver, to consider when choosing the best window for the receiver. These factors are under research by other students in the SDSU Combustion and Solar Energy Laboratory and were evaluated along with the optical predictions from this thesis to choose the optimal window shape.

CHAPTER 9

FUTURE WORK

There are several recommendations for future work. The first one is to get the actual absorptive index data for different window materials over a wide wavelength range and compare the optical properties to see how accurate the current results are. The lack of this data is the single largest uncertainty in the design of the window at this point, and the thermal load from the heliostats depends strongly on the values of the absorptive index. The absorptive index may need to be measured within the interested wavelength range since the vendor does not supply enough information within this range.

Another recommended work is to do a year-long study to see how the power reaching the aperture plane and entering the window changes throughout the year by using MIRVAL. This study is actually started, but due to inconsistent results it is not displayed in this thesis. Therefore it needs to be investigated more to make sure the current results are valid. A better understanding of MIRVAL would also be useful; so that mirror surface accuracy can be varied (it is currently set as the default value).

Another recommended work is to couple the code developed in this research with the receiver model to calculate the thermal load on the window coming from inside the receiver. Along with the thermal load, the radiation losses from inside the receiver should be calculated for different window geometries. These radiation losses and thermal load on the window should be studied with the transmission, absorption and the reflective losses (only considering the radiation from the heliostat field) to optimize the shape of the window. It should be kept in mind that, the deeper window, for example a hemisphere, will have higher transmission from the heliostat field side but will have more losses from the inside of the receiver since the area of the window is bigger.

The programs developed in this research also allow us to consider a secondary concentrator to increase the incident radiation to the system without increasing the window diameter. Since the small particle receiver does not have any practical flux limitation (unlike tubular receivers), providing more power through the same window will result in a higher

efficiency receiver. The development of a secondary concentrator will depend on the heliostat field, and must be coupled with the overall receiver design.

The final recommendation is to study the effect of the thermal load from a structural stand point. Absorbed heat flux on the window is calculated locally in this thesis. This calculation will feed into calculating the window internal temperature distribution, and from that the thermal stresses developed on the window can be studied.

REFERENCES

- [1] Pashmina. "BP Statistical Review of World Energy." Last modified June 2009. http://www.et2050.eu/pashmina/index.php?option=com_content&view=category&layout=blog&id=38&Itemid=75.
- [2] McLamb, Eric. "Fossil Fuels vs. Renewable Energy Resources." Ecology Global Network. Last modified September 6, 2011. <http://www.ecology.com/2011/09/06/fossil-fuels-vs-renewable-energy-resources/>.
- [3] Lifsher, Marc. "California Alternative Energy Legislation Gets Broad Backing." *Los Angeles Times*, June 24, 2010. <http://articles.latimes.com/2010/jun/24/business/la-fi-renewable-power-20100624/2>.
- [4] Reuters. "Germany Targets Switch to 100% Renewable for its Electricity by 2050." *The Guardian*, July 7, 2010. <http://www.guardian.co.uk/environment/2010/jul/07/germany-renewable-energy-electricity>.
- [5] Gereffi, Gary, and Kristen Dubay. "Concentrating Solar Power: Clean Energy for the Electric Grid." Center on Globalization Governance & Competitiveness, 2008. Accessed April 26, 2013. http://www.cggc.duke.edu/environment/climatesolutions/greeneconomy_Ch4_ConcentratingSolarPower.pdf
- [6] International Energy Agency. "Technology Roadmap: Concentrating Solar Power." OECD/IEA, 2010. Accessed April 26, 2013. http://www.iea.org/publications/freepublications/publication/csp_roadmap.pdf
- [7] U. S. Department of Energy. "About the Solar Office." SunShot Initiative. Last modified February 7, 2013. <http://www1.eere.energy.gov/solar/sunshot/about.html>.
- [8] U. S. Department of Energy. "Overview of the SunShot Initiative." Accessed May 3, 2013. <http://www.uwig.org/Golden2012/SunShot-Banunarayanan.pdf>.
- [9] Volker Quaschnig. "Technology Fundamentals: Solar Thermal Power Plants." Last modified June 2003. <http://www.volker-quaschnig.de/articles/fundamentals2/index.php>.
- [10] International Renewable Energy Agency. "Concentrating Solar Power." IRENA Working Paper, International Renewable Energy Agency, Abu Dhabi, UAE, 2012. http://www.irena.org/DocumentDownloads/Publications/RE_Technologies_Cost_Analysis-CSP.pdf
- [11] European Commission. "Concentrating Solar Power: From Research to Implementation." Luxembourg: Office for Official Publications of the European Communities, 2007. Accessed April 26, 2013. http://ec.europa.eu/energy/publications/doc/2007_concentrating_solar_power.pdf
- [12] Schell, Steve. "Design and Evaluation of Esolar's Heliostat Fields." *Solar Energy* 85, no. 4 (2011): 614-619.

- [13] Hunt, Arlon J. "A New Solar Thermal Receiver Utilizing Small Particles." In *Sun II: Proceedings of the International Solar Energy Society, Silver Jubilee Congress, Atlanta, GA*, 1362-1366. Elmsford, NY: Pergamon Press, 1979.
- [14] Hunt, Arlon J., and C. T. Brown. *Solar Testing of the Small Particle Heat Exchanger (SPHER)* (LBL-15807). Berkeley, CA: Lawrence Berkeley National Laboratory, 1983.
- [15] Bertocchi, Rudi, Jacob Karni, and Abraham Kribus. "Experimental Evaluation of a Non-Isothermal High Temperature Solar Particle Receiver." *Energy* 29, no. 5-6 (2004): 687-700.
- [16] Buck, Reiner, Eckhard Lüpfer, and Félix Tellez. "Receiver for Solar-Hybrid Gas Turbine and CC Systems (REFOS)." Paper presented at the 10th SolarPACES International Symposium on Solar Thermal Concentrating Technologies, Sydney, Australia, 2000.
- [17] Heller, Peter, Markus Pfänder, Thorsten Denk, Felix Tellez, Antonio Valverde, Jesús Fernandez, and Arik Ring. "Test and Evaluation of a Solar Powered Gas Turbine System." *Solar Energy* 80, no. 10 (2006): 1225-1230.
- [18] Klein, Hanna Helena, Rachamim Rubin, and Jacob Karni. "Experimental Evaluation of Particle Consumption in a Particle Seeded Solar Receiver." *Journal of Solar Energy Engineering* 130, no. 1 (2007): 011012-8.
- [19] Miller, Fletcher J., and Arlon J. Hunt. "Developing the Small Particle Heat Exchange Receiver for a Prototype Test." Paper presented at the ASME 2012 6th International Conference on Energy Sustainability, San Diego, CA, July 2012.
- [20] Miller, Fletcher J. "An Experimental and Theoretical Study of Heat Transfer in a Gas-Particle Flow Under Direct Radiant Heating." PhD diss., University of California at Berkeley, 1988.
- [21] Ruther, Steven James. "Radiation Heat Transfer Simulation of a Small Particle Solar Receiver Using the Monte Carlo Method." Master's Thesis, San Diego State University, 2010.
- [22] Crocker, Adam. "Coupled Fluid Flow and Radiation Modeling of a Small Particle Solar Receiver." Master's Thesis, San Diego State University, 2012.
- [23] Fernandez del Campo, Pablo, and Fletcher J. Miller. "Three-Dimensional Fluid Dynamics and Radiative Heat Transfer Modeling of a Small Particle Solar Receiver." Paper presented at ASME 2013 Summer Heat Transfer Conference, Minneapolis, MN (forthcoming).
- [24] Howell, J. R., and M. Perlmutter. "Monte Carlo Solution of Thermal Transfer Through Radiant Media Between Gray Walls." *Journal of Heat Transfer* 86, no. 1 (1964): 116-122.
- [25] Howell, J. R. "The Monte Carlo Method in Radiative Heat Transfer." *Journal of Heat Transfer* 120 (1997): 547-560.
- [26] Garcia, P., Alain Ferriere, and Jean-Jacques Bezier. "Codes for Solar Flux Calculation Dedicated to Central Receiver System Applications: A Comparative Review." *Solar Energy* 82, no. 3 (2008): 189-197.

- [27] Tonatiuh. "Tonatiuh - A Monte Carlo Ray Tracer for the Optical Simulation of Solar Concentrating Systems." Google Code Project. Accessed April 26, 2013. <http://code.google.com/p/tonatiuh/>.
- [28] Mande, Onkar Kiran. "Window and Seal Design for a Small Particle Solar Receiver." Master's Thesis, San Diego State University, 2011.
- [29] Saung, E-Fann, and Miller, Fletcher. "Dome Window and Mount Design for a Large Scale Solar Receiver." Paper presented at ASME 2013 Summer Heat Transfer Conference, Minneapolis, MN (forthcoming).
- [30] Leary, P. L., and J. D. Hankins. *User's Guide for MIRVAL: A Computer Code for Comparing Designs of Heliostat-Receiver Optics for Central Receiver Solar Power Plants (SAND-77-8280)*. Livermore, CA: Sandia National Laboratory, 1979.
- [31] Ho, Cliff. E-mail Message to Author, October 2012.
- [32] American Society for Testing and Materials. "Reference Solar Spectral Irradiance: Air Mass 1.5." Accessed April 26, 2013. <http://rredc.nrel.gov/solar/spectra/am1.5/>.
- [33] Knuth, Donald E. *The Art of Computer Programming*. Vol. 1, *Sorting and Searching*. Reading, MA: Addison-Wesley Professional, 1986.
- [34] Kitamura, Rei, Laurent Pilon, and Miroslaw Jonasz. "Optical Constant of Silica Glass from Extreme Ultraviolet to Far Infrared at Near Room Temperature." *Applied Optics* 46, no. 33 (2007): 8118-8133.
- [35] Howell, John R., Robert Siegel, and M. Pinar Mengüç. *Thermal Radiation Heat Transfer*. 5th ed. New York, NY: Taylor & Francis, 2011.
- [36] Duffie, John A., and William A. Beckman. *Solar Engineering of Thermal Processes*. 3rd ed. Hoboken, New Jersey: John Wiley & Sons, 2006.
- [37] Heraeus Quarzglas. "Heraeus Quarzglas - Home of Quartz Solutions." Heraeus Quarzglas Homepage. Accessed April 26, 2013. <http://heraeus-quarzglas.com/en/home/Home.aspx>.
- [38] Khashan, M. A., and A. Y. Nassif. "A Simple Method of Determining the Dispersion of a Solid Material from the Reflectance Interferogram of Sheer Material." *Optic Communications* 198, no. 4-6 (2001): 247-256.
- [39] Beder, E. C., C. D. Bass, and W. L. Shackelford. "Transmissivity and Absorption of Fused Quartz Between 0.22 μ and 3.5 μ from Room Temperature to 1500 $^{\circ}$ C." *Applied Optics* 10, no. 10 (1971): 2263-2268.
- [40] Calingaert, G., S. Heron, and R. Stair. *Sapphire and Other New Combustion-Chamber Window Materials*. SAE Technical Paper 360144, 1936. doi:10.4271/360144.
- [41] Mande, Onkar K., and Fletcher Miller. "Window Design for a Small Particle Solar Receiver." Paper presented at the 9th Annual International Energy Conversion Engineering Conference, San Diego, CA, July 2011.
- [42] Brewster, M. Quinn. *Thermal Radiative Heat Transfer & Properties*. Hoboken, New Jersey: John Wiley & Sons, 1992.

APPENDIX

**FIT EQUATIONS FOR ABSORPTIVE INDEX FOR
GENERIC FUSED QUARTZ**

In the equations given below for specific wavelength interval, y represents the log of absorptive and l represents the wavelength.

Wavelength interval: 0.09 to 0.12

$$y = 1.6336182985 \cdot 10^{+10} \cdot l^6 - 1.97030278775701 \cdot 10^{+10} \cdot l^5 + 7.86839165511285 \cdot 10^{+09} \cdot l^4 - 1.51165428367874 \cdot 10^{+09} \cdot l^3 + 1.53973317472502 \cdot 10^{+08} \cdot l^2 - 8.04740570336953 \cdot 10^{+06} \cdot l + 1.70516642439461 \cdot 10^{+05}$$

Wavelength interval: 0.12 to 0.26

$$y = 3.25725406195068 \cdot 10^{+06} \cdot l^6 - 3.52720444544116 \cdot 10^{+05} \cdot l^5 - 1.54736169810495 \cdot 10^{+06} \cdot l^4 + 8.33348547493981 \cdot 10^{+05} \cdot l^3 - 1.78271302915381 \cdot 10^{+05} \cdot l^2 + 1.73865911860176 \cdot 10^{+04} \cdot l - 6.39760878331422 \cdot 10^{+02}$$

Wavelength interval: 0.26 to 0.4

$$y = -3.59565907367187 \cdot 10^{+08} \cdot l^6 + 7.33146344189131 \cdot 10^{+08} \cdot l^5 - 6.20956854511939 \cdot 10^{+08} \cdot l^4 + 2.79631622336298 \cdot 10^{+08} \cdot l^3 - 7.06114150473072 \cdot 10^{+07} \cdot l^2 + 9.47957750891990 \cdot 10^{+06} \cdot l - 5.28576706718734 \cdot 10^{+05}$$

Wavelength interval: 0.4 to 1

$$y = -1.06443946194648 \cdot 10^{+03} \cdot l^6 + 4.65545955720186 \cdot 10^{+03} \cdot l^5 - 8.32905634386611 \cdot 10^{+03} \cdot l^4 + 7.78781213477723 \cdot 10^{+03} \cdot l^3 - 4.00797330395235 \cdot 10^{+03} \cdot l^2 + 1.07610690701185 \cdot 10^{+03} \cdot l - 1.24944378863452 \cdot 10^{+02}$$

Wavelength interval: 1 to 2

$$y = 2.80338983647525 \cdot 10^{+01} \cdot l^6 - 2.83038914340883 \cdot 10^{+02} \cdot l^5 + 1.17250078402603 \cdot 10^{+03} \cdot l^4 - 2.55132773495765 \cdot 10^{+03} \cdot l^3 + 3.07720169774303 \cdot 10^{+03} \cdot l^2 - 1.95117327594816 \cdot 10^{+03} \cdot l + 5.00884484344046 \cdot 10^{+02}$$

Wavelength interval: 2 to 5

$$y = 6.02689243547502 \cdot 10^{-01} \cdot l^6 - 1.26613745333414 \cdot 10^{+01} \cdot l^5 + 1.08943808193088 \cdot 10^{+02} \cdot l^4 - 4.90843367427885 \cdot 10^{+02} \cdot l^3 + 1.21997407389880 \cdot 10^{+03} \cdot l^2 - 1.583542242045 \cdot 10^{+03} \cdot l + 8.31459432767667 \cdot 10^{+02}$$

Wavelength interval: 5 to 7.46

$$y = -2.68982855668582 \cdot 10^{-01} \cdot l^6 + 9.97560456109881 \cdot l^5 - 1.53573993099075 \cdot 10^{+02} \cdot l^4 + 1.25631759038428 \cdot 10^{+03} \cdot l^3 - 5.76016977204904 \cdot 10^{+03} \cdot l^2 + 1.40355327328843 \cdot 10^{+04} \cdot l - 1.42026261138911 \cdot 10^{+04}$$

Wavelength interval: 7.46 to 8

$$y = 1.28625872658193 \cdot 10^{+03} \cdot l^6 - 6.02081317900420 \cdot 10^{+04} \cdot l^5 + 1.17415820012597 \cdot 10^{+06} \cdot l^4 - 1.22110396657999 \cdot 10^{+07} \cdot l^3 + 7.14261060161121 \cdot 10^{+07} \cdot l^2 - 2.22800288123221 \cdot 10^{+08} \cdot l + 2.89546895513200 \cdot 10^{+08}$$

Wavelength interval: 8 to 9.1

$$y = -4.12752329849172 \cdot l^6 + 2.10262508391355 \cdot 10^{+02} \cdot l^5 - 4.46345912096258 \cdot 10^{+03} \cdot l^4 + 5.05406607184139 \cdot 10^{+04} \cdot l^3 - 3.21962752936773 \cdot 10^{+05} \cdot l^2 + 1.09409163658216 \cdot 10^{+06} \cdot l - 1.54948350408040 \cdot 10^{+06}$$

Wavelength interval: 9.1 to 10.1

$$y = 2.56939469825011 \cdot l^6 - 1.40976312122631 \cdot 10^{+02} \cdot l^5 + 3.21898916540474 \cdot 10^{+03} \cdot l^4 - 3.91504993702661 \cdot 10^{+04} \cdot l^3 + 2.67482701138831 \cdot 10^{+05} \cdot l^2 - 9.73282701467233 \cdot 10^{+05} \cdot l + 1.47340063457588 \cdot 10^{+06}$$

Wavelength interval: 10.1 to 11.22

$$y = -2.83195101125165 \cdot 10^{+01} \cdot l^6 + 1.82141500457004 \cdot 10^{+03} \cdot l^5 - 4.87984892941604 \cdot 10^{+04} \cdot l^4 + 6.97089709839335 \cdot 10^{+05} \cdot l^3 - 5.59989822729340 \cdot 10^{+06} \cdot l^2 + 2.39859805990267 \cdot 10^{+07} \cdot l - 4.27967923688059 \cdot 10^{+07}$$

Wavelength interval: 11.22 to 12.4

$$y = -1.11990933793131 \cdot 10^{+01} \cdot l^6 + 8.02765664457621 \cdot 10^{+02} \cdot l^5 - 2.39683204666042 \cdot 10^{+04} \cdot l^4 + 3.81538691932741 \cdot 10^{+05} \cdot l^3 - 3.41519039097181 \cdot 10^{+06} \cdot l^2 + 1.62982987370468 \cdot 10^{+07} \cdot l - 3.23974077131514 \cdot 10^{+07}$$

Wavelength interval: 12.4 to 14.3

$$y = 1.89520519159123 * 1^6 - 1.50984432877632 * 10^{+02} * 1^5 + 5.00933634498779 * 10^{+03} * 1^4 - 8.85951460044576 * 10^{+04} * 1^3 + 8.80937083426030 * 10^{+05} * 1^2 - 4.66940031991698 * 10^{+06} * 1 + 1.03073863940172 * 10^{+07}$$

Wavelength interval: 14.3 to 20.7

$$y = -3.12034933992678 * 10^{-04} * 1^6 + 3.21710679942278 * 10^{-02} * 1^5 - 1.37498245617038 * 1^4 + 3.11863832902918 * 10^{+01} * 1^3 - 3.95966193091158 * 10^{+02} * 1^2 + 2.66907069262195 * 10^{+03} * 1 - 7.46608842940852 * 10^{+03}$$

Wavelength interval: 20.7 to 24.7

$$y = -5.45170469838752 * 10^{-03} * 1^6 + 7.50442548679246 * 10^{-01} * 1^5 - 4.30244841044873 * 10^{+01} * 1^4 + 1.31502359505029 * 10^{+03} * 1^3 - 2.25991415208058 * 10^{+04} * 1^2 + 2.07044740522034 * 10^{+05} * 1 - 7.90018256635863 * 10^{+05}$$

Wavelength interval: 24.7 to 50

$$y = 1.33755493657468 * 10^{-07} * 1^6 - 3.07779399795551 * 10^{-05} * 1^5 + 2.92272147078789 * 10^{-03} * 1^4 - 1.46578039751812 * 10^{-01} * 1^3 + 4.09402796734044 * 1^2 - 6.04171364002270 * 10^{+01} * 1 + 3.67638759474446 * 10^{+02}$$